JETP Letters, Vol. 78, No. 1, 2003, pp. 1–4. Translated from Pis'ma v Zhurnal Éksperimental'noĭ i Teoreticheskoĭ Fiziki, Vol. 78, No. 1, 2003, pp. 3–7.

Analysis of the $Hb\bar{b}$ Coupling Constant and *CP*-Violation Effects at the Future e^+e^- Collider

V. Braguta[1], A. Chalov[1], A. Likhoded[1, 2, *], and R. Rosenfeld[2,]**

[1] *Institute for High Energy Physics, Protvino, Moscow region, 142284 Russia*
[2] *Instituto de Física Teórica, UNESP, 01405-900, São Paulo, Brasil*
* *e-mail: andre@ift.unesp.br*
** *e-mail: rosenfel@ift.unesp.br*
Received May 20, 2003

The $e^+e^- \longrightarrow b\bar{b}\nu\bar{\nu}$ process, where ν is an electron, muon, or τ-lepton neutrino, is analyzed in detail for the general form of the coupling constant of a Higgs boson with b quarks, with the $(m_b/v)(a + i\gamma_5 b)$ parameterization of the $Hb\bar{b}$ interaction. This process is shown to be highly sensitive to this coupling constant. Experiments at the future with $\sqrt{s}$ = 500-GeV linear collider will provide limits of 2 and 20% for deviations of the parameters a and b, respectively, from their Standard Model values. Results concerning the $e^+e^- \longrightarrow b\bar{b}\nu\bar{\nu}$ process in combination with the independent measurements of the partial width $\Gamma_{H \to b\bar{b}}$ can testify to the *CP* origin of the Higgs sector of the theory. © *2003 MAIK "Nauka/Interperiodica".*
PACS numbers: 13.66.Fg; 11.30.Er; 14.80.Cp

1. INTRODUCTION

The origin of fermion mass is one of the important problems of particle physics. The Higgs boson completely determines the electroweak-symmetry violation and generation of masses. However, it is obvious that the Standard Model in this aspect is not the final theory. Therefore, a careful search for nonstandard coupling constants of the Higgs boson [or, in fact, the admixture of the lightest pseudo(scalar) Higgs boson] with fermions can provide important information about the real mechanism of the origin of masses.

We previously discussed the possibility of detecting deviations of the coupling constants of the Higgs boson with τ leptons from their Standard Model values in experiments at the future linear collider [1]. In this work, we extend that analysis to the case of the coupling of the Higgs boson with b quarks, which seems to be preferable due to the larger Yukawa coupling. For definiteness, we focus on the determination of the (pseudo)scalar–b–$\bar{b}$ coupling constant at the future 500-GeV linear collider with a total emittance of 1 ab^{-1} according to the TESLA project [2]. We assume that the Higgs boson will be discovered earlier at LHC. However, its properties will be studied in detail at the linear collider.

All possible contributions to the $e^+e^- \longrightarrow b\bar{b}\nu\bar{\nu}$ process, where ν is an electron, muon, or τ-lepton neutrino, are taken into account. In particular, we emphasize that processes accompanied by the fusion of gauge bosons make the dominant contribution among the processes with the formation of the Higgs boson of $M_H <$ 180 GeV and $\sqrt{s} \geq 500$ GeV.

In various Standard Model extensions with additional scalar and pseudoscalar bosons, the lightest particle with zero spin can be a mixture of states with indefinite parity. Therefore, the $Hb\bar{b}$ coupling can generally be parameterized as

$$(m_b/v)(a + i\gamma_5 b), \tag{1}$$

where v = 246 GeV, m_b is the mass of the b quark, and $a = 1$ and $b = 0$ in the Standard Model. We discuss three cases: (i) a and b are independent parameters, (ii) $a = 1$ and b is a free parameter, and (iii) $b = 0$ and a is a free parameter. As will be shown, in the case of two independent parameters, there are insensitivity regions along circles in the a–b plane. This circumstance is determined by the impossibility of distinguishing between the a and b effects.

The cross section for the $e^+e^- \longrightarrow b\bar{b}\nu\bar{\nu}$ process involves terms linear in the parameter a, which are determined by the interference contributions of diagrams with and without the Higgs boson, and terms proportional to a^2 and b^2, which are determined by the contribution of Higgs boson. This behavior of observables makes it possible to search for deviations of the coupling constants from the Standard Model. In partic-

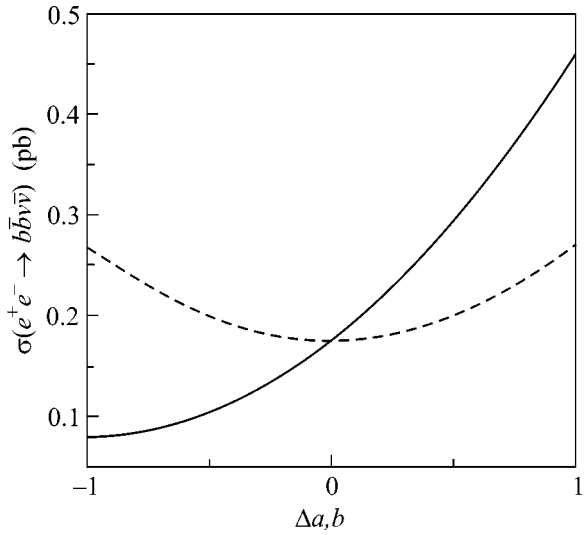

Fig. 1. Total cross section for the $e^+e^- \longrightarrow b\bar{b}\nu\bar{\nu}$ process vs. the parameters (solid line) Δa and (dashed line) b.

ular, such deviations are predicted in supersymmetric models.

The Standard Model predicts a value of about 180 fb for the total cross section for the $e^+e^- \longrightarrow b\bar{b}\nu\bar{\nu}$ process at $M_H = 120$ GeV and $\sqrt{s} = 500$ GeV. The process involving ν_e in the final state makes the major contribution to the cross section, in particular because only this channel includes diagrams with fusion of gauge bosons that make the basic contribution to the cross section. For comparison, the cross section for the $e^+e^- \longrightarrow H\nu_e\bar{\nu}_e$ process at $\sqrt{s} = 500$ GeV is about 100 fb.

Figure 1 shows the total reaction cross section summarized over all three neutrino types as a function of the parameters $\Delta a \equiv a - 1$ and b. The b dependence is symmetric about the $b = 0$ straight line, because only terms proportional to b^2 contribute to the cross section. At the same time, the Δa dependence is substantially asymmetric due to the contributions of the interference between diagrams with the Higgs boson and background Standard Model diagrams, which determine the presence of terms linear in Δa. We emphasize that the Δa dependence for $b\bar{b}$ is than for $\tau^+\tau^-$ [1] more pronounced. In this work, we estimate the sensitivity of experiments at the e^+e^- linear collider of the next generation to these parameters.

2. ANALYSIS AND RESULTS

Monte Carlo simulation of the data was carried out by generating the observables in the form of the following expansion in the coupling constants a and b multiplied by the kinematic factors:

$$\frac{d\sigma}{d\mathbb{O}} = A_0 + aA_1 + a^2A_2 + abA_3 + bA_4 + b^2A_5\ldots, \quad (2)$$

where $\mathbb{O}$ is an observable and A_i are the kinematic factors, which are independent of a and b and result from the calculation of diagrams and integration over the phase space. The Monte Carlo method is used to simulate the factors A_i. Therefore, the coupling constants a and b can be varied without the repetitive simulation of the data for each (a, b) pair. In the case under consideration, $A_3 = A_4 = 0$.

The generated event sample corresponds to statistics expected at the TESLA collider. The detector response is simulated by the SIMET 3.01 package [4]. We take the efficiency of the b-jet pair as $\varepsilon_{bb} = 56\%$ according to the b-taq algorithm [3]. The data are simulated with $M_H = 120$ GeV.

Figure 2 shows the differential distribution in $\cos\theta_{eb}$, where θ_{eb} is the scattering angle of the b jet with respect to the initial electron beam for the total contribution of the Standard Model diagrams and for the contributions of the diagrams involving the Higgs boson exchange (including diagrams of interference with the Standard Model). To illustrate the importance of the contribution of the process involving ν_e, we present both the contribution of the process involving ν_μ in the final state (which is virtually similar to the process involving ν_τ) and the total contribution from processes involving all three neutrino types. It is easy to see that the contribution from diagrams involving the Higgs boson is small, while it is comparable with the total Standard Model contribution in the total distribution.

To illustrate the effect of the variation in the parameters a and b, Fig. 3 shows the contribution of diagrams involving the Higgs boson to the distribution in $\cos\theta_{eb}$ for the process involving ν_μ and for the sum of all three processes for the Standard Model ($a = 1$, $b = 0$) and for $a = b = 0.5$. It is seen that the distribution shapes are very similar, as is expected, while normalizations differ considerably.

The contributions from possible background processes such as $e^+e^- \longrightarrow e^+e^-ZZ \longrightarrow e^+e^-b\bar{b}\nu\bar{\nu}$ (with a missing e pair), $e^+e^- \longrightarrow \nu\bar{\nu}\,W^+W^- \longrightarrow \nu\bar{\nu}b\bar{b}\nu\bar{\nu}$, and $e^+e^- \longrightarrow ZZZ \longrightarrow b\bar{b}\nu\bar{\nu}\nu\bar{\nu}$ either are small or can be significantly suppressed to 0.2 fb [3].

The characteristics of a future detector and possible sources of systematic errors are important. The systematic errors are expected to be equal to 0.5% in measurements of emittance, 1% in the determination of acceptance, 1% in the measurements of branching ratios, and 1% in the separation of the contributions from the background processes. We also assume a Gaussian distributions of systematic errors. We apply the standard χ^2 criterion to analyze events and to determine bounds on the

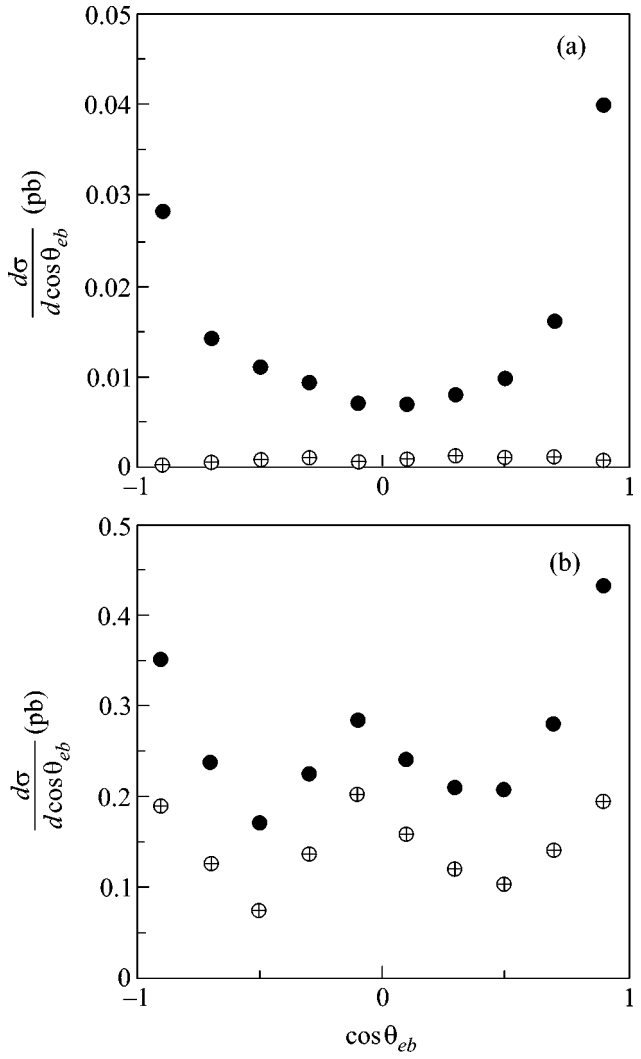

Fig. 2. Differential distribution in $\cos\theta_{eb}$ for the processes (a) $e^+e^- \longrightarrow b\bar{b}\nu_\mu\bar{\nu}_\mu$ and (b) $e^+e^- \longrightarrow b\bar{b}\nu\bar{\nu}$ summed over all neutrino types. The solid and crossed points correspond to the total Standard Model contribution and contribution from diagrams involving the Higgs boson (including interference terms).

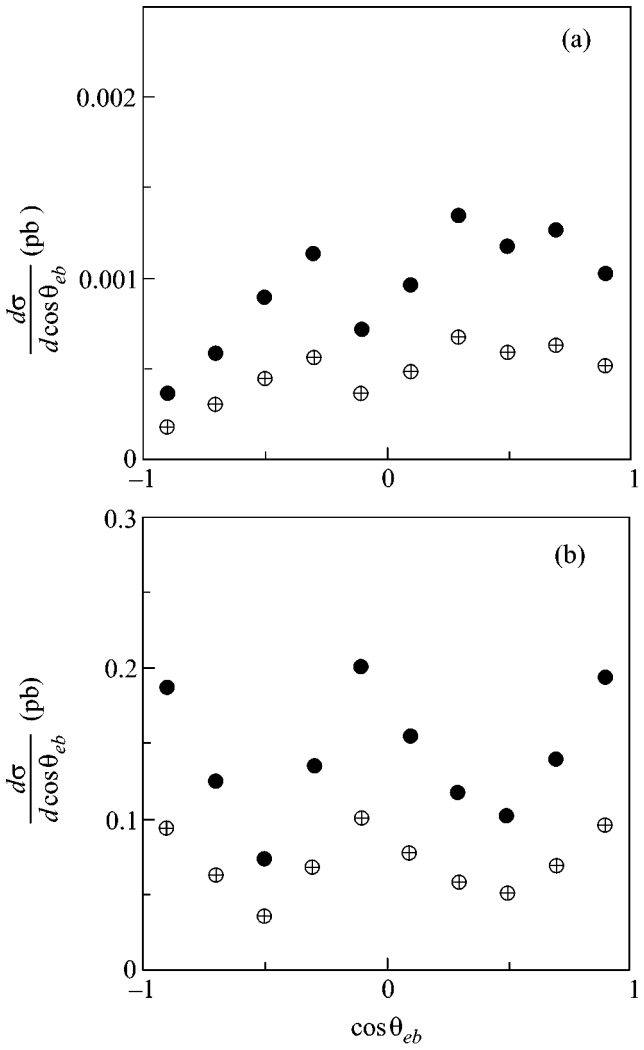

Fig. 3. Contribution from Higgs boson diagrams to the differential distribution in $\cos\theta_{eb}$ for the processes (a) $e^+e^- \longrightarrow b\bar{b}\nu_\mu\bar{\nu}_\mu$ and (b) $e^+e^- \longrightarrow b\bar{b}\nu\bar{\nu}\omega$ for (solid points) $a = 1$ and $b = 0$ (Standard Model) and (crossed points) $a = b = 0.5$.

$Hb\bar{b}$ coupling constants. Analysis of various differential distributions reveals that the most stringent bounds on the model parameters are achieved from the data on the $\cos\theta_{eb}$ distribution when the kinematic region is divided into 10 bin. The experimental error $\Delta\sigma_i^{\text{exp}}$ for the ith bin can be written as

$$\Delta\sigma_i^{\text{exp}} = \sigma_i^{\text{SM}}\sqrt{\delta_{\text{syst}}^2 + \delta_{\text{stat}}^2}, \quad (3)$$

where

$$\delta_{\text{stat}} = \frac{1}{\sqrt{\sigma_i^{\text{SM}}\varepsilon_{bb}\int\mathcal{L}dt}} \quad (4)$$

and δ_{syst}^2 is the sum of the squared systematic errors mentioned above.

Figure 4 shows the resulting limits on the parameters for a 500-GeV TESLA-like linear collider [2] for $M_H = 120$ GeV. We consider three possible total emittances of the collider: 100 fb^{-1}, 1, and 10 ab^{-1}. When the parameters Δa and b are independent, the admissible region (at 95% C.L.) is the region inside the circles. The horizontal straight lines correspond to the admissible region for the parameter b at $a = 1$. The vertical straight lines correspond to the admissible region for the parameter Δa at $b = 0$.

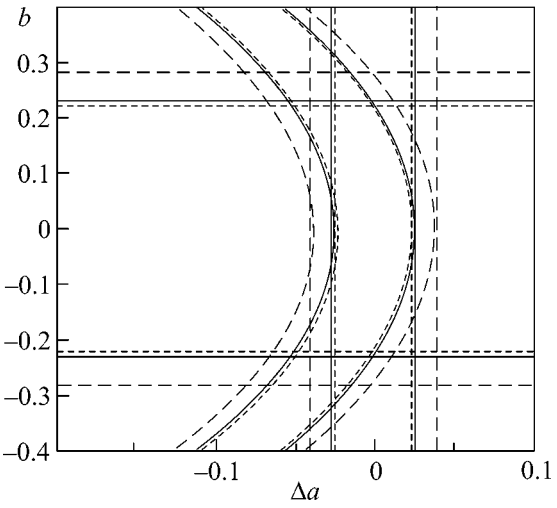

Fig. 4. Admissible regions of the parameters Δa and b (at 95% C.L.) for $\mathcal{L}$ = (long dashes) 100 fb^{-1}, (solid lines) 1, and (short dashes) 10 ab^{-1}. The region inside the corresponding concentric lines is the admissible region for two independent parameters Δa and b. The horizontal straight lines correspond to the admissible regions for the parameter b at $\Delta a = 0$. The vertical straight lines correspond to the admissible regions for the parameter Δa at $b = 0$.

At the 95% C.L., the following bounds can be obtained:

$$\begin{aligned} &-0.041 \le \Delta a \le 0.039 \quad \text{for} \quad \mathcal{L} = 100 \text{ fb}^{-1};\\ &-0.026 \le \Delta a \le 0.027 \quad \text{for} \quad \mathcal{L} = 1 \text{ ab}^{-1};\\ &-0.024 \le \Delta a \le 0.024 \quad \text{for} \quad \mathcal{L} = 10 \text{ ab}^{-1} \end{aligned} \tag{5}$$

for $b = 0$ and free Δa and

$$\begin{aligned} &-0.28 \le b \le 0.28 \quad \text{for} \quad \mathcal{L} = 100 \text{ fb}^{-1};\\ &-0.23 \le b \le 0.23 \quad \text{for} \quad \mathcal{L} = 1 \text{ ab}^{-1};\\ &-0.22 \le b \le 0.22 \quad \text{for} \quad \mathcal{L} = 10 \text{ ab}^{-1} \end{aligned} \tag{6}$$

for $\Delta a = 0$ and free b.

These results are more stringent than the bounds obtained in a similar analysis of the process with τ leptons in the final state by more than an order of magnitude, which is explained by the larger Yukawa coupling constant for b quarks and higher sensitivity of this process.

The resulting bounds can be extrapolated to the case of small variations in the Higgs boson mass near 120 GeV by multiplying by a factor of $(M_H/120 \text{ GeV})^2$.

3. CONCLUSIONS

The sensitivity of measurements concerning the $e^+e^- \longrightarrow b\bar{b}\nu\bar{\nu}$ processes at the future linear collider to new $Hb\bar{b}$ coupling constants, which are predicted in numerous extensions of the Standard Model, has been analyzed. As was shown, future experiments will enable one to detect possible deviations of the $Hb\bar{b}$ coupling constants from the Standard Model values with a high accuracy, and processes involving gauge bosons make an important contribution, experiments at a TESLA-like collider will be able to provide bounds of several percent on the parameter a (at fixed b) and tens of percent on the parameter b (at fixed a). These results are comparable with the data obtained in [2], where the relative accuracy of determining the Yukawa constant g_{Hbb} was predicted to be equal to 2.2% under a global fit to data at $\mathcal{L}$ = 500 fb^{-1} and $\sqrt{s}$ = 500 GeV.

The concluding remark concerning future measurements is as follows. Let us assume that new collider experiments concerning the Higgs boson will reveal deviation from the Standard Model predictions. In addition, let us assume that independent measurements of the partial width $\Gamma_{H \to b\bar{b}}$ (e.g., from the production of the Higgs boson at a muon collider) will be carried out. In this case, it is easy to see that $\Gamma_{H \to b\bar{b}} \sim (a^2 + b^2)$, while

$$\frac{d\sigma}{d\mathbb{O}} = A_0 + aA_1 + a^2A_2 + b^2A_3$$

for the observables in the $e^+e^- \longrightarrow b\bar{b}\nu\bar{\nu}$ process. Combining the above results and the data concerning $\Gamma_{H \to b\bar{b}}$, one can separate the contributions for a and b and obtain the explicit evidence of the *CP* violation in the Higgs sector.

We are grateful to A. Belyaev for stimulating discussions and valuable remarks. The work of A.L. was supported by Fapesp (grant no. 2001/0691-4). The work of A.Ch. and V.B. was supported by the Russian Foundation for Basic Research (project nos. 99-02-16558 and 00-15-96645), the Ministry of Education of the Russian Federation (project no. RF E00-33-062), and the U.S. Civilian Research and Development Foundation for the Independent States of the Former Soviet Union (grant no. MO-011-0). The work of R.R. was supported in part by Fapesp and CNPq.

REFERENCES

1. A. Chalov, A. Likhoded, and R. Rosenfeld, hep-ph/0205146; J. Phys. G.: Nucl. Part. Phys. **29**, 337 (2003).
2. R.-D. Heuer, D. J. Miller, F. Richard, *et al.*, hep-ph/0106315.
3. K. Desch and N. Meyer, *LC Notes*, LC-PHSM-2001-025, http://www.desy.de/lcnotes/2001/025/ww-fus.ps.gz.
4. M. Pohl and H. J. Schreiber, *SIMDET—A Parametric Monte Carlo for a TESLA Detector*, DESY Report 99-030 (1999).

Translated by R. Tyapaev

JETP Letters, Vol. 78, No. 1, 2003, pp. 13–16. Translated from Pis'ma v Zhurnal Éksperimental'noĭ i Teoreticheskoĭ Fiziki, Vol. 78, No. 1, 2003, pp. 16–20.

Transport and Optical Properties of Iron Borate $FeBO_3$ under High Pressures

I. A. Troyan[1], M. I. Eremets[2], A. G. Gavrilyuk[1], I. S. Lyubutin[3,*], and V. A. Sarkisyan[3]

[1] *Institute of High-Pressure Physics, Russian Academy of Sciences, Troitsk, Moscow region, 142090 Russia*

[2] *Max-Planck Institut für Chemie, 55020 Mainz, Germany*

[3] *Shubnikov Institute of Crystallography, Russian Academy of Sciences, Leninskiĭ pr. 59, Moscow, 119333 Russia*

**e-mail: lyubutin@ns.crys.ras.ru*

Received May 21, 2003

The optical absorption spectra of iron borate $FeBO_3$ were measured in diamond anvil cells at high pressures up to $P = 82$ GPa. The electronic transition with an abrupt jump in the absorption edge from ~3 to 0.8 eV was observed at $P \approx 46$ GPa. The resistance and its temperature dependence were directly measured for $FeBO_3$ at high pressures up to 140 GPa. It was established that the electronic transition at $P \approx 46$ GPa was accompanied by the insulator–semiconductor transition. In the high-pressure phase, the thermoactivation gap decreases smoothly at $46 < P < 140$ GPa approximately from 0.55 to 0.2 eV following the linear law. The extrapolated value of the pressure at which the sample becomes fully metallic is equal to about 210 GPa. © *2003 MAIK "Nauka/Interperiodica".*

PACS numbers: 72.15.Eb; 71.30.+h; 78.40.Kc; 72.15.Jf

Iron borate $FeBO_3$ belongs to the rare class of materials that are transparent in the visible region and possess spontaneous magnetization at room temperature. $FeBO_3$ crystal has the rhombohedral calcite structure [1]. At normal conditions, it is an antiferromagnet with weak ferromagnetism [2] and a Néel temperature of about 348 K [3]. At normal pressure, iron borate is an insulator with an optical gap of 2.9 eV [4]. By its electronic properties, $FeBO_3$ is a typical representative of the systems with strong electron correlation [5, 6]. Depending on the ratio between the Coulomb energy U (d–d gap) and the charge-transfer energy Δ (p–d charge-transfer gap), these materials can be either Mott insulators [5] or charge-transfer insulators [7–9]. Under high pressure, one can expect that such systems undergo the insulator–metal transition with a drastic change in their magnetic and optical properties [7, 10].

In our recent high-pressure experiments, we observed the magnetic moment collapse in iron borate at $P \sim 46$ GPa (at room temperature) [11, 12] and the structural phase transition at ~53 GPa with a jump of ~9% in the unit-cell volume [13]. The ^{57}Fe Mössbauer spectra also gave an indication of a drastic change in the electronic properties at $P \sim 46$ GPa, in particular, of the transition of Fe^{3+} ions from a high-spin ($S = 5/2$) to low-spin ($S = 1/2$) state [12]. Nevertheless, the question of metallization still remains open.

In this work, the resistance of the $FeBO_3$ crystal was directly measured at high pressures up to 140 GPa in a diamond anvil cell. For each pressure, the temperature dependence of resistance was also measured in the range 77–300 K. In addition, the behavior of the absorption edge in the optical spectra was studied up to 82 GPa. A jump in the optical gap was observed at 46 GPa. The behavior of the optical gap and of the conductivity activation energy indicates that, in the pressure range $P \sim 46$ GPa, the crystal undergoes a phase transition of the insulator–semiconductor type.

1. Optical absorption spectra. High-quality optically transparent $FeBO_3$ single crystals were grown from a solution in melt and were colored light green.

The optical absorption spectra were recorded over the pressure range up to 82 GPa at room temperature in a diamond anvil cell. The diamond anvil culets were about 400 μm in diameter. A hole at the center of rhenium gasket had a diameter of ~120 μm. For measurements, a platelet of size $\sim 50 \times 50 \times 5$ μm with plane coinciding with the basal plane (111) was split off from a bulky $FeBO_3$ single crystal. In the optical measurements, the light beam in the high-pressure cell was directed perpendicular to the crystal basal plane. Poly(ethyl siloxane) (PES-5) was used as a pressure-transmitting fluid providing quasi-hydrostatic conditions. After pressure release, the single crystal was not damaged. The optical setup for studying the absorption spectra at high pressure allows measurements in the visible and near-IR regions (from 0.3 to 5 μm). In the visible region, a photomultiplier FEU-100 was used as a detector, while, in the near-IR region, the light was detected by a germanium diode cooled to the liquid nitrogen temperature. The diameter of a light spot on the sample was on the order of 20 μm. To eliminate possible spurious signals, the reference signal I_0 was first

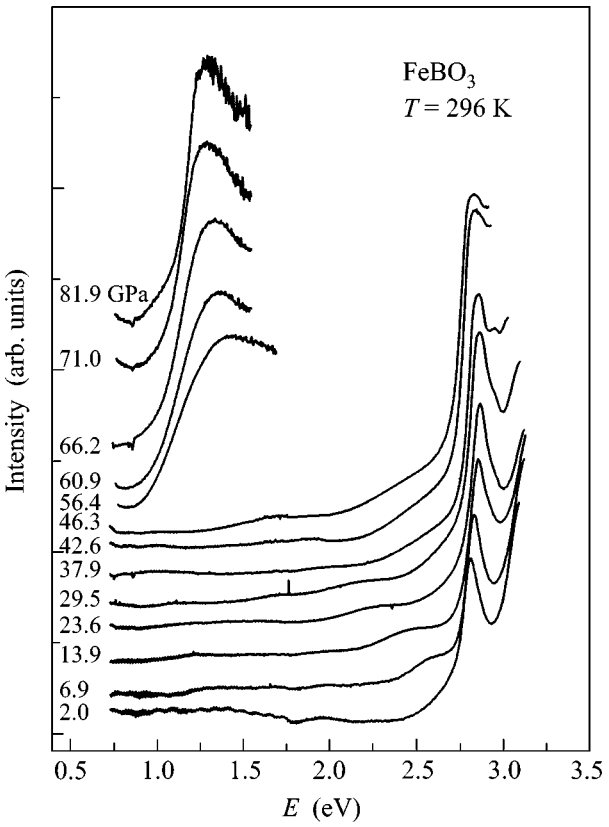

Fig. 1. Room-temperature absorption spectra of the $FeBO_3$ single crystal at different pressures.

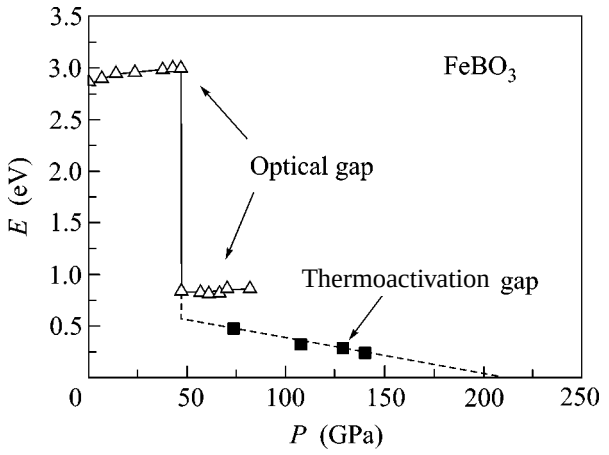

Fig. 2. Baric dependences of the optical absorption edge (room temperature) and the conduction thermoactivation energy (thermoactivation gap) obtained in the experiments on the electrical resistance of iron borate $FeBO_3$.

measured outside the sample, whereupon the signal I passed through the sample was measured. The absorption spectrum was calculated by the standard method from the formula $I = I_0\exp(-\alpha d)$, where d is the sample thickness and α is the optical absorption coefficient.

The evolution of optical absorption spectra of iron borate with an increase in pressure at room temperature is shown in Fig. 1. As P increases to 46 GPa, the energy of the optical absorption edge slowly increases, after which it drops abruptly from ~3 to ~0.8 eV at $P \sim$ 46 GPa, and then virtually does not change upon further buildup of pressure to 82 GPa (Fig. 2). The jump in the optical gap at 46 GPa correlates with the magnetic moment collapse observed earlier in [11] and with the spin crossover [12] in iron borate.

2. Setup for measuring resistance in a diamond anvil cell and the measurement technique. The high-pressure resistance was measured in a diamond anvil cell on a special setup (Fig. 3) in the High-Pressure Group at the Max Planck Institute (Mainz, Germany). The method of fabricating electrocontacts (leads) was designed by Prof. M.I. Eremts and successfully used up to pressures of 250 GPa [14]. The essence of this method is as follows. The metallic gasket is preliminary pressed in the cell to obtain a sharp imprint of the anvil culets. At the center of the imprint, a hole is drilled for visual verification (with illumination from below) of the arrangement of the sample and the electrocontacts. Then a thick layer of a mixture of epoxy resin and a micron-ground BN powder is applied to the gasket. After the resin was polymerized, the gasket is pressed with a force corresponding to one-half the maximal experimental pressure. The sample of a thickness of several microns is placed at the center of the prepared gasket.

Two pairs of crossed leads (Fig. 3) cut from a 2-μm-thick platinum foil are applied to the sample. This simulates the quasi-four-probe scheme of resistance measurement. The outer ends of the platinum electrocontacts are soldered to copper conductors that are firmly fixed to the cell frame and brought outside to connect with the measuring equipment.

The signals were measured using a two-channel digital "DSP Lock- in 7265" (Perkin-Elmer) lock-in detector. This instrument is equipped with high-quality 18-digit analogue-digital input converters (ADCs) operating in the frequency range from 0.01 Hz to 150 kHz. Further filtration and locked-in detection of the signal is performed digitally using a built-in processor. The instrument also contains a built-in generator of precision voltage with the amplitude from 5 V to 1 μV. In our measurements, the voltage frequency was 3 Hz, allowing the errors introduced by the contact potentials to be eliminated. In the general case, two channels of the DSP Lock-in 7265 detector operate simultaneously; channel A measures voltage, and channel B measures current. To measure the resistance of high-ohmic samples (higher than 1 GΩ), only channel B was used. In this case, the current through the sample was measured, while the voltage applied to the sample was assumed to be equal to the voltage of the driving generator. In addi-

tion, the instrument has an integrating 16-digit ADC, which was used for measuring voltage on a calibrated temperature gauge. The accuracy of temperature measurement was 0.1 K in the range 77–300 K. The software allows all the measured parameters to be recorded on a hard disk as functions of time and reading of the chosen channel.

For the high-pressure cell situated in a cryostat and connected to the measuring system, the leakage current was 0.5 pA at a pressure of 10 GPa (dielectric state of the sample). For this reason, the actual experimental accuracy of measurement was determined by the driving voltage generator. The resistance was measured for a driving voltage of 0.01 V with an error of 1 μV, which corresponded to an accuracy of 0.1%.

In our experiments, flat diamond anvils with a diameter of 180 μm were used. A $FeBO_3$ sample with a thickness on the order of 4 μm was placed at the center of a boron nitride gasket, so that there was no pressure-transmitting medium in this experiment. Micron-sized ruby chips were distributed over the sample. The pressure scatter between the two nearest electrodes in the sample was 3 GPa at a pressure of 100 GPa. This value was caused by the nonhydrostatic pressure component and taken as the error of pressure measurement.

The pressure was measured and fixed at room temperature. Then the cell connected to the measuring apparatus was placed in a helium blow-through cryostat. The temperature gauge was attached to the cell frame. The cell was cooled to 77 K for 3 h. For each fixed pressure, the temperature dependence of the resistance was measured for 8 h in the warming regime. During the cooling, the pressure variation was not controlled. The pressure was measured before and after the temperature cycle. It was established that, after warming, the pressure increased by 10%. In numerous earlier experiments, the pressure in the diamond anvil cell increased upon cooling and was not released after warming. For this reason, the pressure measured after cell warming was taken as the pressure on the sample in our experiment.

3. Results of resistance measurements and discussion. The study of electrical resistance of $FeBO_3$ was carried out up to a pressure of 140 GPa. For each fixed pressure, the temperature dependence of resistance was measured in the range 77–300 K with the aim to determine the conduction type (metallic or semiconducting) and calculate the activation energy in the case of nonmetallic conduction.

It was found that, over the entire pressure range attained in the experiment, the sample remained high-ohmic. Because of this, we measured the current through the sample. It turned out that the resistance of $FeBO_3$ became measurable only in the high-pressure phase after the electronic transition at $P > 46$ GPa. The temperature dependences of the resistance of $FeBO_3$ are given in Fig. 4a for the three pressure values 108.2, 128.2, and 140 GPa. One can see that this dependence

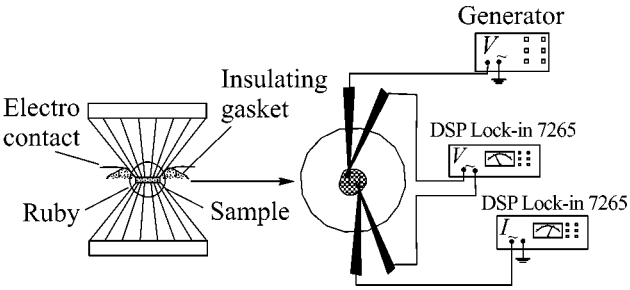

Fig. 3. Scheme of the experiment on measuring resistance at high pressures in a diamond anvil cell.

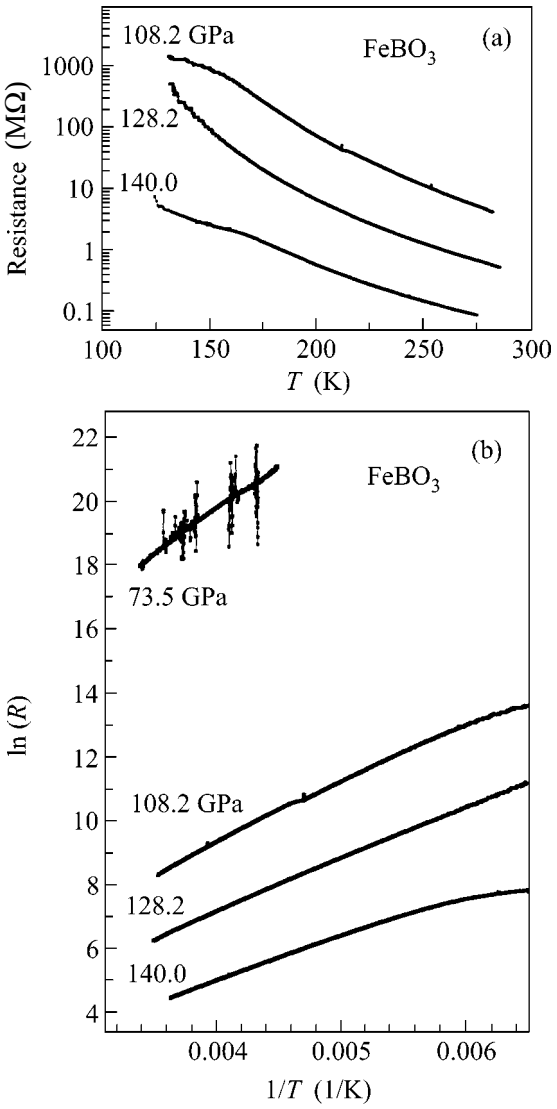

Fig. 4. (a) Evolution of the temperature dependence of the $FeBO_3$ resistance for various pressures and (b) the dependence of the logarithm of resistance on the reciprocal temperature.

is typical of semiconductors. The plots of the logarithm of resistance against the reciprocal temperature are presented in Fig. 4b for different pressures. Since

the temperature dependence of resistivity ρ obeys the law

$$\rho = \rho_0 \exp(E_t/2kT),$$

the activation energy E_t for the conductivity can be determined from the formula

$$E_t = 2k\frac{\partial \ln(\rho)}{\partial(1/T)}.$$

The calculated pressure dependences of the thermoactivation energies for conductivity in $FeBO_3$ are presented in Fig. 2. Immediately after the electronic transition at $P = 46$ GPa, the thermoactivation gap E_t equals 0.55 eV. In the high-pressure phase, the $E_t(P)$ gap decreases linearly to 0.2 eV with increasing pressure in the range $46 < P < 140$ GPa, allowing the parameters to be extrapolated to $E_t(0) = (0.70 \pm 0.04)$ eV and $dE_t/dP = -(0.0033 \pm 0.0004)$ eV/GPa. Therefore, the complete metallization occurs at a pressure of about 210 GPa.

At normal pressure, the high-spin Fe^{3+} $3d^5$ configuration is an analogue of an orbitally nondegenerate (single-band) Hubbard model with a half-filled band. Strong electron correlations lead to the charge-carrier localization [15]. One can assume that the phase transition at $P \approx 46$ GPa is accompanied by the spin crossover from a high-spin $(e_g^2\uparrow)(t_{2g}^3\uparrow)$ ($S = 5/2$) configuration of the Fe^{3+} ion to its low-spin $e_g^0(t_{2g}^3\uparrow)(t_{2g}^2\downarrow)$ ($S = 1/2$) configuration. The holes in the e_g shell can serve as current carriers providing semiconductor conduction [15]. With the buildup of pressure, the interionic distances shorten and the bandwidth increases because of strengthening of the cation–anion *d–sp* hybridization. This results in the carrier delocalization and increases the conductivity with pressure.

Note in conclusion that both the optical data and the resistance measurements indicate that, from the viewpoint of transport properties, the phase transition in iron borate at 46 GPa is the insulator–semiconductor phase transition.

This work was supported by the Russian Foundation for Basic Research (project no. 02-02-1364a) and the program "Strongly Correlated Electrons" of the Section of Physical Sciences of the Russian Academy of Sciences.

REFERENCES

1. I. Bernal, C. W. Struck, and J. G. White, Acta Crystallogr. **16**, 849 (1963).
2. M. P. Petrov, G. A. Smolenskiĭ, A. P. Pagurt, *et al.*, Fiz. Tverd. Tela (Leningrad) **14**, 109 (1972) [Sov. Phys. Solid State **14**, 87 (1972)].
3. R. Wolff, A. J. Kurtzig, and R. C. LeCraw, J. Appl. Phys. **41**, 1218 (1970).
4. I. S. Édel'man, A. V. Malakhovskiĭ, T. I. Vasil'eva, and V. N. Seleznev, Fiz. Tverd. Tela (Leningrad) **14**, 2810 (1972) [Sov. Phys. Solid State **14**, 2442 (1972)].
5. N. F. Mott, Proc. Phys. Soc. London, Sect. A **62**, 416 (1949); Can. J. Phys. **34**, 287 (1961); N. F. Mott, *Metal–Insulator Transitions*, 2nd ed. (Taylor and Francis, London, 1990; Nauka, Moscow, 1979).
6. S. Hufner, J. Osterwalder, T. Riesterer, and F. Hulliger, Solid State Commun. **52**, 793 (1984).
7. J. Zaanen, G. A. Sawatsky, and J. W. Allen, Phys. Rev. Lett. **55**, 418 (1985).
8. V. I. Anisimov, J. Zaanen, and O. K. Andersen, Phys. Rev. B **44**, 943 (1991).
9. S. Hufner, J. Osterwalder, T. Riesterer, and F. Hulliger, Solid State Commun. **52**, 793 (1984).
10. R. E. Cohen, I. I. Mazin, and D. G. Isaak, Science **275**, 654 (1997).
11. I. A. Troyan, A. G. Gavrilyuk, V. A. Sarkisyan, *et al.*, Pis'ma Zh. Éksp. Teor. Fiz. **74**, 26 (2001) [JETP Lett. **74**, 24 (2001)].
12. V. A. Sarkisyan, I. A. Troyan, I. S. Lyubutin, *et al.*, Pis'ma Zh. Éksp. Teor. Fiz. **76**, 788 (2002) [JETP Lett. **76**, 664 (2002)].
13. A. G. Gavriliuk, I. A. Trojan, R. Boehler, *et al.*, Pis'ma Zh. Éksp. Teor. Fiz. **75**, 25 (2002) [JETP Lett. **75**, 23 (2002)].
14. M. I. Eremets, V. V. Struzhkin, H. K. Mao, and R. J. Hemley, Science **293** (13), 272 (2001).
15. N. B. Ivanova, V. V. Rudenko, A. D. Balaev, *et al.*, Zh. Éksp. Teor. Fiz. **121**, 354 (2002) [JETP **94**, 299 (2002)].

Translated by V. Sakun

JETP Letters, Vol. 78, No. 1, 2003, pp. 17–20. Translated from Pis'ma v Zhurnal Éksperimental'noĭ i Teoreticheskoĭ Fiziki, Vol. 78, No. 1, 2003, pp. 21–25.

Direct Observation of Localized Exciton States in $CdS_{1-x}Se_x$ Solid Solutions

N. R. Grigor'eva, R. V. Grigor'ev, and B. V. Novikov

Research Institute of Physics, St. Petersburg State University, St. Petersburg, 198504 Russia

e-mail: N.Grigorieva@pobox.spbu.ru

Received June 4, 2003

A system of isolated localized exciton states corresponding to particular energies from the tail of the density of states is observed in $CdS_{1-x}Se_x$ crystals. From an analysis of the obtained photoluminescence excitation spectra, the boundary between the free and localized excitons and the length of the tail region of the density of localized states that make an essential contribution to radiative recombination are determined. It is shown that the localized and free excitons prove to be separated and represent two exciton subsystems. The energies of actual optical photons are accurately determined to be 23.6 ± 0.2 and 35.6 ± 0.3 meV for $CdS_{0.70}Se_{0.30}$ and 20.7 ± 0.2 and 31.4 ± 0.3 meV for $CdS_{0.50}Se_{0.50}$. © *2003 MAIK "Nauka/Interperiodica".*

PACS numbers: 71.35.-y

The energy states of excitons localized by the fluctuation potential play an important part in the formation of optical properties of solid solutions (SSs). The processes of exciton localization in SSs based on II–VI compounds have been most intensively studied for $CdS_{1-x}Se_x$ solid solutions [1–4]. Studying the emission relaxation times in $CdS_{1-x}Se_x$ crystals [2] allowed the spectral boundary of mobility separating the regions of free and localized excitons to be determined. The authors of [5] carried out a theoretical analysis of the photoluminescence (PL) spectra of the SSs under consideration with regard to the finite exciton lifetime and the exciton–phonon interaction. In this work, two models of a localized exciton were used for the most adequate description of experimental data in a wide range of compositions: (1) an exciton localized as a whole and (2) a system formed by an electron interacting with the averaged potential of a localized hole.

It is generally assumed that the emission of excitons localized on composition fluctuations is mainly exhibited in the low-temperature PL spectra of $CdS_{1-x}Se_x$ crystals in the range of concentrations from 3 to 60%. In this case, the PL spectrum consists of a relatively broad band located in the tail region of the density of exciton states and phonon replicas of this band [1–5]. As the temperature increases, the band of localized excitons decays and the emission of free excitons and donor–acceptor pairs and band–acceptor emission arise in the spectrum [3]. The important role of stacking faults in the formation of reflectance and PL spectra for $CdS_{1-x}Se_x$ crystals of various compositions was revealed in our works [6, 7].

In this work, we investigated the photoluminescence excitation (PLE) spectra and selectively excited PL spectra of crystals of SSs with compositions $CdS_{0.70}Se_{0.30}$ and $CdS_{0.50}Se_{0.50}$. The PLE spectra were studied for various regions of the no-phonon band and its phonon replicas.

Well-faceted crystals were obtained by sublimation at 950°C from the gas phase. The starting mixture was preliminarily homogenized by repeated sublimation. The sample had a well-defined shape of hexahedra. The faces studied were 1×3 mm in size on the average, and the thickness of samples varied from 0.1 to 1 mm. The samples were not doped specially in the process of growth, and their surfaces were not treated after the growth.

As was shown by x-ray spectrum analysis, x-ray diffraction analysis, and HRTEM studies, our samples exhibited a high degree of homogeneity. These samples were single-phase SSs without separating an individual CdS or CdSe component and represented single crystals composed of crystalline blocks having a hexagonal crystal structure and a structure with intermediate anisotropy [6, 7].

The excitation of the samples was carried out through a DFS-12 monochromator (with a spectral slit width of ~1.3 meV), and the emission was measured at a preset wavelength with the use of a DFS-24 monochromator (with a spectral slit width of ~ 0.13 meV). A DKsSh-150 lamp was used as the source of the continuous spectrum. All investigations were carried out at 4.2 K. The reflectance and PL spectra were studied on the same setup.

The PLE spectra were measured for 24 recording points of emission in the spectral range that included the no-phonon line and the first phonon replica from 2.246 to 2.195 eV for $CdS_{0.70}Se_{0.30}$ crystals and from 2.080 to 2.029 eV for $CdS_{0.50}Se_{0.50}$ crystals. Simulta-

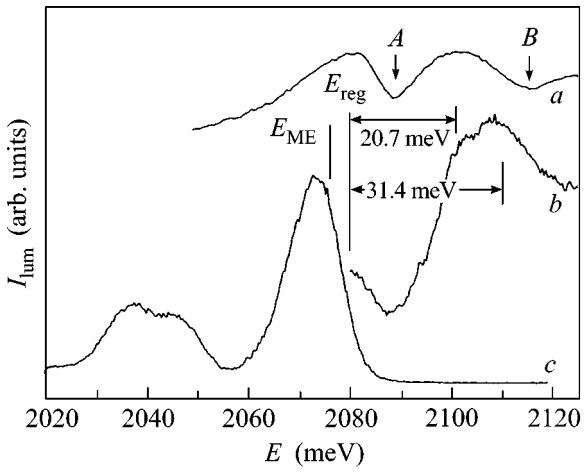

Fig. 1. Optical spectra of a $CdS_{0.5}Se_{0.5}$ crystal: (*a*) reflectance spectrum, (*b*) PLE spectrum in the region of short-wavelength PL decay (E_{reg} = 2.0799 eV), and (*c*) PL spectrum.

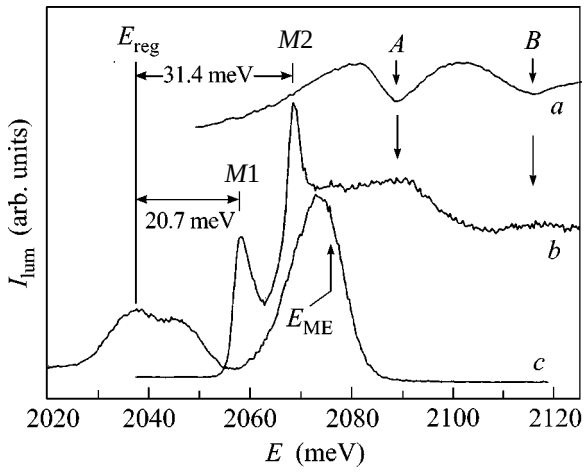

Fig. 2. Optical spectra of a $CdS_{0.5}Se_{0.5}$ crystal: (*a*) reflectance spectrum, (*b*) PLE spectrum in the region of the first phonon replica (E_{reg} = 2.373 eV), and (*c*) PL spectrum.

neously, the reflectance and PL spectra were measured at excitation in the region of intrinsic absorption.

The excitation spectra for two actual regions of the $CdS_{0.50}Se_{0.50}$ SS crystal are shown in Figs. 1 and 2. The PLE spectrum presented in Fig. 1 is typical for the emission recording region located in the short-wavelength wing of the no-phonon PL line. The spectral spacing between the features of the PLE spectrum and the energy position of the recording point can be related to the value of optical phonons. It is rather characteristic that decay in the PLE spectrum is observed in the region 2.101–2.083 meV, in which there is strong exciton absorption; that is, emission is slightly excited in this region, and fast relaxation through optical phonons is most probable.

Another typical PLE spectrum shown in Fig. 2 was obtained by recording emission in the region of phonon replicas of the PL spectrum. Two sharp peaks *M*1 and *M*2 are observed in its long-wavelength part. The spectral contour of these peaks is asymmetrical; it has a tail smoothly decaying toward high energies. The half-width of the spectral contour lies within the range 1–2 eV. The peaks arise at an energy of 2.076 eV and shift along the spectrum following the shift of the wavelength of the recorded emission. The distance between the spectral position of the peaks and the wavelength of the recorded emission always remains constant and equal to 20.7 ± 0.2 meV for *M*1 and 31.4 ± 0.3 meV for *M*2. The appearance and shift of the *M*1 and *M*2 peaks occur in the spectral range from 2.076 to 2.049 eV, that is, from the position of the no-phonon band maximum in the PL spectrum to the beginning of the region of the first phonon replica. The intensity of these peaks reaches a maximum inside the indicated range, sharply decays toward the short-wavelength region, and decays more slowly toward the long-wavelength region. Broad maxima corresponding to *A* and *B* excitons are observed in the short-wavelength part of the PLE spectrum for this recording range. The distance between the spectral position of the *M*1 and *M*2 peaks and the wavelength of the recorded emission for the $CdS_{0.70}Se_{0.30}$ SS crystals equals 23.6 ± 0.2 and 35.6 ± 0.3 meV, respectively. The appearance and shift of the *M*1 and *M*2 peaks in this case occur in the spectral range from 2.233 to 2.195 eV.

The differences in the PLE spectra recorded for different regions of the PL spectrum are associated with the action of different mechanisms of radiative recombination in the no-phonon PL band, namely, with the emission of free and localized excitons. The emission in the short-wavelength part (up to the maximum) of the no-phonon PL band in the $CdS_{1-x}Se_x$ crystals is mainly due to the emission of free excitons, and the emission in the longer wavelength part of the no-phonon band and in the region of phonon replicas is mainly due to localized excitons.[1]

The PLE spectra of free and bound excitons in binary II–VI compounds were comprehensively studied in the works [8, 9]. The authors of these works found that the exciton lifetime in the crystals plays an important part in the formation of the PLE spectra. If the exciton lifetime in the band exceeds the thermal equilibration time, the equilibrium distribution function is exhibited in the exciton PL spectrum. In this case, the shape of the PLE spectrum does not depend on the energy of the created exciton (it is probable that it can only depend on the exciton concentration in a certain

[1] The separate contribution of these mechanisms to the PL of the no-phonon band is also confirmed by our studies of the temperature dependence of the SS emission. As the temperature increases, the PL of localized excitons decays faster than the PL of free excitons; therefore, it is clearly seen how the free-exciton line is exhibited in the contour of the no-phonon band (in its short-wavelength part).

spectral region). In the case when the radiationless recombination time is long, the exciton lifetime becomes shorter than the thermal equilibration time. Here, only fast relaxation through optical phonons is manifested. Maxima associated with relaxation through optical phonons appear in the PLE spectrum.

An analysis of the PLE spectra indicates that the free excitons in SSs are characterized by a short lifetime and have no time to come into thermal equilibrium with the lattice; therefore, only fast relaxation with the participation of optical phonons is revealed in the spectrum. Two maxima with different intensities correspond to this mechanism in the PLE spectra presented in Fig. 1. These maxima are separated from the exciton line by the energies of optical phonons, 20.7 ± 0.2 and 31.4 ± 0.3 meV, respectively. In the similar spectrum for the $CdS_{0.70}Se_{0.30}$ SS, the corresponding two maxima are separated from the exciton line by approximately 23.6 ± 0.2 and 35.6 ± 0.3 meV.

This situation is especially well pronounced if the recording energy of the excited emission lies in the short-wavelength region of the PL spectrum formed by the free-exciton emission.

When the PLE spectrum is recorded in the region of phonon replicas (Fig. 2), it is naturally expected that the largest contribution to the PLE spectrum will be made by the resonantly excited stationary state shifted with respect to the registration energy (E_{reg}) by the optical phonon energy [1]. In this case, individual localized states can be directly observed in the spectrum recorded in the region of phonon replicas. The localized states that satisfy the above condition are manifested as narrow peaks. As E_{reg} is varied, these peaks shift along the continuous tail of the density of states. Therefore, the sharp peaks are always separated from the registration energy by the same value equal to the energies optical phonons that can propagate in $CdS_{1-x}Se_x$ SSs. The peak amplitude, depending on its energy position, is proportional to the population of the localized states and can be described based on the models proposed in [5].

The highest energy position of the sharp peak observed in Fig. 2 can be considered as the shallowest localized state, and the energy of this state can be used to estimate the position of the mobility edge E_{ME}. For the $CdS_{0.50}Se_{0.50}$ SS, it comprises 2.076 ± 0.001 eV. The position of the mobility edge with respect to the PL spectrum determined in this way corresponds to the calculated position obtained in the work [5] for the $CdS_{0.50}Se_{0.50}$ SS. The position of the mobility edge with respect to the PL spectrum for the $CdS_{0.70}Se_{0.30}$ SS is determined by a value of 2.233 ± 0.001 eV.

The significant intensity of the sharp peaks indicates that the exciton–phonon interaction is strong. The asymmetry of the spectral contour of these peaks can be explained by the relaxation of the localized exciton with the participation of acoustic phonons, which occurs within the supercluster.

It should be noted that sufficiently well-pronounced features are observed in the PLE spectra recorded in the region of phonon replicas (as in Fig. 2) in the region of excitons *A* and *B*. These features must be associated with the population mechanisms of the given localized state. As distinct from the PLE spectrum displayed in Fig. 1, the spectrum under consideration does not contain maxima associated with fast exciton relaxation. This indicates that the mechanism responsible in this case for the population of localized states is different from that in the case of the population of the states above the mobility threshold. The absence of phonon replicas designates that the mechanism of the formation of localized excitons by their localization as an entity is inefficient.

It is evident in Fig. 1 that only nonthermalized excitons with a short lifetime exist in the crystal. In this case, the formation of a localized exciton proceeds through a capture of an electron by a hole localized on a fluctuation. The hole is localized instantly, and the electron lives long and has time to be thermalized. This is due to the fact that composition fluctuations mainly change the valence band edge, whereas the conduction band is hardly distorted. Electron thermalization leads to the fact that only features associated with an increase in the electron concentration remain in the PLE spectrum.

Free electrons and holes can be created upon both their direct excitation and exciton dissociation. The process of exciton dissociation before their localization results in the fact that direct energy exchange between the systems of localized and free excitons is complicated. The localized and free excitons become separated and represent two exciton subsystems. These subsystems are separated by the so-called mobility edge. The transition of excitons as a whole to the tail of localized states is probably complicated because these states are commonly occupied by the rapidly localized hole.

The independence of the two exciton subsystems can be revealed by analyzing the phonon replicas of the selectively excited PL spectra. A model analysis that we performed based on [5] indicates that the phonon replicas in the spectrum obtained upon excitation above the mobility edge consist of the contribution of localized excitons and the contribution of free excitons. The contribution of the latter is described by the Maxwell–Boltzmann distribution. The PL spectra excited both above (Fig. 3a) and below (Fig. 3b) the mobility edge allow one to verify that these contributions are different. The position and shape of the phonon replicas in the selectively excited PL spectrum shown in Fig. 3b depend on the excitation energy. The shape of the phonon replicas reflects the population of a small region of the tail of the localized states and is described by the expression $\text{const}(\omega - \omega_0)^3\exp(-(\omega - \omega_0)/d)$, where *d* is a parameter depending on the length of the

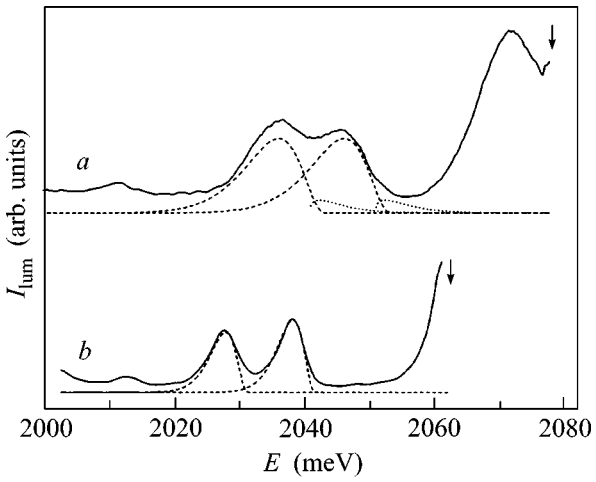

Fig. 3. Selectively excited PL spectra of a $CdS_{0.50}Se_{0.50}$ crystal (arrows indicate the exciting light energy): (*a*) the exciting light energy equals 2.0778 eV (the dashed lines indicate the model contour of the first phonon replicas from localized excitons; the dot line indicates that from free excitons) and (*b*) the exciting light energy equals 2.0623 eV (the dashed lines indicate the model contour of the first phonon replicas from localized excitons).

tail region of the localized states and ω_0 is the frequency shifted from the mobility edge (Fig. 3a) or from the excited light frequency (Fig. 3b) by the value of the optical phonon.

In conclusion, it should be noted that it turns out to be possible to observe the emission of excitons resonantly excited to particular localized states by PLE spectra. In other experiments, these states are manifested as a continuous spectrum (for example, in studying absorption spectra or PL upon excitation in the fundamental absorption region).

Thus, it proved to be possible to single out two mechanisms of emission in the $CdS_{0.70}Se_{0.30}$ and $CdS_{0.50}Se_{0.50}$ SSs by their PLE spectra. A system of separate localized states corresponding to particular energies from the tail of the density of states was observed. An analysis of the PLE spectra obtained in this work allowed the position of the boundary between the free and localized excitons to be determined at 2.076 ± 0.001 eV for the $CdS_{0.50}Se_{0.50}$ SS and 2.233 ± 0.001 eV for the $CdS_{0.70}Se_{0.30}$ SS. It was found that the localized and free excitons are separated and represent two exciton subsystems. These subsystems are separated by the so-called mobility edge. The length of the tail region of the density of localized states that make a significant contribution to radiative recombination was determined. It was found equal to 38 ± 1 meV for $CdS_{0.70}Se_{0.30}$ (in the range from 2.195 to 2.233 eV) and 27 ± 1 meV for $CdS_{0.50}Se_{0.50}$ (in the range from 2.049 to 2.076 eV). The energies of actual optical phonons were accurately determined and comprised 23.6 ± 0.2 and 35.6 ± 0.3 meV for $CdS_{0.70}Se_{0.30}$ and 20.7 ± 0.2 and 31.4 ± 0.3 meV for $CdS_{0.50}Se_{0.50}$.

This work was supported by the Russian Foundation for Basic Research, project no. 02-02-16690, and the Ministry of Education of Russian Federation together with the Administration of St. Petersburg, project no. PD02-1.2-272.

REFERENCES

1. E. Cohen and M. D. Sturge, Phys. Rev. B **25**, 3828 (1982).
2. J. A. Kassh, Arza Ron, and E. Cohen, Phys. Rev. B **28**, 6147 (1983).
3. S. Permogorov, A. Reznitsky, S. Verbin, *et al.*, Phys. Status Solidi B **113**, 589 (1982).
4. S. Permogorov, A. Reznitsky, S. Verbin, and V. Lysenko, Solid State Commun. **47**, 5 (1983).
5. A. A. Klochikhin, S. A. Permogorov, and A. N. Reznitskiĭ, Fiz. Tverd. Tela (St. Petersburg) **39**, 1170 (1997) [Phys. Solid State **39**, 1035 (1997)].
6. N. R. Grigorieva, R. V. Grigoriev, E. P. Denisov, *et al.*, J. Cryst. Growth **214/215**, 457 (2000).
7. B. V. Novikov, N. R. Grigorieva, B. A. Kazennov, *et al.*, J. Cryst. Growth **233**, 68 (2001).
8. E. F. Gross, S. A. Permogorov, V. V. Travnikov, and A. V. Sel'kin, Fiz. Tverd. Tela (Leningrad) **13**, 699 (1971) [Sov. Phys. Solid State **13**, 578 (1971)].
9. E. F. Gross, S. A. Permogorov, V. V. Travnikov, and A. V. Sel'kin, Fiz. Tverd. Tela (Leningrad) **14**, 1388 (1972) [Sov. Phys. Solid State **14**, 1193 (1972)].

Translated by A. Bagatur'yants

JETP Letters, Vol. 78, No. 1, 2003, pp. 21–24. Translated from Pis'ma v Zhurnal Éksperimental'noĭ i Teoreticheskoĭ Fiziki, Vol. 78, No. 1, 2003, pp. 26–29.

Coexistence of Antiferromagnetic and Paramagnetic Electronic Phases in Quasi-One-Dimensional $(TMTSF)_2PF_6$

A. V. Kornilov[1, 2], V. M. Pudalov[1, 2, *], Y. Kitaoka[3], K. Ishida[3], G.-q. Zheng[3], T. Mito[3], and J. S. Qualls[4]

[1] *Lebedev Physics Institute, Russian Academy of Sciences, Moscow, 119991 Russia*
[2] *Lebedev Research Center in Physics, Moscow, 119991 Russia*
**e-mail: pudalov@mail1.lebedev.ru*
[3] *Division of Material Physics, School of Engineering Science, Osaka University, Osaka 560-8531, Japan*
[4] *Wake Forest University, Winston-Salem, NC 27109, USA*
Received June 4, 2003

Phase transitions occuring in a quasi-one-dimensional organic compound $(TMTSF)_2PF_6$ near the boundaries between the paramagnetic metallic (PM), antiferromagnetic insulator (AFI), and superconducting (SC) states were studied experimentally. A controlled transition through the phase boundary was achieved by maintaining the sample at fixed temperature *T* and pressure *P*, while the critical pressure was tuned by varying a magnetic field *B*. When the PM/AFI phase boundary was crossed due to the variation of a magnetic field, history effects were observed: the resistance was found to depend on the trajectory described by the system before arriving at a given point (*P*–*B*–*T*) of the phase space. The results of the experiment give evidence for the formation of a macroscopically inhomogeneous state characterized by the inclusions of a minor phase that is spatially separated from the major phase. Away from the phase boundary, the homogeneous state is restored. After this, upon approaching the phase boundary in the back direction, the system exhibits no features of the minor phase up to the very boundary. © *2003 MAIK "Nauka/Interperiodica".*

PACS numbers: 75.30.Kz; 74.70.Kn; 75.30.Fv

The interplay (i.e., coexistence or competition) of the magnetic spin ordering and the superconducting electron pairing is a matter of considerable interest [1–3]. The phase diagram of quasi-one-dimensional $(TMTSF)_2PF_6$ is similar to that of cuprate superconductors. In the absence of a magnetic field, the phase diagram has a narrow pressure interval (≈0.53–0.6 GPa) within which a decrease in temperature leads to two sequential electronic phase transitions (Fig. 1) [3, 4]: first, from the paramagnetic metallic (PM) phase [5] to the antiferromagnetic insulator (AFI) phase with the formation of a spin-density wave and, second, from the AFI to the superconducting (SC) state. Figure 1 also shows the vertical trajectory $P = 0.54$ GPa, which intersects two phase boundaries (the two points of intersection correspond to second-order phase transitions). The intersection of the boundaries leads to changes in the resistance: it has a metallic character ($dR/dT > 0$) in the PM phase, activated character ($R \propto \exp(\Delta/T)$) in the AFI phase, and is zero in the SC phase.

Theoretically, in addition to the classical single-phase state of the system near the phase boundary, the appearance of heterophase states is also possible: for example, a microscopically mixed two-phase state or a macroscopically inhomogeneous state with a spatial phase separation. These states can be distinguished by studying the properties of the system in a close vicinity of the transition point. In particular, for an inhomogeneous state with inclusions of one phase in the other phase, one can expect some prehistory and hysteresis effects: the properties of the system at a given point of the *P*–*T* diagram may depend on the trajectory described by the system before arriving at this point. By contrast, there is no reason to expect any prehistory effects for the mixed state. In principle, two states can be distinguished by the qualitative difference that should be manifested in the transport characteristics when the system crosses the phase boundary upon varying pressure at a constant temperature. However, in practice, such an experiment is difficult to realize, because an *in situ* pressure sweep near 1 GPA at a temperature near 1 K causes considerable technical problems.

In this paper, we present the results of solving the aforementioned problem in a different way. From our magnetic-field measurements and from the results reported by other authors (e.g., [6]), it follows that an increase in a magnetic field is accompanied by a displacement of the AFI/PM boundary $T(P)$ toward higher temperatures. Since the field dependence of the boundary T_0 is smooth and monotonic, it is possible to control its position by magnetic field and, thus, to cause the system to cross the phase boundary by varying the magnetic field at a fixed pressure *P* and temperature *T*. This

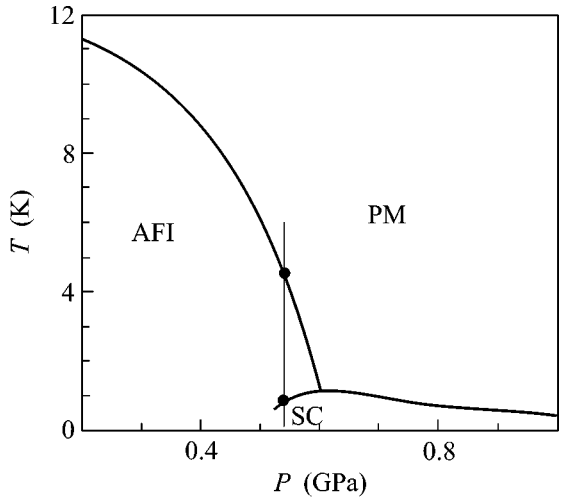

Fig. 1. Phase P–T diagram of $(TMTSF)_2PF_6$ in the absence of magnetic field. The phases in the plot are denoted as follows: PM is a paramagnetic metal, AFI is an antiferromagnetic insulator, and SC is a superconductor. The vertical line represents the isobaric trajectory $P = 0.54$ GPa. The dots on the trajectory indicate two phase transitions: from PM to AFI and from AFI to SC.

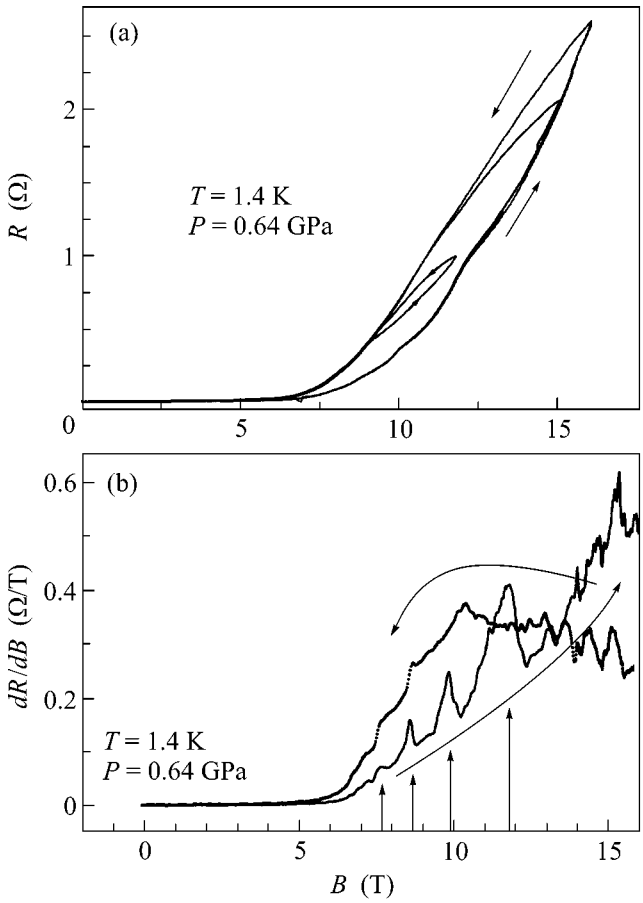

Fig. 2. (a) Dependence of the resistance on magnetic field in the case of crossing the PM/AFI boundary. The sharp increase in $R(B)$ at $B \approx 7$ T corresponds to the PM–AFI transition. (b) Dependence of the derivative dR/dB on magnetic field for the resistance shown in Fig. 2a in the increasing and decreasing magnetic field. The vertical arrows indicate the jumps in R, which correspond to the transitions between the FISDW phases.

experimental approach allowed us to perform measurements without using a smooth pressure sweep at low temperatures.

Our measurements showed that, when the system crosses the PM/AFI boundary at low temperatures ($T \lesssim 4$ K), its magnetoresistance exhibits strong prehistory effects: depending on the direction of the field sweep, the minor phase is observed away from the phase boundary, in the depth of the major phase. These effects directly indicate that, in the vicinity of the AFI/PM/SC phase boundary, the sample is in a macroscopically inhomogeneous heterophase state.

The samples were $(TMTSF)_2PF_6$ single crystals grown by the electrochemical method. Their typical dimensions were $2 \times 0.8 \times 0.3$ mm along the a, b, and c crystal axes, respectively. The sample under investigation and a manganin pressure gauge were placed in a nonmagnetic pressure cell [7] filled with a Si-organic pressure-transmitting liquid. The required pressure was produced in the cell at room temperature, after which the cell was slowly cooled (for ~12 h). The pressure cell with the sample was placed in a cryostat containing a superconducting solenoid. Measurements were performed in the cryostat with ^{4}He pumping. A magnetic field was directed along the c axis, and the measuring current was along the a axis. To realize the idea of the experiment, the initial values of P and T were chosen slightly above P_0 and T_0, so that the PM–AFI transition could occur with an increase in magnetic field.

For the initial point chosen in this way, the resistance was found to vary insignificantly with magnetic field increasing up to $B \approx 7$ T (Fig. 2a). As the field increases further, the resistance sharply increases by two to three orders of magnitude, which points to the transition from the metallic PM phase to the AFI phase. It should be noted that, starting with $B \approx 8$ T, nonmonotonic periodic resistance variations are observed on the background of the monotonically increasing resistance component, which are not typical of the AFI phase.

In the case of the back field sweep, i.e., when B decreases from 16 to 7 T, a strong hysteresis (~50%) is observed in the resistance (Fig. 2a) while the nonmonotonic component practically disappears. The hysteresis of $R(B)$ and the appearance and disappearance of the nonmonotonic component depend only on the field magnitude $|B|$ and do not depend on the field direction, i.e., $R(B) = R(-B)$ for the same history of varying quantity $|B|$. The hysteresis magnitude increases with increasing magnetic field. When the field sweep from 0 to 16 T is repeated, the dependence $R(B)$ described above is completely reproduced.

The nonmonotonic resistance component is more pronounced in the derivative dR/dB shown in Fig. 2b. It is significant that the nonmonotonic component is observed only when the field increases and disappears when the field decreases from 16 T to lower values. The vertical arrows in Fig. 2b indicate the positions of the boundaries between the phases of the field-induced spin-density wave (FISDW) [8] for the field sweep in the PM state [5] in the FISDW region. The positions of the peaks of dR/dB in Fig. 2b agree well with the expected boundaries of the FISDW phases. We emphasize again that the presence of these peaks would be natural for the PM state but is quite unexpected for the AFI state. The dependence $dR(B)/dB$ does not exhibit a peak at $B \approx 14$ T, which should be expected for the PM state [8]. The absence of this peak evidences a complete disappearance of the PM phase and the recovery of the homogeneous AF state in the field $B \geq 14$ T. In support of this interpretation, we note that, in stronger magnetic fields $B > 14$ T, one can see "rapid oscillations" (RO), which are characteristic of the AFI phase in $(TMTSF)_2PF_6$ (see Figs. 2b and 3) [9].

Figure 3 shows the field dependences of the derivative dR/dB for different temperatures. One can see that, as the temperature increases, the hysteresis observed in $R(B)$ for the forth and back field sweeps disappears. It is important that, at the low temperature $T = 1.4$ K, the hysteresis manifests itself not only in the magnitude of the resistance (or in dR/dB), but also in the qualitatively different behavior of the $R(B)$ dependence. When the field increases, the $R(B)$ dependence exhibits jumps (indicated by arrows for $B = 8$–12 T), which are characteristic of the FISDW phase transitions in the PM phase, although the system evidently transformed to the AFI phase starting with a field of ≈6 T (which is evidenced by the strong increase in the resistance in Fig. 2a and by the appearance of the ROs). In the back field sweep, these "anomalous" jumps are practically absent while the expected ROs are seen [9].

Discussion. Evidently, the results of our experiments do not agree with the behavior that should be expected for a microscopically mixed state with the two coexisting phases. In this state, the hysteresis effects and the dependence of the phase composition on the history cannot take place. The behavior described above is also not typical of the homogeneously "overcooled" or "overheated" phases in first-order phase transitions. In addition, for a second-order phase transition in a homogeneous system, which actually is the AFI–PM transition, no hysteresis or overheating/overcooling effects should occur. In the phase-space region where only the PM (or AFI) phase should exist, features of the opposite phase are evidently observed in addition to the expected features of the "correct" phase. Thus, the appearance of the hysteresis at the second-order transition and the evident features of both phases in the same phase-space region suggest that the phase composition of the system becomes inhomogeneous.

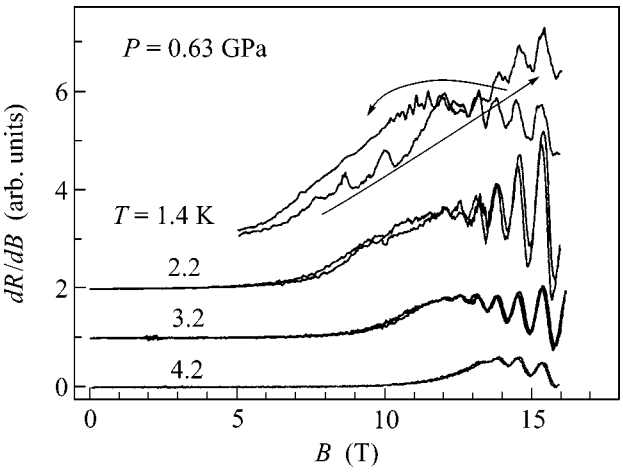

Fig. 3. Dependence of the derivative dR/dB on magnetic field for four different temperatures. One can see the fast disappearance of the hysteresis with increasing temperature and the nonmonotonic temperature dependence of the amplitude of "rapid oscillations."

The experiments described above demonstrate that the transition from metallic to antiferromagnetic state is accompanied by the appearance of a hysteresis in the dependence of the resistance on magnetic field. The results obtained from the experiments unambiguously indicate that, near the PM/AFI phase boundary, an inhomogeneous state with inclusions of the minor phase embedded in the major phase is formed. This conclusion agrees well with the data obtained earlier [4] from the isobaric temperature sweeps at $B = 0$. However, in contrast to the cited paper [4], our conclusion is based on the results that do not depend on any model assumptions about the spatial arrangement of the inhomogeneous state, because for the identification of the phase composition we used a qualitative difference in the behavior of the resistances in the AFI and PM phases. Note that the hysteresis of the magnitude and the character of the resistance variation is unrelated to any inhomogeneity of the sample and does not depend on time; it is a stationary and reproducible effect.

We are grateful to A.G. Lebed' and V. Podzorov for discussions. The work was supported by the NWO, INTAS, COE Research in Grant-in-Aid for Scientific Research (Japan), the Russian Foundation for Basic Research, the Presidential Program "Support of the Leading Scientific Schools," the Russian Federal Programs "Quantum Macrophysics," "Basic Research in Physical Sciences," and "High-Temperature Superconductivity," and the Scientific Program of the Russian Academy of Sciences "Strongly Correlated Electrons."

REFERENCES

1. J. Orenstein and A. J. Millis, Science **288**, 468 (2000).
2. N. D. Mathur, F. M. Grosche, S. R. Julian, *et al.*, Nature **394**, 39 (1998).

3. P. M. Chaikin, J. Phys. I (Paris) **6**, 1875 (1996).
4. T. Vuletić, P. Auban-Senzier, C. Pasquier, *et al.*, Eur. Phys. J. B **25**, 319 (2002).
5. For the simplicity sake, a "paramagnetic" phase implies metallic state at $P > P_0(T)$, which strictly speaking, is paramagnetic only in zero and weak magnetic fields. In a quantizing magnetic field, the magnetic-field-induced spin-density waves arise in this region of the P–T diagram [8].
6. N. Matsunaga, K. Yamashita, H. Kotani, *et al.*, Phys. Rev. B **64**, 052405 (2001).
7. A. V. Kornilov, V. A. Sukhoparov, and V. M. Pudalov, in *High Pressure Science and Technology*, Ed. by W. Trzeciakowski (World Sci., Singapore, 1996), p. 63.
8. A. V. Kornilov, V. M. Pudalov, Y. Kitaoka, *et al.*, Phys. Rev. B **65**, 60404 (2002); Synth. Met. **133–134**, 69 (2003).
9. So-called rapid oscillations (ROs) are observed in the AFI phase of $(TMTSF)_2PF_6$ [10]; their nature is not fully understood as yet and is the subject of discussion. In this work, it is significant that, for a one-dimensional Fermi surface, ROs do not reduce to the Shubnikov-de Haas oscillations; they depend nonmonotonically on temperature and, thus, are good indicators of the AF phase.
10. S. Uji, J. S. Brooks, M. Chaparala, *et al.*, Phys. Rev. B **55**, 12446 (1997), and references therein.

Translated by E. Golyamina

JETP Letters, Vol. 78, No. 1, 2003, pp. 25–29. Translated from Pis'ma v Zhurnal Éksperimental'noĭ i Teoreticheskoĭ Fiziki, Vol. 78, No. 1, 2003, pp. 30–35.

Two-Dimensional Quantum Ferromagnet, Magnetic Chains, and Oxygen Ordering in $La_2NiO_{4.125}$ Single Crystals

A. A. Nikonov* and O. E. Parfenov

Russian Research Centre Kurchatov Institute, pl. Kurchatova 1, Moscow, 123182 Russia

**e-mail: nikonov@isssph.kiae.ru*

Received June 4, 2003

The temperature dependence of the magnetic susceptibility $\chi(T)$ is studied in the region of the magnetic and charge ordering of $La_2NiO_{4.125}$ single crystals that differ in the degree of ordering of the excess oxygen. In the absence of the ordering of the excess oxygen, $\chi(T)$ obeys the dependence $\chi(T) \approx C/T^2$, which is explained by the formation of 1D FM Heisenberg chains of impurity states with $S = 1/2$. The ordering of oxygen creates favorable conditions for the formation of 2D FM Heisenberg lattices of impurity states with $S = 1/2$ that obey the exponential dependence $\chi(T) \approx C(T)^2\exp(4\pi JS^2/kT)$, which is an indication of the formation of a 2D quantum Heisenberg ferromagnet. © *2003 MAIK "Nauka/Interperiodica".*

PACS numbers: 75.30.Cr; 75.40.Cx; 75.10.Jm

In recent years, much attention has been attracted to studying unusual magnetic charge superstructures, so-called stripes. It is believed that it is in the microscopic mechanism of the generation of these objects that the keys to understanding phenomena like high-T_c superconductivity in cuprates and giant magnetoresistance in manganites [1] lie. At the same time, the expedience of describing stripes as an exceptionally new, exotic formation is subject to an intensive discussion by authors that use more "traditional" concepts (see M. Braden *et al.* [1]). Remaining within the framework of traditional concepts, some theoretical models suggest that doping the starting antiferromagnetic (AFM) dielectric compound gives rise to a subsystem of impurity complexes [2]. At a relatively low temperature, each of these complexes consists of an impurity and a hole localized in its vicinity. The hole is localized on the orbitals of atoms that belong to magnetic planes of the basic lattice, forming a complex impurity state. The crystal and magnetic lattices are strongly distorted in the region of the impurity state. More often, the process of hole localization at low concentrations is considered as the formation of a small-radius polaron bound with an acceptor [3]. This is a deep-level impurity model. As the concentration of holes increases, a tendency arises toward the ordering of oxygen into either one-dimensional chains or two-dimensional lattices [4], which are manifested as magnetic charge superstructures.

It is evident that the mechanism of the formation of such superstructures cannot be understood without understanding their unusual magnetic properties. The first stripes were observed in La_2NiO_{4+x} at $x \sim 0.125$ [5–7]; at present, their conducting and magnetic properties have been poorly understood; and only very limited data are known on magnetization and susceptibility [5, 8]. In addition, all these stripes were obtained in a strong magnetic field of ~1 T, which gives no way of carrying out a correct analysis of the temperature dependence $\chi(T)$. Such an analysis is an important independent source of information about the magnitude and sign of the exchange interaction J, the value of magnetic moments S, the character of magnetic anisotropy, and the dimensionality of the magnetic system.

The goal of this work was to study the magnetic properties of magnetic charge structures in a weak magnetic field and their correlation with the processes of oxygen ordering in $La_2NiO_{4.125}$ single crystals. This study led to observing a magnetic state that was described well by the model of a 2D quantum Heisenberg ferromagnet with $S = 1/2$.

In these investigations, La_2NiO_{4+x} single crystals with a mass of ~0.08 g grown by crucibleless zone melting [10] were used. The necessary oxygen concentration $x = 0.125(2)$ was gained by annealing at $T \approx 650$°C at the corresponding oxygen pressure [11] and was refined by the value of the crystal lattice parameter $c = 12.668(1)$ Å measured at room temperature [12]. The crystal lattice parameters and the occurrence and character of the ordering of the impurity oxygen were determined by x-ray diffraction analysis on a DRON3 setup. Neutron diffraction analysis performed on an IR-8 reactor at Kurchatov Institute Russian Research Center showed that the crystal possessed a high degree of bulk homogeneity with mosaicity that did not exceed 15' along the c axis. Magnetic properties were studied by measuring the initial magnetic susceptibility $\chi(T)$ in a weak alternating magnetic field $h = h_0\sin(wt)$, $h_0 = 1$ Oe, $f = 1$ kHz. The measurement procedure was described in detail in [13]. Simultaneously with the sus-

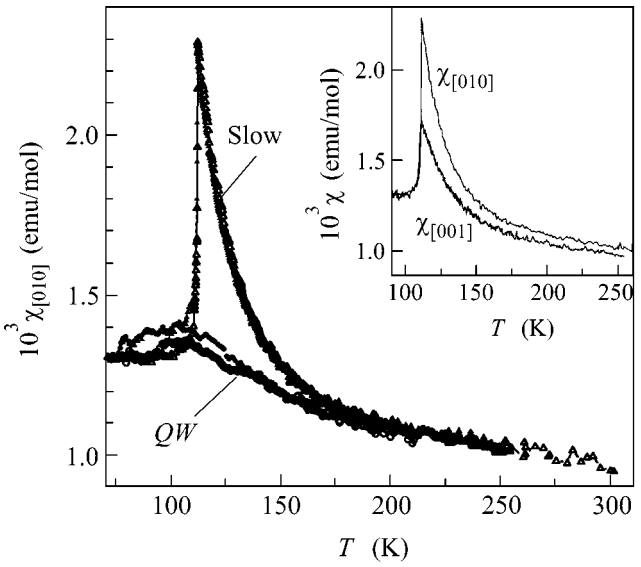

Fig. 1. Temperature dependence of the molar susceptibility $\chi_{[010]}(T)$ of a $La_2NiO_{4.125}$ single crystal. The *QW* symbol marks $\chi_{QW}(T)$. The inset displays $\chi_{[010]}(T)$ and $\chi_{[001]}(T)$.

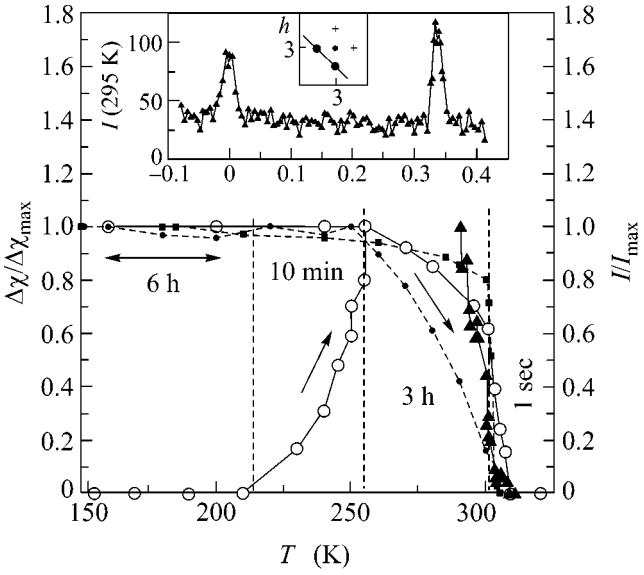

Fig. 2. Light circles show the behavior of $\Delta\chi(T)$ in low-temperature annealing. Black triangles represent the variation of the height of the intensity of the superstructure reflex $(3 - h, 2.67 + h, 0)$ displayed in the inset. Black circles and squares correspond to the data reported by Tranquada [7] and Nakajima [6], respectively.

ceptibility, the electrical resistance $R_{ab}(T)$ ($E \parallel ab$) was measured. The measurements were carried out by the four-contact method with a sample $1 \times 1 \times 0.5$ mm in size cut off from the main crystal. The contacts were made by baking a silver paste.

The experimental temperature dependence of the magnetic susceptibility $\chi_{[010]}(T)$ is shown in Fig. 1. We found no susceptibility anisotropy in the *ab* plane $\chi_{[100]} = \chi_{[010]} = \chi_{[110]}$, which may be associated with both the twinning of 1D FM chains [7] and the isotropic properties of the 2D lattice of magnetic polarons. Below 200 K, the behavior of $\chi_{[010]}(T)$ starts to deviate strongly from the behavior at $T > 200$ K. A stepwise decrease in $\chi_{[010]}$ accompanied by a small hysteresis is observed at $T_c = 110.5$ K, which is characteristic of first-order transitions. Upon cooling, the susceptibility value somewhat exceeds the value observed upon heating. This hysteresis correlates with the hysteresis of the superstructure wave vector of the magnetic charge structure observed below T_c in [9]. At the same time, as distinct from [5, 8], we found an anomalously strong growth of the transverse susceptibility $\chi_{[001]}(T)$ (inset in Fig. 1). At the temperature $T_c = 110.5$ K, the ratio $\chi_{[010]}/\chi_{[001]} \sim 2$. An application of additional constant longitudinal and transverse magnetic fields of ~1.5 kOe does not lead to a change in $\chi(T)$.

With the use of x-ray diffraction analysis, we found and investigated weak reflexes of the impurity superstructure (2.67, 3, 0) and (3, 2.67, 0). Scanning was performed along the $(3 - h, 2.67 + h, 0)$ direction. The reflexes obtained at 295 K are shown in the inset in Fig. 2. These reflexes indicate that the charge in the CuO_2 plane undergoes 2D modulation. It was found in [8] that the charge modulation (1/3, 0, 1) coincides with the spin modulation at $T > T_c = 110.5$ K. The variation of the intensity of these reflexes upon cooling is shown in Fig. 2 by black triangles. Each point was measured for ~30 min. The behavior of the intensity of the superstructure reflex and the temperature of its disappearance $T_O \sim 305$ K coincide with the data on oxygen ordering obtained by Tranquada [7] and Nakajima [6], which are presented in Fig. 2 by black circles and squares, respectively. The intensity of superstructure reflexes mirrors the process of oxygen ordering in our crystals. It is apparent that the long-range order in the arrangement of impurity atoms disappears above 305 K. After quenching from 320 down to 295 K, the superstructure reflex is restored in ~3 h. That is, in the case of sufficiently rapid cooling, strict order in the arrangement of the impurity atoms has no time to be established. By varying the rate of quenching and carrying out subsequent low-temperature annealings, we investigated the connection of the anomalous behavior of susceptibility with the degree of ordering of the impurity oxygen.

The dependence $\chi^{QW}_{[010]}$ obtained with a sample that was rapidly dipped, after heating to 320 K, into liquid nitrogen is presented in Fig. 1. As was expected, the quenching led to a strong decrease in the anomalous growth of $\chi_{[010]}(T)$. However, the susceptibility value below T_c and the hysteresis did not change after the quenching, which was confirmed by repeated tempera-

ture cycling from 78 to 200 K. Because oxygen remains immobile in this temperature range, $\chi^{QW}_{[010]}(T)$ and the hysteresis are determined exclusively by the ordering of holes.

The restoration of the anomaly $\Delta\chi(T_c) = \chi_{[010]}(T_c) - \chi^{QW}_{[010]}(T_c)$ with the use of annealing normalized to a maximum is shown in Fig. 2 by light circles. The hold time of a sample was different at different annealing temperatures. This time is indicated in the figure. The anomaly starts to grow rapidly upon warming above 210 K and attains a maximum value at ~250 K. Further warming tends to decrease the anomaly. At annealing temperatures in the range 250–300 K, the total hold time of samples necessary for attaining an equilibrium state is no less than 3 h. The ratio $\Delta\chi(250\ \text{K})/\Delta\chi(300\ \text{K}) \approx 3/2$. Upon heating above 303 K, the anomaly height decreases much faster. In this case, annealing is carried out by heating up to a prescribed temperature followed by immediate cooling. It is evident that the change $\Delta\chi$ upon annealing correlates with the behavior of the intensity of the superstructure reflex obtained from our x-ray diffraction data and from the neutron diffraction data [6, 7]. From this correlation, it follows that $\Delta\chi(T)$ is directly proportional to the number of ordered impurity atoms.

It is evident that the ordering process of impurity states participating in electron transport must affect the temperature behavior of conductivity. Experimental temperature dependences of the electrical resistance $R_{ab}(T) \sim R_0\exp(E/kT)$ and the activation energy $E(T) = d(\ln R_{ab})/dT^{-1}$ measured for the same sample, which was cooled at different rates (Fig. 3). The difference $\Delta R(T) = R^{Sl}(T) - R^{QW}(T)$ is shown in the inset. It is evident that the temperature dependences $\Delta\chi(T)$ and $\Delta R(T)$ are similar above T_c. However, the events associated with ordering are most pronounced in $E(T)$. The value $E \cong 400$ K indicates that a great part of holes at $T < 200$ K is localized on impurity states. At a temperature of 170 K, $E(T)$ exhibits a distinct peak. A strong decrease in $E(T)$ is observed below 130 K. At temperatures of 110 and 102 K, which correspond to magnetic charge transitions [9], sharp spikes exist in $E^{Sl}(T)$. It is known from the neutron diffraction data that the magnetic correlation length $\xi \sim 10$ Å (Nakajima [6]) at $T \sim 160$ K becomes equal to the average distance between impurity states [9]. Therefore, the occurrence of short-range order in the magnetic hole structure is the most probable reason for the appearance of a peak in $E(T)$ at 170 K. The short-range order is determined by the magnitude of the magnetic interaction J between the nearest impurity states or magnetic polarons and, therefore, is independent of the degree of oxygen ordering and the quenching rate. Because holes are strongly bound with the impurity oxygen atoms, the ordering of the impurity must be favorable to the relaxation of elastic strains in the crystal lattice and to the development of long-range order in the system of magnetic polarons. The sharp decrease in the activation energy $E(T)$ below ~130 K is most likely associated with the long-range order developing in the system of impurity states. Quenching leads to a decrease in the activation energy at $T > 115$ K, a shift of the kink temperature toward low temperatures, and the disappearance of spikes at 110 and 102 K, which are directly associated with the long-range order in the system of holes. The appearance of spikes at these temperatures and the disappearance of these spikes after quenching points to a change in the type of long-range order.

The dimensionality of the structure, the magnitude of the magnetic interaction between polarons J, and the value of the magnetic moment S can be determined from the temperature dependence of the susceptibility $\chi_{[010]}(T) = \chi_0 + \chi_S(T)$. Here we use the simplest suggestion that χ_0 is a weakly temperature-dependent part of the susceptibility and $\chi_S(T)$ is the contribution associated with the formation of the magnetic hole structure. When the power dependence $\chi_S \sim (T - T_c)^{-\gamma}$ is used, an unusually high value of the critical index $\gamma > 6$ is obtained. It is known that an anomalously high value of γ indicates that the susceptibility exponentially depends of the temperature, which is a distinctive feature of low-dimensional magnetic systems.

Several magnetic systems are known in which the susceptibility decreases by an exponential law with increasing temperature. Firstly, these are 1D Ising ferromagnetic chains of spins $S_{[010]} = 1/2$ with the anisotropic interaction $J_{[010]}$[14–19]. The longitudinal magnetic susceptibility of such chains under the condition $T < J/k$ obeys the equation

$$\chi_{\|\text{mol}}(T) = \chi_0 + f\frac{N_A g^2 \mu_B^2}{4k} T^{-1} e^{2J/kT}. \qquad (1)$$

Secondly, these are 2D FM Heisenberg lattices of spins S [18, 20, 21]. The magnetic susceptibility of a 2D quantum system at $T < J/k$ obeys the equation

$$\chi_{\text{mol}}(T) = \chi_0 + f\frac{N_A g^2 \mu_B^2}{3k} \times 5 \times 10^{-3} (S)^{-7} (J)^{-3} T^2 e^{4\pi JS^2/kT}, \qquad (2)$$

where f is the fraction of holes with respect to the number of Ni atoms, and $\chi_0 \sim$ const.

Let us suggest that polarons with $S = 1/2$ are ordered into 1D FM Ising chains. Fitting with the use of Eq. (1) gives the values $J/k = 240 \pm 20$ K and $\chi_0 = 9.6 \times 10^{-4}$ emu/mol. The fitting was carried out by the least-squares method. However, it is known that a maximum at $T_{\max} = 0.82J/k \sim 200$ K must be observed in the transverse susceptibility within the model of 1D FM Ising chains. The absence of such a maximum in the transverse susceptibility in the temperature range under study allows the model of 1D FM Ising chains with $S = 1/2$ to be declined.

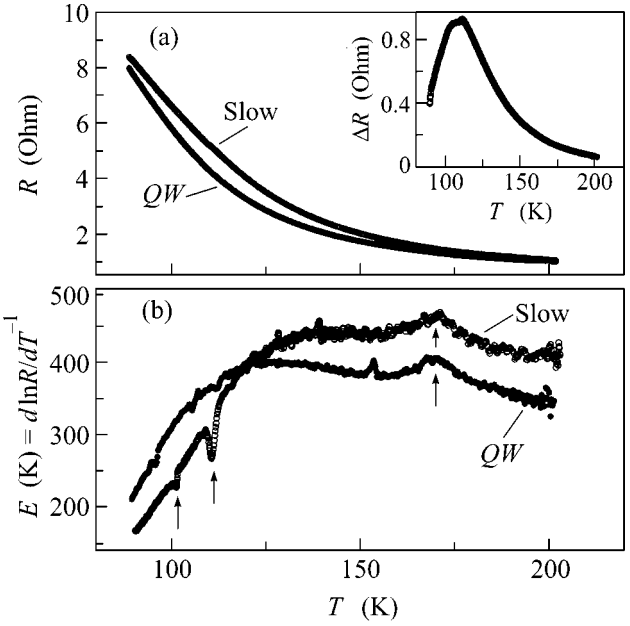

Fig. 3. (a) Temperature dependence of the electrical resistance $R_{ab}(T)$ of a sample slowly cooled down from 290 K and quenched from 320 K. The inset displays the difference $\Delta R_{ab}(T) = R^{Sl}(T) - R^{QW}(T)$. (b) Temperature dependence of the activation energy obtained at different cooling rates.

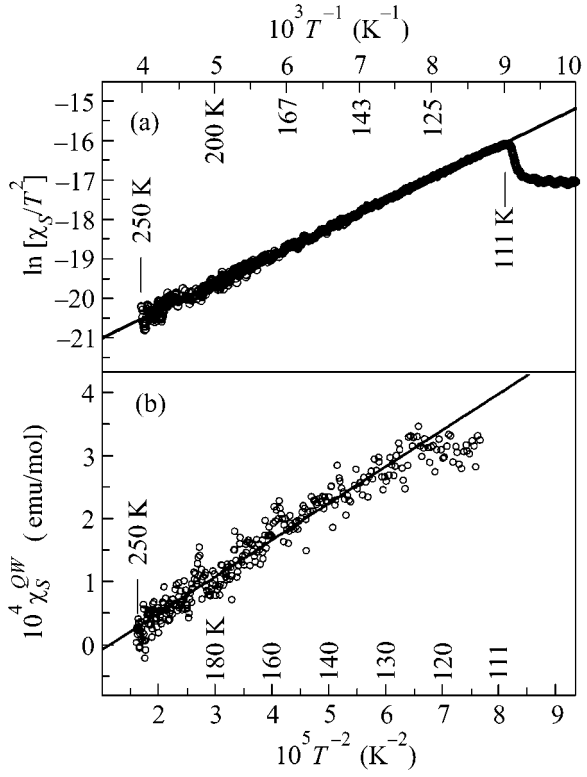

Fig. 4. Experimental values of the temperature dependence of the susceptibility $\chi_S(T) = \chi_{[010]}(T) - \chi_0$. Fitting dependences are shown in solid lines: (a) $\ln\{\chi_S(T)/T^2\} = -\ln C + 4\pi JS^2/kT$ and (b) $\chi_S^{QW}(T) = C/T^2$.

Suppose that the anomalous behavior of the susceptibility is associated with the formation of 2D FM Heisenberg lattices and obeys Eq. (2). The experimental dependence $\chi_S(T)$ is presented in Fig. 4a on a semilogarithmic scale as a function of the inverse temperature, $\chi_0 = 9.6 \times 10^{-4}$ emu/mol. The exponential behavior is clearly defined on these coordinates. The exponent was obtained by fitting $4\pi JS^2/k = 900 \pm 20$ K, which gives $J/k = 75 \pm 20$ K for $S = 1$, $S \longrightarrow \infty$ and $J/k = 300 \pm 20$ K for $S = 1/2$. The value $J/k = 75$ K does not satisfy the condition $T < J/k$ and drops out completely beyond the limits of the temperature range at hand. For the factor before the exponent, the fitting gives a value of 3.4×10^{-11} emu/mol. Substituting $J/k = 300$ K and $S = 1/2$, we obtain the share of the holes making a contribution to the anomaly $f \approx 3 \times 10^{-3}$. From here it follows, firstly, that a very small amount of holes (less than 5%) participates in the formation of the ferromagnetic lattice. Secondly, the value of the magnetic moment of the impurity state $S = 1/2$ correlates with the theoretical estimates of the value of the magnetic moment of polarons [2, 3].

From quenching experiments, we found that, because of the disordering of oxygen, the value of $J \sim$ const for a small decrease in the anomaly height. When the anomaly height becomes less than 50%, $\chi_S(T)$ ceases to obey the exponential dependence.

The feature observed in $\chi^{QW}_{[010]}(T)$ appears only slightly. Therefore, its analysis is of qualitative character. In the analysis of $\chi^{QW}_{[010]}(T)$, we use some evident assumptions about the behavior of the magnetic system. Firstly, from the general behavior of the susceptibility, it is evident that χ_0 is independent of quenching, and we may use the value obtained in the previous analysis. Secondly, the weak effect of the cooling rate on the behavior of the main features of $E(T)$ caused by the formation of short-range order and the weak variation of J with steadily increasing disorder indirectly indicate that the values of J and S are independent of quenching. The temperature dependence $\chi^{[010]}_{QWS}(T)$ is described well by the power law $\chi^{QW}_{[010]}(T) = \chi_0 + CT^{-\gamma}$. Fitting with the use of the least-squares method gives the values of the power $\gamma = 1.9 \pm 0.2$ and the coefficient $C = 5.5 \pm 0.5$ emu/mol. The quadratic dependence is shown in Fig. 4b in a more explicit form.

From the theory of critical phenomena, it is known that the value $\gamma \approx 2$ corresponds to either a 2D FM Ising lattice in the vicinity of $T \sim T_c$ or 1D FM Heisenberg chains at $T \leq J/k$. The values of T_c for various 2D Ising lattices are given in the review [17, p. 235]. For the square lattice, $kT_c = 2J/\ln(\sqrt{2} - 1) \approx 2.7J$. From our measurements, $T_c < 110$ K and $J/k \ll 110$ K; that is, the value of J/k proves to be much less than the lower boundary of the temperature range in which the fitting

was performed. This fact indicates that the application of the 2D Ising model to a quenched sample is incorrect.

Suppose that the behavior of $\chi_{QWS}^{[010]}(T)$ is determined by 1D FM Heisenberg chains. According to the theory [20, 22, 23], the susceptibility of 1D FM Heisenberg chains obeys the dependence

$$\chi_{\text{mol}} \cong \chi_0 + f\frac{N_A g^2 \mu_B^2}{k}\left(\frac{8|J|S^4}{3k}\right)T^{-2}. \quad (3)$$

Then, from the preceding analysis, it follows that the disordering of the impurity leads to a transition from the 2D FM Heisenberg lattice to a system of 1D FM Heisenberg chains. Setting the coefficient before T^{-2} equal to $C = 5.5$ emu/mol and taking $J/k \sim 300$ K and $S = 1/2$, we obtain $f \approx 0.1$, that is, 50% holes.

Thus, whereas 1D FM Heisenberg chains are formed even in the absence of the ordering of impurity oxygen atoms, the ordering of oxygen is the decisive factor in the formation of 2D FM Heisenberg lattices.

Based on an analysis of the anomalous behavior of the susceptibility $\chi(T)$ measured in a weak field, it is shown that the ordering of holes in $La_2NiO_{4.125}$ single crystals leads to the formation of 1D FM Heisenberg chains of bound polarons with the intrachain magnetic interaction $J/k = 300 \pm 20$ K and the magnetic moment $S = 1/2$. The ordering of the impurity creates favorable conditions for the formation of 2D quantum FM Heisenberg lattices of impurity states with $S = 1/2$ and the value of $J/k = 300 \pm 20$ K. Thus, $La_2NiO_{4.125}$ is a unique object for studying the properties of a 2D quantum Heisenberg ferromagnet, because the latter has been observed to date only in experiments with ^{3}He (see references in [21]).

The authors are grateful to D.A. Shulyat'ev for growing high-quality crystals, P.P. Parshin for help in performing neutron diffraction studies, and N.A. Chernoplekov and A.A. Zakharov for attention given to this work and valuable comments.

This work was supported by a State contract, project no. 107-1(00)-II.

REFERENCES

1. B. G. Levi, Phys. Today **51**, 19 (1998); R. F. Service, Science **283**, 1106 (1999); V. J. Emery, S. A. Kivelson, and J. M. Tranquada, Proc. Natl. Acad. Sci. USA **96**, 8814 (1999); M. Braden, M. Meven, W. Reichardt, *et al.*, Phys. Rev. B **63**, R140510 (2001).
2. V. J. Emery, Phys. Rev. Lett. **58**, 2794 (1987); R. J. Birgeneau, C. Y. Chen, D. R. Gabber, *et al.*, Phys. Rev. Lett. **59**, 1329 (1987); A. Aharony, R. J. Birgeneau, and A. Coniglio, Phys. Rev. Lett. **60**, 1330 (1988); L. J. Glazman and A. S. Ioselevich, Z. Phys. B: Condens. Matter **80**, 133 (1990).
3. A. O. Gogolin and A. S. Ioselevich, Zh. Éksp. Teor. Fiz. **98**, 681 (1990) [Sov. Phys. JETP **71**, 380 (1990)]; C. H. Chen, S.-W. Cheong, and A. S. Cooper, Phys. Rev. Lett. **71**, 2461 (1993); G. Seibold, E. Sigmund, and V. Hizhnykov, J. Supercond. **9**, 407 (1996); K. A. Muller, G. Zhao, K. Conder, and H. Keller, J. Phys.: Condens. Matter **10**, L291 (1998); T. Kasuya, Physica C (Amsterdam) **312**, 240 (1999); E. Winkler, F. Rivadulla, J.-S. Zhou, and J. B. Goodenough, Phys. Rev. B **66**, 094418 (2002); O. E. Parfenov, A. A. Nikonov, and S. N. Barilo, Pis'ma Zh. Éksp. Teor. Fiz. **76**, 719 (2002) [JETP Lett. **76**, 616 (2002)].
4. J. Zaanen and P. B. Littlewood, Phys. Rev. B **50**, 7222 (1994); Z. Hiroi, T. Obata, M. Takano, *et al.*, Phys. Rev. B **41**, 11665 (1990); T. Mizokavwa and A. Fujimori, Phys. Rev. B **56**, 11920 (1997); A. H. Castro Neto, Phys. Rev. Lett. **78**, 3931 (1997); B. P. Stojković, Z. G. Yu, A. R. Bishop, *et al.*, Phys. Rev. Lett. **82**, 4679 (1999).
5. K. Yamada, T. Omata, K. Nakajima, *et al.*, Physica C (Amsterdam) **221**, 355 (1994).
6. J. M. Tranquada, D. J. Buttrey, V. Sachan, and J. E. Lorenzo, Phys. Rev. Lett. **73**, 1003 (1994); K. Nakajima, Y. Endoh, S. Hosoya, *et al.*, J. Phys. Soc. Jpn. **66**, 809 (1997).
7. J. M. Tranquada, J. E. Lorenzo, D. J. Buttrey, and V. Sachan, Phys. Rev. B **52**, 3581 (1995).
8. J. M. Tranquada, P. Wochner, A. R. Moodenbaugh, and D. J. Buttrey, Phys. Rev. B **55**, R6113 (1997).
9. P. Wochner, J. M. Tranquada, D. J. Buttrey, and V. Sachan, Phys. Rev. B **57**, 1066 (1998).
10. A. M. Balbashev, D. A. Shulyatev, G. Kh. Panova, *et al.*, Physica C (Amsterdam) **256**, 371 (1996).
11. H. Tamura, A. Hayashi, and Y. Ueda, Physica C (Amsterdam) **258**, 61 (1996).
12. D. E. Rice and D. J. Buttrey, J. Solid State Chem. **105**, 197 (1993).
13. A. A. Nikonov, Prib. Tekh. Éksp., No. 6, 168 (1995) [Instrum. Exp. Tech. **38**, 807 (1995)].
14. V. L. Ginsburg and V. M. Fain, Zh. Éksp. Teor. Fiz. **39**, 1323 (1960) [Sov. Phys. JETP **12**, 923 (1960)].
15. S. Katsura, Phys. Rev. **127**, 1508 (1962).
16. M. E. Fisher, J. Math. Phys. **4**, 124 (1963); H. A. Kramers and G. H. Wannier, Phys. Rev. **60**, 252 (1941).
17. C. Domb, Adv. Phys. **9**, 164 (1960); Adv. Phys. **9**, 235 (1960).
18. D. S. Fisher and D. R. Nelson, Phys. Rev. B **16**, 2300 (1977).
19. Jill. C. Bonner and M. E. Fisher, Phys. Rev. **135**, A640 (1964).
20. M. Takahashi, Phys. Rev. Lett. **58**, 168 (1987); Phys. Rev. B **36**, 3791 (1987).
21. P. Kopietz and S. Chakravarty, Phys. Rev. B **40**, 4858 (1989).
22. M. E. Fisher, Am. J. Phys. **32**, 343 (1964).
23. M. Takahashi and M. Yamada, J. Phys. Soc. Jpn. **54**, 2808 (1985).

Translated by A. Bagatur'yants

JETP Letters, Vol. 78, No. 1, 2003, pp. 30–33. Translated from Pis'ma v Zhurnal Éksperimental'noĭ i Teoreticheskoĭ Fiziki, Vol. 78, No. 1, 2003, pp. 36–39.

Resonance Backscattering in Submicron Rings

A. A. Bykov[1, *], D. V. Nomokonov[1], A. K. Bakarov[1], O. Estibals[2], and J. C. Portal[2]

[1]*Institute of Semiconductor Physics, Siberian Division, Russian Academy of Sciences, pr. Akademika Lavrent'eva 13, Novosibirsk, 630090 Russia*

**e-mail: bykov@thermo.isp.nsc.ru*

[2]*Grenoble High Magnetic Fields Laboratory, MPI-FKF and CNRS B.P.166, F-38042 Grenoble, France*

Received June 5, 2003

Quasiperiodic peaks of the resistance as a function of gate voltage were observed in submicron rings fabricated on the basis of a two-dimensional electron gas in a GaAs quantum well with the AlAs/GaAs superlattice barriers. In magnetic fields higher than 1 T, the peaks disappeared. The negative magnetoresistance observed in the peak maxima is explained by the magnetic-field-induced suppression of the resonance backscattering that appears in the triangular quantum dots situated in the branching regions of a ring interferometer. © *2003 MAIK "Nauka/Interperiodica".*

PACS numbers: 73.23.-b; 72.20.My

The negative four-terminal magnetoresistance arising in the waist of a high-mobility two-dimensional electron gas (TEG) is one of the classical examples of charge-carrier backscattering in semiconductor microstructures [1]. This negative magnetoresistance has a classical nature and is due to an increase in the probability of charge-carrier passage through the waist upon a decrease in the cyclotron radius. In this case, the dependence $R_{4t}(V_g)$ of the four-terminal resistance on the gate voltage is caused by a change in the TEG concentration and waist width and has a monotonic nonresonant character.

In this work, it is established experimentally that, at low temperatures, the $R_{4t}(V_g)$ dependence in submicron rings fabricated on the basis of a high-mobility TEG exhibits quasiperiodic resistance peaks that disappear upon an increase in the magnetic field. The negative magnetoresistance observed in the peak maxima is explained by the magnetic-field-induced suppression of the resonance backscattering appearing at certain gate voltages in the rings under study.

The rings were fabricated on the basis of a TEG in a GaAs quantum well with the AlAs/GaAs superlattice barriers [2–4] by electron-beam lithography and ion-plasma etching. The TEG mobility and the concentration in the original structure grown from molecular-beam epitaxy at 4.2 K was $\mu = 4 \times 10^5$ cm^2/Vs and $n_s = 1.6 \times 10^{12}$ cm^{-2}, respectively. The atomic-force microscope (AFM) image of the ring is shown in Fig. 1a. The effective ring radius, as determined from the period of the h/e oscillations, was on the order of $r_{\text{eff}} \simeq 0.13$ μm. The AuTi/GaAs Schottky barrier was used as a planar gate. Experiments were carried out in the temperature range from 0.1 to 30 K in magnetic fields up to 5 T. The resistance was measured using the four-terminal scheme.

The schematic view of a ring with the depletion regions appearing along the etching edges is shown in

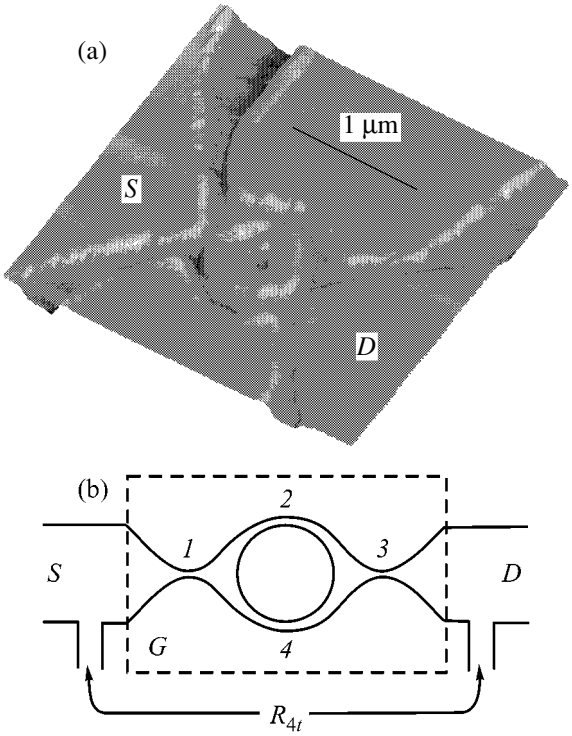

Fig. 1. (a) AFM image of the ring structure. (b) Schematic drawing of the ring: *1* and *3* are the input and output waists connecting the ring with the broad TEG regions; *2* and *4* are the waists arising in the ring; and *S*, *D*, and *G* denote, respectively, the source, the drain, and a planar gate.

Fig. 1b. The interferometer has four waists, which divide the ring in the tunneling regime into two triangular quantum dots [5, 6]. The waists at the ring input and output are denoted by *1* and *3*, and the waists inside the ring (interferometer arms) are denoted by *2* and *4*. The AFM image suggests that the resistances of waists *1* and *3* are higher than for waists *2* and *4*, because the surface of a semiconductor structure has small etching pits at the interferometer input and output [7].

The results of measuring R_{4t} as a function of gate resistance for different values of a magnetic field are shown in Fig. 2a. In the zero-field dependence, one can clearly see the gate peaks separated by about 0.05–0.07 V and completely disappearing in magnetic fields higher than 2 T. The gate peaks, on the background of the monotonically improved passage with increasing V_g, are due, in our opinion, to the resonances in the triangular quantum dots, which, as follows from the electrostatic calculations [5, 7], take place at the input and output of small rings. The application of a relatively weak magnetic field destroys these resonances.

The magnetic-field dependences of a four-terminal resistance for V_g (indicated by asterisks in Fig. 2a at the peak maximum and minimum between the peaks) are shown in Fig. 2b. In curve *1*, recorded at the peak maximum, one can clearly see a drastic decrease in the resistance with increasing magnetic field up to 0.5 T. Away from the resonance (curve *2* in Fig. 2b recorded at the minimum between the peaks in Fig. 2a), the magnetoresistance varies weakly. The negative magnetoresistance at the peaks can be qualitatively explained by the magnetic-field-induced suppression of the backscattering in an open triangular billiard [8], as is schematically shown in the figure for one (input) quantum point in the transmission regime, which is close to the open regime. In zero field, most electrons are scattered backward from the wall of the triangular quantum well, whereas, in the presence of a magnetic field that distorts their trajectories, the probability of passing through the triangular dot increases. However, this classical model does not explain the fact that the negative magnetoresistance disappears in the minima between the peaks.

The reflection resonances in the transmission regime intermediate between the open and closed rings (Fig. 2a) were observed up to 30 K, and their amplitude at temperatures below 4.2 K virtually did not change. However, at lower temperatures, the $R_{4t}(V_g)$ dependences in the high-ohmic region (in the closed regime) showed resistance peaks with maxima as high as 0.5–1 MΩ. A typical $R_{4t}(V_g)$ curve at a temperature of 0.1 K is shown in Fig. 3a. A gating peak with a magnitude of 350 kΩ is clearly seen. In the closed regime, tunnel waists appear in narrow regions *1* and *3* (Fig. 1b), while the ring is divided into two triangular quantum dots connected with each other laterally at the interferometer arms. In this situation, the gating is explicitly seen only upon lowering the temperature. As follows from Fig. 3a, the resistance peaks in this case become narrower and high-ohmic under the conditions of resonance reflection.

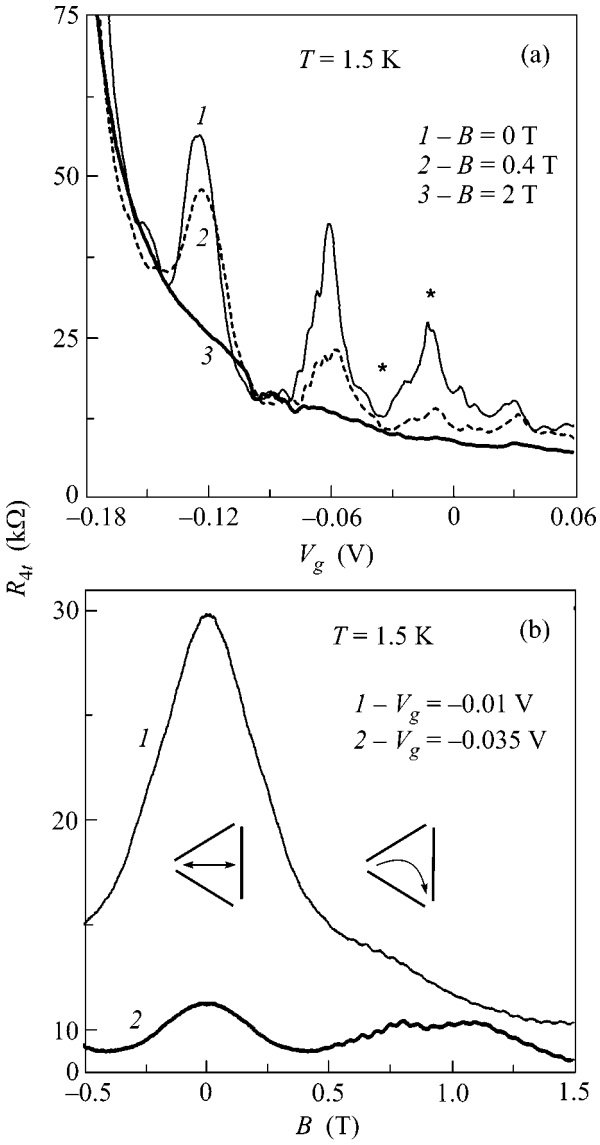

Fig. 2. (a) The $R_{4t}(V_g)$ dependence at T = 1.5 K in the regime close to the open regime for different B values: B = (*1*) 0, (*2*) 0.4, and (*3*) 2.0 T. Asterisks indicate the V_g values for which the $R_{4t}(B)$ dependences were measured. (b) The $R_{4t}(B)$ dependences at T = 1.5 K at the (*1*) maximum and (*2*) minimum in Fig. 2a. The classical electron trajectories in the triangular region are schematically shown in the inset for the cases of the absence and presence of a magnetic field.

Let us discuss the results obtained. In the closed regime, the experimental data should be analyzed in terms of quantum states in the triangular regions. In a triangular region modeled by the Hénon–Heiles potential, the three most characteristic states in the absence of a magnetic field are the "linear," "triangular," and "smile" states [9]. The evolution of these states in a magnetic field roughly describes the change in the char-

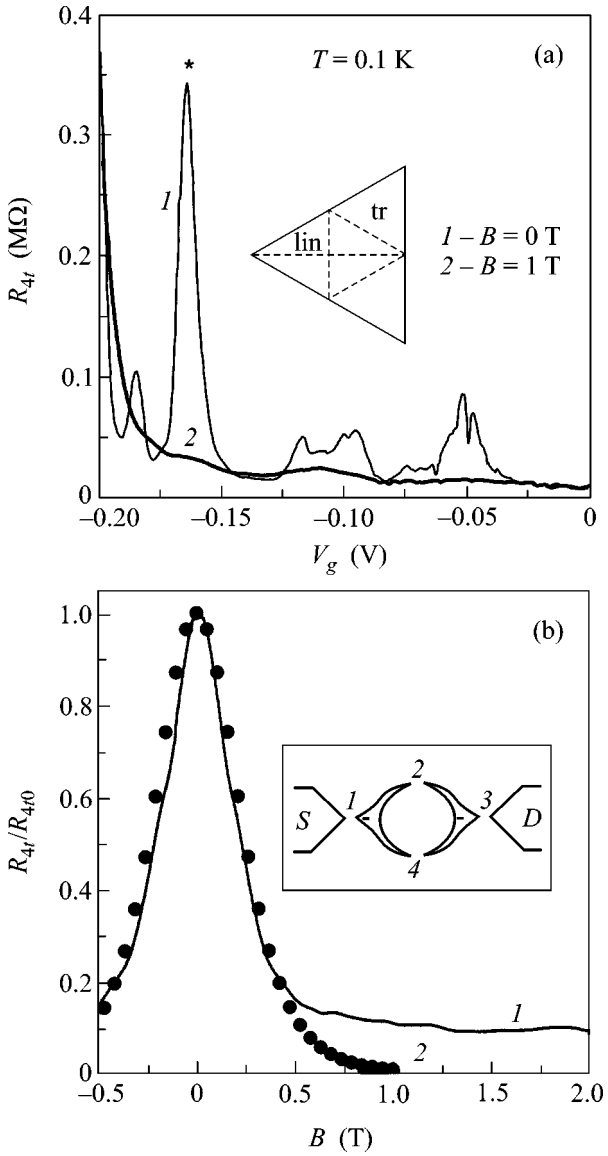

Fig. 3. (a) The $R_{4t}(V_g)$ dependence at $T = 0.1$ K in the closed regime for different B values: $B = (1)$ 0 and (2) 1.0 T. Asterisk indicates the peak for which the $R_{4t}(B)$ dependence was measured. Two characteristic quantum states in the closed triangular region are schematically shown in the inset: "lin" and "tr." (b) Experimental $R_{4t}(B)$ dependence of the ring in the closed regime at $T = 0.1$ K for the peak indicated by asterisk in Fig. 3a (*1*). (*2*) The calculated curve corresponding to the Raikh–Glazman model [10] with parameters $B_0 = 2.0$ T and $B_1 = 0.294$ T. A ring with four tunneling waists is schematically shown in the inset.

acter of electron passage through the triangular region with changing magnetic field. In the absence of a magnetic field, the greatest contribution to gating comes from the state with the wave function localized mainly along the triangle height. In the inset in Fig. 3a, it is denoted as "lin"). The tails of the wave function of this state very weakly overlap in the corner regions, where the triangles are joined together, which appreciably diminishes the probability of electron passage through the interferometer. Another characteristic state in the triangular region is triangular (denoted as "tr" in the inset in Fig. 3a), which is weakly bound to all three corners, because it is localized at the central region of the triangle. For this reason, in magnetic fields not strongly disturbing the spatial structure of this state, it should only slightly influence the transport through the triangular region [8]. The experimental dependence of the magnetoresistance in the closed ring-operation regime is shown in Fig. 3b.

The mechanism of negative magnetoresistance in such a system can qualitatively be described by the model suggested by Raikh and Glazman in [10]. In this model, a magnetic field appreciably strengthens the binding of the states in two quantum dots connected by tunneling through the saddle point. In our case, two triangular quantum dots are joined together by two waists (*2* and *4* in the inset in Fig. 3b). The main role in the transport is played by the states near the Fermi level. The binding of these states strongly depends on the overlap of their wave functions on both sides of the barrier. In zero magnetic field, this overlap is weak, because the wave functions at the input and output barrier cross-sections rapidly oscillate with different periods. In a magnetic field, the wave functions acquire an additional phase, which makes the periods of these oscillations closer and, hence, drastically increases the wave-function overlap. As a result, the magnetic field appreciably strengthens the binding of quantum dots, giving negative magnetoresistance of the form [10]

$$R(B)/R(0) = \exp(B^2/B_0^2)/\cosh^2(B/B_1).$$

The experimental curve for the negative magnetoresistance corresponding to the asterisked peak in Fig. 3a is shown in Fig. 3b together with the curve corresponding to the Raikh–Glazman model (both curves are normalized to the zero-field resistance). The parameters of the model for the calculated curve are $B_0 = 2.0$ T and $B_1 = 0.294$ T. With these parameters, the experimental and theoretical curves coincide well with each other at low fields $B \ll B_c$, where $B_c = B_0^2/B_1$ is the field for which the magnetoresistance in the model [10] is minimal.

The parameters B_0 and B_1 contain the geometric and energetic characteristics both of the tunneling saddle waists between the quantum dots and of the dots themselves. The values of these parameters coincide qualitatively with the parameters of triangular dots obtained in the model calculations [7] of small rings. This fact indicates that the saddle waists *2* and *4* are narrow and extended. This conclusion seems to be natural, if one recalls that, before their formation, these waists were open sections of the ring with the appropriate profile of the restricting potential. Unfortunately, the complicated character of the dependence of parameters B_0 and B_1 on the saddle geometry and energetics did not allow us to

gain more detailed information about the potential relief of the tunneling waists from the comparison of the experimental and calculated curves.

In summary, this work presents the experimental results on measuring the charge-carrier transport through individual submicron-sized rings based on a high-mobility TEG with high density. Quasiperiodic gating peaks have been observed as functions of gating voltage. Such a behavior is explained by the resonance electron backscattering in the triangular quantum dots at the ring input and output. The negative magnetoresistance at the peak maxima is qualitatively explained by the strengthening of binding between the triangular dots with an increase in the magnetic field and is in agreement with the Raikh–Glazman model.

We are grateful to A.V. Latyshev for the AFM characterization of the rings and to V.A. Tkachenko and O.A. Tkachenko for discussion of results. This work was supported by the Russian Foundation for Basic Research, project no. 01-02-16892.

REFERENCES

1. H. van Houten, C. W. J. Beenakker, P. H. M. Loosdrecht, *et al.*, Phys. Rev. B **37**, 8534 (1988).
2. K.-J. Friedland, R. Hey, H. Kostial, *et al.*, Phys. Rev. Lett. **77**, 4616 (1996).
3. A. A. Bykov, A. K. Bakarov, L. V. Litvin, and A. I. Toropov, Pis'ma Zh. Éksp. Teor. Fiz. **72**, 300 (2000) [JETP Lett. **72**, 209 (2000)].
4. A. A. Bykov, O. Estibals, I. V. Marchishin, *et al.*, Physica E (Amsterdam) **12**, 778 (2002).
5. O. A. Tkachenko, V. A. Tkachenko, D. G. Baksheev, *et al.*, Pis'ma Zh. Éksp. Teor. Fiz. **71**, 366 (2000) [JETP Lett. **71**, 255 (2000)].
6. A. A. Bykov, D. G. Baksheev, L. V. Litvin, *et al.*, Pis'ma Zh. Éksp. Teor. Fiz. **71**, 631 (2000) [JETP Lett. **71**, 434 (2000)].
7. V. A. Tkachenko, A. A. Bykov, D. G. Baksheev, *et al.*, Zh. Éksp. Teor. Fiz. **124** (2), 351 (2003) [JETP **97**, 317 (2003)].
8. L. Christiansson, H. Linke, P. Omling, *et al.*, Phys. Rev. B **57**, 12306 (1998).
9. M. Brack, R. K. Bhaduri, J. Law, and M. V. N. Murthy, Phys. Rev. Lett. **70**, 568 (1993).
10. M. E. Raikh and L. I. Glazman, Phys. Rev. Lett. **75**, 128 (1995).

Translated by V. Sakun

JETP Letters, Vol. 78, No. 1, 2003, pp. 34–37. Translated from Pis'ma v Zhurnal Éksperimental'noĭ i Teoreticheskoĭ Fiziki, Vol. 78, No. 1, 2003, pp. 40–44.

New Type of Exact Solutions to the Generalized Ashkin–Teller Model and Anisotropic Ising Model with Spin 3/2

V. M. Rozenbaum

Institute of Surface Chemistry, National Academy of Sciences of Ukraine, 03164 Kiev, Ukraine

e-mail: vrozen@mail.kar.net

Received May 20, 2003

The generalized Ashkin–Teller model involving both biquadratic and bilinear interactions between the Ising subsystems (σ and s) and equivalent to the anisotropic Ising model with spin 3/2 is considered. For a certain magnitude of the opposite-sign bilinear interactions along the horizontal and vertical axes of a square lattice, the exact analytic solution is obtained that describes the phase transition between the disordered ($\langle\sigma\rangle = \langle s\rangle = \langle\sigma s\rangle = 0$) and the correlated ordered ($\langle\sigma s\rangle \neq 0$ and $\langle\sigma\rangle = \langle s\rangle = 0$) states. © *2003 MAIK "Nauka/Interperiodica".*

PACS numbers: 64.60.Cn; 75.10.Hk

The exactly solvable two-dimensional lattice models in statistical physics play an important part in the theory of phase transitions [1]. They are developed due to their own logic that alludes to those modifications of the Hamiltonian for which new exact solutions can be obtained, as well as due to the problems associated with the description of phase transitions in various real systems, such as two-dimensional antiferromagnets [2], artificial two-dimensional lattices of ferromagnetic nanoparticles [3], and adsorbed molecular monolayers [4, 5]. Among the models allowing four states of a particle in the lattice site, the Ashkin–Teller model and a model with spin 3/2 is actively used. In essence, these models are equivalent (for the same number of interaction types between spins 3/2 and the same limitations on the parameters of these interactions), allowing the results obtained for a certain model to be extended to the other model [6, 7].

To describe the orientational phase transitions in systems with an essentially anisotropic multipolar Coulomb interaction, a more detailed study of the anisotropic models is necessary. For example, the phase transition in a square lattice of dipoles with four possible orientations along the square diagonals was considered using a short-range dipolar model reducible to the exactly solvable anisotropic Ising model [8]. In the case of four orientations of the molecular long axes along the axes of a square lattice, a more complicated situation arises because of the presence of fluctuation interactions between two Ising subsystems of spins 1/2 and the appearance of a new type of orientational order (occurrence of the preferable orientation of the molecular long axes in the absence of spontaneous polarization) [9]. It turned out that this new type of ordering allows an exact analytic description not only for the corresponding Bethe lattice [9] but also for a square lattice. It is the purpose of this work to show that (a) the most general formulation of the anisotropic model for spins 3/2 is equivalent to the generalized Ashkin–Teller model including not only the biquadratic but also the bilinear interactions between the Ising subsystems and (b) the generalized Ashkin–Teller model has the exact analytic solution at a certain magnitude of the opposite-sign bilinear interactions along the horizontal and vertical bonds (so-called fluctuation interactions).

The most general formulation of the anisotropic Ising model with the interactions between spin pairs $S_i = \pm 1/2$ and $\pm 3/2$ at the neighboring sites i and j of an arbitrary lattice is characterized by the Hamiltonian of the form [6, 7]

$$H = -\frac{1}{2}\sum_{i\neq j}\Big[J_{ij}S_iS_j + K_{ij}S_i^2S_j^2 + L_{ij}S_i^3S_j^3 + \frac{M_{ij}}{2}(S_iS_j^3 + S_i^3S_j)\Big] - \sum_i \Delta_i S_i^2. \quad (1)$$

The simplest relationship between spins S_i and a pair of spins σ_i, $s_i = \pm 1$ is given by

$$S_i = \sigma_i + \frac{1}{2}s_i. \quad (2)$$

Substitution of Eq. (2) into Eq. (1) gives the Hamiltonian in the σ, s variables:

$$H = -\frac{1}{2}\sum_{i\neq j}[J_{1,ij}\sigma_i\sigma_j + J'_{1,ij}s_is_j + J_{2,ij}(\sigma_is_j + s_i\sigma_j) + J_{4,ij}\sigma_is_i\sigma_js_j] - \sum_i\left[\left(\frac{5}{4}\sum_j J_{4,ij} + \Delta_i\right)\sigma_is_i + \frac{5}{4}\left(\frac{5}{8}\sum_j J_{4,ij} + \Delta_i\right)\right], \quad (3)$$

where new interaction parameters are introduced:

$$\begin{pmatrix} j_{1,ij} \\ J'_{1,ij} \\ J_{2,ij} \end{pmatrix} = \begin{pmatrix} 1 & 49/16 & 7/4 \\ 1/4 & 169/64 & 13/16 \\ 1/2 & 91/32 & 5/4 \end{pmatrix}\begin{pmatrix} J_{ij} \\ L_{ij} \\ M_{ij} \end{pmatrix}, \quad (4)$$

$$J_{4,ij} = K_{ij}.$$

A model with Hamiltonian (3) can be considered as the generalized Ashkin–Teller model. It is different from the original Ashkin–Teller model [10, 11] (see also [1]) in that the interaction parameters along differently oriented bonds (i, j) are different and that the bilinear interactions (proportional to the $J_{2,ij}$ parameters) between the Ising σ and s subsystems are included. The on-site σ_is_i interactions can be compensated through the appropriate choice of the parameters Δ_i. In [6], the conditions for reducing the Ising model with spin 3/2 to the standard Ashkin–Teller model were formulated; in our more general formulation, they are equivalent to the additional condition $J_{2,ij} = 0$ (a similar conclusion about the reducibility to the eight-vertex model, though with a condition less general than $J_{2,ij} = 0$, can be found in [7]).

Let us now turn to a square lattice. Assume that the parameters J_1, J'_1, and J_4 are identical along all the neighboring bonds and that $J_1 = J'_1$ and $\Delta = -5J_4$ (to compensate the on-site bilinear interactions). Let the system anisotropy consist only in that the interaction parameters $J_{2,ij}$ along the horizontal $(i, j = x)$ and vertical $(i, j = y)$ bonds are opposite in sign: $J_2 = J_{2,x} = -J_{2,y}$. The corresponding Hamiltonian is

$$H = \sum_{mn}[-J_1(\sigma_{mn}\sigma_{m+1,n} + s_{mn}s_{m+1,n} + \sigma_{mn}\sigma_{m,n+1} + s_{mn}s_{m,n+1}) - J_2(\sigma_{mn}s_{m+1,n} + s_{mn}\sigma_{m+1,n} - \sigma_{mn}\sigma_{m,n+1} - s_{mn}s_{m,n+1}) - J_4(\sigma_{mn}s_{mn}s_{m+1,n}\sigma_{m+1,n} + \sigma_{mn}s_{mn}\sigma_{m,n+1}s_{m,n+1})]. \quad (5)$$

A Hamiltonian of this form was introduced in [12] and, with $J_2 \approx 0.6J_1$, $J_4 \approx -0.2J_1$, and $J_1 \approx 0.8$ meV, described the orientational phase transition well in a 2×1 monolayer of CO molecules adsorbed at the NaCl(100) surface.

For $0 \le J_2 \le J_1$, the ground-state energies of this Hamiltonian and the corresponding spin distributions over the sites of a square lattice are given by

$$H_0 = \begin{cases} N(-4J_1 - 2J_4), & \sigma_{mn} = s_{mn} = 1, \quad J_4 > -J_1; \\ 2NJ_4, & \sigma_{mn}s_{mn} = (-1)^{m+n}, \quad J_4 < -J_1. \end{cases} \quad (6)$$

These states are degenerate with respect to the parameter J_2. The degeneracy also holds for an arbitrary relation between the parameters J_1 and J_2. For example, if $0 \le J_1 \le J_2$, the parameters J_1 and J_2 change places, and then the degeneracy occurs with respect to the parameter J_1. For arbitrary signs of parameters J_1 and J_2, of importance is which of the absolute values $|J_1|$ or $|J_2|$ is larger. In determining the ground-state structure, the larger value competes with $-J_4$ ($J_4 < 0$), while the smaller corresponds to the degeneracy parameter. Clearly, after redefining the spin variables, each of the resulting phase regions can be described by Hamiltonian (5) with the substitution $J_1 \longleftrightarrow J_2$ and/or changing signs of J_1 and J_2. For this reason, the statistical properties of all phase regions are identical, and, without loss of generality, one can restrict oneself to the consideration of the region $0 \le J_2 \le J_1$.

A particular case of Hamiltonian (5) with $J_4 = 0$ was considered in [9]. It corresponds to a quasi-dipolar model with four possible molecular orientations along the axes of a square lattice. In [9], the term "fluctuation interactions" was introduced for the bilinear s–σ interactions proportional to J_2 and not contributing to the ground state. Accordingly, we call the model characterized by Hamiltonian (5) the generalized Ashkin–Teller model with fluctuation interactions. The phase diagram of this new model is expected to be highly intricate, because each of the particular cases $J_2 = 0$ [1] and $J_4 = 0$ [9] is characterized by the presence of at least three phases: $\langle\sigma\rangle = \langle s\rangle = \langle\sigma s\rangle = 0$ (phase I), $\langle\sigma\rangle = \langle s\rangle \neq 0$ with $\langle\sigma s\rangle \neq 0$ (phase II), and $\langle\sigma\rangle = \langle s\rangle = 0$ with $\langle\sigma s\rangle \neq 0$ (phase III). The construction of a complete phase diagram (for J_2 and $J_4 \neq 0$) is a rather intriguing but as yet unsolved problem, which requires the use of certain approximate or numerical methods (in [9], e.g., the Bethe lattice with coordination number 4 and $J_4 = 0$ was considered, and the Monte Carlo modeling was performed on a square lattice). At present, only the exact solutions describing the phase transition between phases I and II in the trivial case $J_2 = J_4 = 0$ (two-dimensional Ising model) and in the case $-J_1 \le J_4 \le J_1$, $J_2 = 0$ are known [1]. For this reason, the new exact solution presented below for the transition between phases I and III in another particular case $J_1 = J_2$ is of special interest.

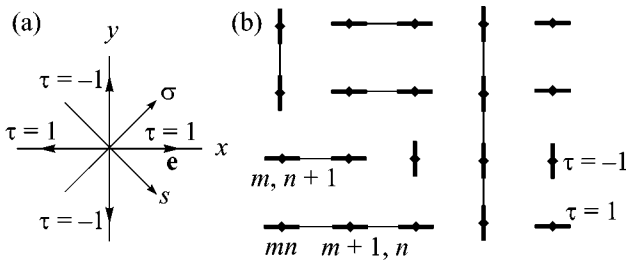

Fig. 1. (a) Scheme of the correspondence between four pairs of spin variables $\sigma_{mn} = \pm 1$ and $s_{mn} = \pm 1$ (or $\tau_{mn} = \sigma_{mn}s_{mn}$) and four orientations of the vector $\mathbf{e}_{nm}$. (b) Example of the distribution of spin variables over the sites of a square lattice. For the $J_1 = J_2$ case, the solid lines connect the interacting σ spins; the interaction energies are $\pm 4J_1$ (the sign is determined by the values of σ variables). After the summation over the states of σ spins, the effective interaction energy of a pair of neighboring τ_1 and τ_2 spins becomes equal to $-\tilde{J}\tau_1\tau_2$, where $\tilde{J}$ depends on temperature and is determined by Eqs. (10)–(12).

Let us introduce new spin variables τ_{mn} corresponding to the ground states given by Eq. (6),

$$\tau_{mn} = \begin{cases} \sigma_{mn}s_{mn}, & J_4 > -J_1; \\ (-1)^{m+n}\sigma_{mn}s_{mn}, & J_4 < -J_1. \end{cases} \tag{7}$$

The correspondence between the four pairs of possible values of spin variables and the four orientations of vector $\mathbf{e}_{mn}$ in the dipolar model, suitable for the graphical interpretation of the solution, is illustrated in Fig. 1a. In terms of the variables τ_{mn} and σ_{mn}, Hamiltonian (5) can be rewritten as

$$\begin{aligned} H = -\sum_{mn}\{&[J_1(1 \pm \tau_{mn}\tau_{m+1,n}) \\ &+ J_2(\tau_{mn} \pm \tau_{m+1,n})]\sigma_{mn}\sigma_{m+1,n} \\ &+ [J_1(1 \pm \tau_{mn}\tau_{m,n+1}) \\ &- J_2(\tau_{mn} \pm \tau_{m,n+1})]\sigma_{mn}\sigma_{m,n+1} \\ &+ J_4(\tau_{mn}\tau_{m+1,n} + \tau_{mn}\tau_{m,n+1})\}. \end{aligned} \tag{8}$$

Hereafter, the upper signs correspond to $J_4 > -J_1$ and the lower signs correspond to $J_4 < -J_1$ ($J_1 > 0$). For $J_1 = J_2$, the expressions in the square brackets can take only the two values $4J_1$ and 0. The first corresponds to the horizontal bond with $\tau_{mn} = \tau_{m+1,n} = 1$ or the vertical bond with $\tau_{mn} = \tau_{m,n+1} = -1$. In all other cases, the value is zero. This implies that the diagrammatic σ-expansion of the partition function using the identity $\exp(a\sigma) = \cosh a + \sigma\sinh a$ ($\sigma = \pm 1$) [13] contains only the horizontal and vertical chains sharing none of the lattice sites (Fig. 1b). The subsystem of σ spins becomes quasi-one-dimensional without long-range order, $\langle\sigma\rangle = 0$. Because of this, the summation over the 2^N states of σ spins will nullify all terms containing even one hyperbolic sine multiplier, so that the partition function takes the form

$$\begin{aligned} Z &= \sum_{\{\tau\},\{\sigma\}} \exp(-H/T) \\ &= 2^N \sum_{\{\tau\}} \prod_{mn} \{[\cosh K_1(1 + \tau_{mn})(1 \pm \tau_{m+1,n})] \\ &\quad \times [\cosh K_1(1 - \tau_{mn})(1 \pm \tau_{m,n+1})] \\ &\quad \times \exp[K_4(\tau_{mn}\tau_{m+1,n} + \tau_{mn}\tau_{m,n+1})]\} \end{aligned} \tag{9}$$

($K_j = J_j/T$, $j = 1, 2, 4$). Since the arguments of hyperbolic cosines take only two values $4K_1$ and 0, one can use the identity

$$\begin{aligned} \cosh(1 + \tau_1)(1 + \tau_2)K_1 &= \exp[(1 + \tau_1)(1 + \tau_2)\tilde{K}_1], \\ \tilde{K}_1 &= \frac{1}{4}\ln(\cosh 4K_1) \end{aligned} \tag{10}$$

to reduce the partition function to

$$\begin{aligned} Z &= 2^N(\cosh 4K_1)^{N/2} Z_{\text{Ising}}(\tilde{K}), \\ \tilde{K} &= \begin{cases} \tilde{K}_1 + K_4, & K_1 + K_4 > 0, \\ -\tilde{K}_1 + |K_4|, & K_1 + K_4 < 0. \end{cases} \end{aligned} \tag{11}$$

Here, $Z_{\text{Ising}}(\tilde{K})$ denotes the partition function of a two-dimensional Ising model with the effective Hamiltonian

$$\begin{aligned} H_{\text{eff}} &= -\tilde{J}\sum_{mn}[\tau_{mn}\tau_{m+1,n} + \tau_{mn}\tau_{m,n+1}], \\ \tilde{J} &= T\tilde{K}, \end{aligned} \tag{12}$$

where the interaction parameter $\tilde{J}$ depends on temperature and accounts for the thermodynamically averaged interaction of two neighboring σ spins. The temperature of the phase transition from a disordered ($\langle\tau\rangle = 0$) to the correlated ordered ($\langle\tau\rangle \neq 0$) state is found from the equation $\sinh 2\tilde{K} = 1$ for the critical temperature of a two-dimensional Ising model:

$$\begin{aligned} &\cosh 4K_1 \\ &= \begin{cases} (3 + 2\sqrt{2})\exp(-4K_4), & K_1 + K_4 > 0 \\ (3 + 2\sqrt{2})^{-1}\exp(-4K_4), & K_1 + K_4 < 0. \end{cases} \end{aligned} \tag{13}$$

The phase diagram of the generalized Ashkin–Teller model with fluctuation interactions is shown in Fig. 2 for the particular case $J_1 = J_2$. The coexistence lines for phases I and III are determined from Eq. (13). The points with $K_1 = K_2 = 0$ and $K_4 = \pm 0.4407$ (circular marks in Fig. 2) correspond to the critical values of a two-dimensional Ising model with respect to the spin

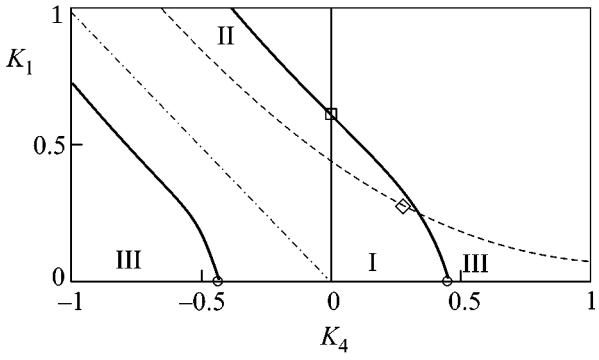

Fig. 2. Phase diagram of the generalized Ashkin–Teller model for the particular cases $J_1 = J_2$ (solid lines separating phases I and III) and $J_2 = 0$ (dashed lines separating phases I, II, and III in the region $K_4 > -K_1$). The singular points discussed in the text are marked.

variable τ. The point with $K_4 = 0$ and $K_1 = K_2 = 0.6121$ (square mark in Fig. 2) determines the exact value $T_c = 1.6337J_1$ of the phase-transition temperature in a quasi-dipolar model with four possible molecular orientations along the axes of a square lattice. The value $T_c = 1.94J_1$ obtained in [9] for the corresponding Bethe lattice can be regarded as the result of the cluster approximation for a square lattice.

It is of interest to compare our phase diagram with the Ashkin–Teller diagram with $J_2 = 0$. The phase-separation lines for phases I and III contain the same points $K_1 = 0$ and $K_4 = \pm 0.4407$. Whereas the I–III lines in the left part of the diagram has the same asymptotic value $K_1 = -K_4$, the I–III line for $K_2 = 0$ in the right part reaches the bifurcation point $K_1 = K_4 = 0.2747$ (rhombic mark in Fig. 2) that corresponds to the coexistence of three phases (dotted lines in Fig. 2). It is easy to understand that, as the parameter J_2 increases, the region occupied by phase II is expelled by phase III, and the bifurcation point moves up and to the left, approaching the line $K_1 = -K_4$ at $J_2 \longrightarrow J_1$.

Note in conclusion that we have obtained the exact analytic solution for the generalized Ashkin–Teller model, in which the parameter J_2 of bilinear fluctuation interactions between Ising subsystems is equal to the parameter J_1 of bilinear interactions between the neighboring spins in each subsystem. The phase diagram constructed for this solution shows that phase III ($\langle \sigma s \rangle \neq 0$ at $\langle \sigma \rangle = \langle s \rangle = 0$) can arise due not only to the biquadratic but also to the bilinear interactions between the Ising subsystems (the latter type of interactions is also typical of the anisotropic model with spin 3/2 and of the dipolar model). Our exact solution provides the key to understanding the formation mechanism of phase III. At $J_2 = J_1$, one of the spin subsystems becomes quasi-one-dimensional, allowing the explicit summation of the partition function over the states of this spin subsystem. Then the result of the summation over the states of the second spin subsystem is formally expressed through the partition function of a two-dimensional Ising model with an unusual interaction parameter that results from the thermodynamic averaging over the spins of the first subsystem.

REFERENCES

1. R. J. Baxter, *Exactly Solved Models in Statistical Mechanics* (Academic, London, 1982; Mir, Moscow, 1985).
2. C. L. Henley, Phys. Rev. Lett. **62**, 2056 (1989).
3. S. A. Gusev, Yu. N. Nozdrin, M. V. Sapozhnikov, and A. A. Fraerman, Usp. Fiz. Nauk **170**, 331 (2000) [Phys. Usp. **43**, 288 (2000)].
4. V. M. Rozenbaum, V. M. Ogenko, and A. A. Chuĭko, Usp. Fiz. Nauk **161** (10), 79 (1991) [Sov. Phys. Usp. **34**, 883 (1991)].
5. V. M. Rozenbaum and S. H. Lin, *Spectroscopy and Dynamics of Orientationally Structured Adsorbates* (World Sci., Singapore, 2002).
6. T. Horiguchi and Y. Honda, Prog. Theor. Phys. **93**, 981 (1995).
7. N. Sh. Izmailyan, Pis'ma Zh. Éksp. Teor. Fiz. **63**, 270 (1996) [JETP Lett. **63**, 290 (1996)].
8. V. M. Rozenbaum and V. M. Ogenko, Pis'ma Zh. Éksp. Teor. Fiz. **35**, 151 (1982) [JETP Lett. **35**, 184 (1982)].
9. V. M. Rozenbaum and A. N. Morozov, Pis'ma Zh. Éksp. Teor. Fiz. **75**, 756 (2002) [JETP Lett. **75**, 631 (2002)].
10. J. Ashkin and E. Teller, Phys. Rev. **64**, 178 (1943).
11. R. V. Ditzian, J. R. Banavar, G. S. Grest, and L. P. Kadanoff, Phys. Rev. B **22**, 2542 (1980).
12. V. M. Rozenbaum and S. H. Lin, J. Chem. Phys. **112**, 9083 (2000).
13. L. D. Landau and E. M. Lifshitz, *Statistical Physics*, 3rd ed. (Nauka, Moscow, 1976; Pergamon Press, Oxford, 1980), Part 1.

Translated by V. Sakun

JETP Letters, Vol. 78, No. 1, 2003, pp. 38–50. Translated from Pis'ma v Zhurnal Éksperimental'noĭ i Teoreticheskoĭ Fiziki, Vol. 78, No. 1, 2003, pp. 45–58.

Interaction of Light Waves in Active Nonlinear and Periodically Poled Nonlinear Crystals

G. D. Laptev[1, *], A. A. Novikov[2, **], and A. S. Chirkin[2, *]**

[1] *International Laser Center, Faculty of Physics, Moscow State University, Moscow, 119992 Russia*
**e-mail: gdl@hotbox.ru*
[2] *Faculty of Physics, Moscow State University, Vorob'evy gory, Moscow, 119992 Russia*
***e-mail: novikov@qopm.phys.msu.su*
****e-mail: chirkin@squeez.phys.msu.su*

Received June 4, 2003

The results of classical and quantum studies of the laser-radiation self-frequency conversion processes in periodically poled active nonlinear crystals are overviewed. The theoretical and experimental results of studying quasi-phase-matched self-frequency doubling and summation of the laser and pump frequencies in an active nonlinear periodically poled Nd:Mg:$LiNbO_3$ crystal are presented. The possibility of producing frequency- and polarization-entangled states and the sub-Poisson field statistics through a consecutive nonlinear optical frequency conversion in periodically poled nonlinear crystals is considered. © *2003 MAIK "Nauka/Interperiodica".*

PACS numbers: 42.65.Ky; 42.70.Mp; 42.50.-p

1. INTRODUCTION

Active nonlinear crystals combine active (lasing) properties, owing to the presence of rare-earth impurities (e.g., Nd^{3+}, Er^{3+}, Yb^{3+}), and nonlinear optical properties. In such crystals, the laser frequency can undergo self-frequency conversion if the lasing at a certain frequency is accompanied by the nonlinear conversion of the latter. Studies of active nonlinear crystals were begun back in 1960s [1, 2] and continue to the present day [3–6]. Nowadays, the following active nonlinear crystals are most frequently used in the self-frequency conversion experiments: Nd:$YAl_3(BO_3)_4$ [7–10], Nd:$YCa_4O(BO_3)_3$ [11], Nd:$CdCa_4O(BO_3)_3$ [12], and Yb:$YAl_3(BO_3)_4$ [13].

Recent achievements in selective (diode) laser-pumping technique [3, 6] and the appearance of new active nonlinear crystals with high nonlinearity, high concentration of rare-earth ions, and high optical damage threshold [14–17] have opened up new possibilities for designing compact laser radiation sources [18].

However, in spite of the appearance of new active nonlinear crystals with quadratic nonlinearity, the capabilities associated with increasing the number of nonlinear optical transformations and parametric effects have not been extended. The main reason is that the capabilities of homogeneous nonlinear and active nonlinear crystals are limited because of their dispersion properties. The use of nonlinear and active nonlinear crystals with a periodic inhomogeneity [18], in which the quasi-phase-matched light wave interaction can be implemented if the modulation period of nonlinear susceptibility is properly chosen, allows the range of practically realizable nonlinear optical processes to be substantially extended.

This has motivated our studies of laser-radiation self-frequency conversion processes in periodically poled active nonlinear crystals (PPANCs). A characteristic feature of a PPANC is that its polar axis periodically changes its direction, resulting in a periodic change in the sign of some of the nonlinear susceptibilities. The modulation of the nonlinear susceptibility and, correspondingly, modulation of the wave coupling on going from layer to layer produces a "nonlinear" lattice. As a result, a PPANC can be used to practically implement quasi-phase-matched frequency conversion, for which the detuning of interacting waves is compensated by the reciprocal nonlinear-lattice vector.

Our studies at the interface between laser physics and nonlinear optics have shown that the combination of the PPANC selective pumping and the wave quasi-phase-matching technique extends the class of three-wave interaction processes because of the inclusion of laser and pumping waves into the nonlinear processes.

Of great interest is the study of the quantum properties of the processes occurring in active nonlinear and periodically poled nonlinear crystals. Until now, parametric photon down-conversion, for which the frequency of a created photon is lower than the pump frequency, has been the main source of nonclassical light [19]. This traditional process can be implemented through both phase-matched and quasi-phase-matched wave interactions. In the interactions studied in this work, two nonlinear processes are coupled to each

other. These are either two nonlinear optical processes or the laser and the nonlinear optical processes. In the first case, one deals with the consecutive interactions, and in the second case, with the frequency self-frequency conversion. These situations are cardinally different from the well-known three-frequency process. For instance, in the consecutive processes, the frequencies of the created photons can be both higher and lower than the pump frequency, and there is a quantum correlation between them.

In this review, we report our results obtained over the past three years under the partial support of the Russian Foundation for Basic Research (project no. 00-02-16040). In Section 2, the results of classical theory of the intracavity three-wave interaction processes in a PPANC are presented. The following stationary generation regimes with self-frequency conversion are considered: laser self-frequency doubling and self-frequency halving, frequency summation with the pump wave, and the consecutive third harmonic generation and parametric amplification at low-frequency pumping. Section 3 reports the experimental data on quasi-phase- matched self-frequency conversion of the laser and pump frequencies. The PPANC grown technique is also briefly discussed. Section 4 is devoted to the quantum analysis of the processes of quasi-phase-matched laser-frequency conversion in PPANCs. In Section 5, it is shown that the frequency- and polarization-entangled photon states can be produced through the consecutive nonlinear optical frequency transformations in periodically poled nonlinear crystals. In Section 6, the parametric amplification at a low-frequency pumping is considered in the context of nonclassical light generation. The possibility of generating a radiation with sub-Poisson photon statistics is also demonstrated.

2. QUASI-PHASE-MATCHED LASER-FREQUENCY SELF-FREQUENCY CONVERSION IN PPANC

2.1. Three-Frequency Quasi-Phase-Matched Wave Interactions

Consider a PPANC placed inside a cavity formed by two plane mirrors applied to the crystal ends (Fig. 1). In the case of quasi-phase-matched frequency self-conversion, laser action in a crystal occurs, e.g., at frequency ω_1 and, simultaneously, the waves with frequencies ω_1, ω_2, and ω_3, such that $\omega_1 + \omega_2 = \omega_3$, are involved in the quasi-phase-matched nonlinear interaction. We assume that one of the cavity mirrors totally reflects the radiation at the frequencies of all interacting waves, while the intensity reflection coefficient of another (exit) mirror is R_j for the wave with frequency ω_j (j = 1, 2, 3).

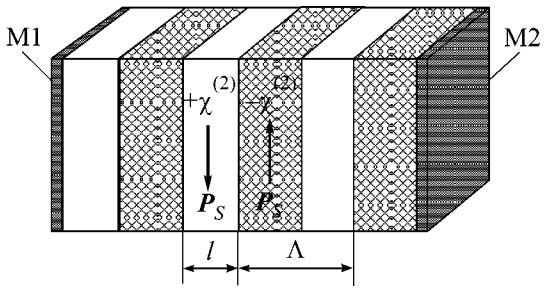

Fig. 1. Active nonlinear PP crystal inside a cavity. M1 and M2 are the cavity mirrors, Λ is the PP period, l is the domain length, $\mathbf{P}_S$ is the spontaneous polarization vector in the domain, and $\chi^{(2)}$ is the coefficient of quadratic nonlinear susceptibility.

The corresponding process of quasi-phase-matched frequency self-frequency conversion is described by the following set of equations [20]:

$$\frac{dI_{1,2}}{dt} = \frac{1}{n_{1,2}T_C}(-\nu_{1,2}I_{1,2} - \sqrt{\varepsilon_{1,2}I_1I_2I_3}\sin(\varphi + \theta)), \quad (1)$$

$$\frac{dI_3}{dt} = \frac{1}{n_3T_C}(-\nu_3I_3 + \sqrt{\varepsilon_3I_1I_2I_3}\sin(\varphi + \theta)), \quad (2)$$

$$\frac{d\varphi}{dt} = \frac{\sqrt{I_1I_2I_3}}{2(n_1 + n_2 - n_3)T_C}\left(\frac{\sqrt{\xi_2}}{I_2}\cos(\varphi + \psi_2) + \frac{\sqrt{\xi_1}}{I_1}\cos(\varphi + \psi_1) - \frac{\sqrt{\xi_3}}{I_3}\cos(\varphi + \psi_3) + \frac{2\delta\Psi}{\sqrt{I_1I_2I_3}}\right), \quad (3)$$

$$\frac{dI_q}{dt} = \frac{\nu_qI_q}{n_qT_C}(N - 1), \quad (4)$$

$$\frac{dN}{dt} = \frac{1}{T_\parallel}(1 + \eta - N(I_q + I_qR_q + 1)). \quad (5)$$

In Eqs. (1)–(5), I_j (j = 1, 2, 3) is the intensity of the ω_jth wave normalized to the saturation intensity I_S of the active medium; φ is the phase difference between the interacting waves; N is the inverse population normalized to its threshold value; index q corresponds to the frequency amplified due to the crystal active properties; $\nu_j = 2(1 - R_j)/(1 + R_j) + 2\alpha_jL$ are the dimensionless linear losses in the cavity for the ω_jth wave, where L is the crystal length and α_j are the linear losses in crystal; the parameter $\varepsilon_j = 8192F_j\pi^3L^2I_S(\mathbf{e}_j\chi^{(2)}_{jik}\mathbf{e}_i\mathbf{e}_k)^2/cn_1n_2n_3\lambda_j^2m^2$ is the nonlinear wave-coupling coefficient with allowance for the quasi-phase-matching $\Lambda = 2\pi m/\Delta k$, where

Λ is the modulation period of the quadratic nonlinear-susceptibility coefficient, m is the quasi-phase-matching order (an odd number), and $\Delta k = k_1 + k_2 - k_3$ is the wave mismatch; $\mathbf{e}_j$, $k_j = 2\pi/\lambda_j$, and n_j are the polarization unit vector, the wave number, and the crystal refractive index for the jth wave, respectively; $\chi^{(2)}_{jik}$ is the quadratic nonlinear- susceptibility tensor; the function

$$F_j = \frac{1 + R_1R_2R_3 + 2\sqrt{R_1R_2R_3}\cos(\Delta kL + \delta\Psi)}{(1 + R_j)^2}$$

is associated with the cavity mirrors; $\delta\Psi/2$ is the additional phase difference acquired by the waves upon their reflection from the cavity mirrors; $1 + \eta = \delta P_{\text{pump}}/P_{\text{th}}$ is the ratio of pump power absorbed in crystal to its threshold value, and δ is the pump absorption coefficient; T_C is the cavity passage time; $T_\parallel$ is the inverse-population relaxation time in the active medium; $\xi_j = \varepsilon_j A^2/4F_j$; $\theta = \arcsin(B/(F_j(1 + R_j)^2))$; and $\varphi_j = \arcsin(B/A)$, where

$$A = \sqrt{(1 + R_1R_2R_3/R_j^2 + 2\cos(\Delta kL + \delta\Psi)\sqrt{R_1R_2R_3/R_j^2}),}$$

and

$$B = (1 + \sqrt{R_1R_2R_3/R_j^2})\cos(\Delta kL/2 + \delta\Psi/2).$$

Set of equations (1)–(5) describes, in general form, the process of quasi-phase-matched laser-radiation self-frequency conversion in a PPANC. The right-hand side of Eq. (4) should be substituted for the term $\nu_j I_j/n_j T_C$ in Eq. (1) or (2), depending on which of the $\omega_{1,2}$ or ω_3 waves is amplified by the active medium.

The following quasi-phase-matched laser-frequency self-frequency conversion processes were studied in detail: frequency self-frequency doubling, self-frequency halving, and addition (mixing) involving the pump wave. These processes were studied for the periodically poled Nd:Mg:$LiNbO_3$ crystal, in which the most intense lasing occurs at a wavelength of 1.084 μm [21].

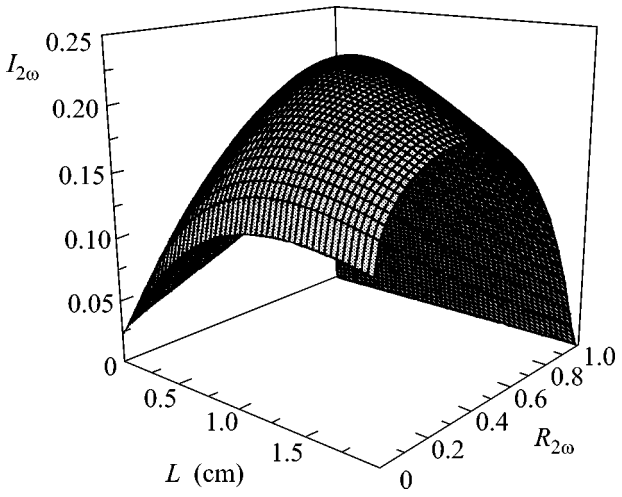

Fig. 2. Normalized second harmonic intensity ($I_{2\omega}$) at the exit from the cavity vs. the crystal length (L) and the reflection coefficient ($R_{2\omega}$) of the exit mirror for the second harmonic.

In the case of *quasi-phase-matched self-doubling*, laser generation in a periodically poled Nd:Mg:$LiNbO_3$ crystal (1.084 μm) is accompanied by the radiation in the green region (0.542 μm) because of the frequency doubling. For the process considered, $\omega_1 = \omega_2 = \omega$ and $\omega_3 = 2\omega$, and the system of Eqs. (1)–(5) has two steady-state solutions for the second harmonic intensity:

$$I_3 = \frac{\varepsilon_3}{4\nu_3^2}(-\nu_1\nu_3(\varepsilon_1\varepsilon_3)^{-1/2} - 1/2 + \sqrt{(\nu_1\nu_3(\varepsilon_1\varepsilon_3)^{-1/2} + 1/2)^2 + 2\eta\nu_1\nu_3(\varepsilon_1\varepsilon_3)^{-1/2}})^2, \quad (6)$$

$$I_3 = \frac{4\nu_1\eta\sqrt{R_3} - \nu_3(1 + R_3)}{4\sqrt{R_3}(4\nu_1\sqrt{R_3} + \nu_3(1 + R_3))}. \quad (7)$$

In deriving expressions (6) and (7), it was assumed that the cavity Q factor is high for the laser frequency ω ($R_1 = R_2 = 1$) and $\delta\Psi = 0$. Note that, for $\delta\Psi \neq 0$, the system of interest has no simple analytic solution. Depending on the values of parameters $\nu_{1,3}$, $\varepsilon_{1,3}$, R_3, and η, one obtains either of two steady-state solutions (6) or (7).

A typical behavior of intensity is shown in Fig. 2 for the stable branch of solutions (6) and (7). One can see from this figure that, for a certain optimal crystal length and a certain reflection coefficient $R_{2\omega}$ of the exit mirror, the second harmonic output intensity (power) is maximal. The calculations were carried out for a periodically poled Nd:Mg:$LiNbO_3$ crystal with a length of 0.5 cm, a nonlinearity period $\Lambda = 7$ μm, and the quasi-phase-matching order $m = 1$. The *ee–e* interaction was used, for which lithium niobate crystal has the greatest nonlinear coefficient $d_{33} = 34.4$ pm/V. The other parameters used in the calculations were as follows: $I_S = 10$ kW/m^2 (data from [20]), $P_{\text{pump}} = 2$ W, $P_{\text{th}} = 1.25\nu_1$, $\delta = 0.5$, $\alpha_\omega = 0.08$ cm^{-1}, $\alpha_{2\omega} = 0.1$ cm^{-1}, and the beam radius in the cavity was 100 μm. It was assumed that the pump power absorbed in the crystal obeyed the expression $\delta P_{\text{pump}} = P_{\text{pump}}(1 - \exp(-\tau L))$, where τ is the pump

linear absorption coefficient. The value $\tau = 2\ln 2$ cm^{-1} was taken.

In the case of *quasi-phase-matched self-halving*, the laser generation in a periodically poled Nd:Mg:$LiNbO_3$ crystal (at 1.084 μm) is accompanied by the second subharmonic generation (at 2.168 μm) as a result of frequency half-division. The resulting two-micron radiation is harmless to human eyes and, hence, it may be of interest in a number of applications. For the frequency self-halving, the set of Eqs. (1)–(5) also has an analytic solution in the case of stationary generation. The behavior of intensity corresponding to this regime is shown in Fig. 3. It follows from this figure that the process has a threshold character and that the subharmonic generation is possible only in a high-Q cavity. The curves in Fig. 3 were calculated for an Nd:Mg:$LiNbO_3$ crystal with the domain structure period $\Lambda = 22$ μm ($m = 1$), $P_{pump} = 3$ W, and $\alpha_{\omega/2} = 0.08$ cm^{-1}. The other parameters were the same as in the case of frequency self-doubling.

In the case of *quasi-phase-matched self-frequency summing* in Nd:Mg:$LiNbO_3$, the pump radiation (0.81 μm) that is not absorbed in crystal interacts nonlinearly with the laser frequency (1.084 μm) to create a wave with the sum frequency (0.464 μm). The corresponding wavelength for the crystal under study lies in the violet region. For this process, the set of Eqs. (1)–(5) also has an analytic solution. The stable branch of this solution is shown in Fig. 4. The calculations were carried out for the Nd:Mg:$LiNbO_3$ crystal with the nonlinearity modulation period $\Lambda = 4.2$ μm ($m = 1$), $P_{pump} = 2$ W, $\alpha_3 = 0.1$ cm^{-1} and $R_2 = 0$. The other parameters were as in the cases considered above.

2.2. Frequency Self-Conversion in Consecutive Wave Interactions

Apart from the traditional nonlinear optical interactions considered above, periodically poled crystals allow the sequential [22] and simultaneous [23] three-wave interactions. The use of PPANCs opens new possibilities of simultaneous generation at several frequencies in the same crystal.

Let, as above, the PPANC be situated inside the cavity (Fig. 1). Let the laser radiation in a crystal be generated at the frequency ω_1, and the conditions for quasi-phase-matched consecutive interaction of four waves ω_1, ω_2, ω_3, and ω_4, such that $\omega_1 + \omega_2 = \omega_3$ and $\omega_1 + \omega_3 = \omega_4$, be fulfilled. We assume that one of the cavity mirrors totally reflects all interacting waves, while the intensity reflection coefficients of another mirror are R_j ($j = 1, 2, 3, 4$).

In this case, the wave interaction obeys the following set of equations [24]:

$$\frac{dI_1}{dt} = \frac{1}{n_1 T_C}(-\nu_1 I_1 - \sqrt{\varepsilon_{21} I_1 I_2 I_3}\cos\Psi_2), \qquad (8)$$

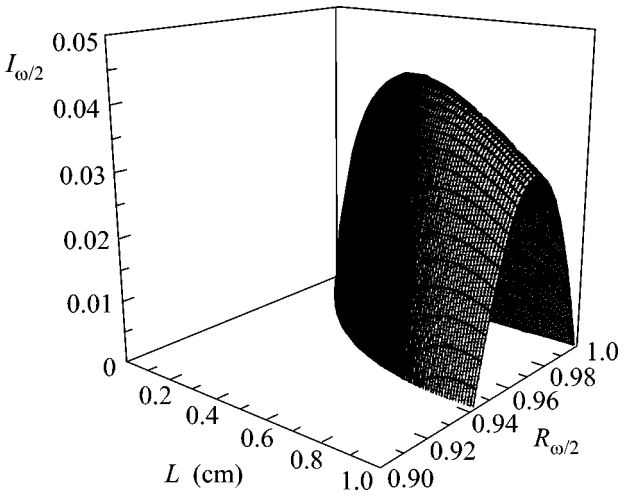

Fig. 3. Normalized subharmonic intensity ($I_{\omega/2}$) at the exit from the cavity vs. the crystal length (L) and the reflection coefficient ($R_{\omega/2}$) of the exit mirror for the subharmonic.

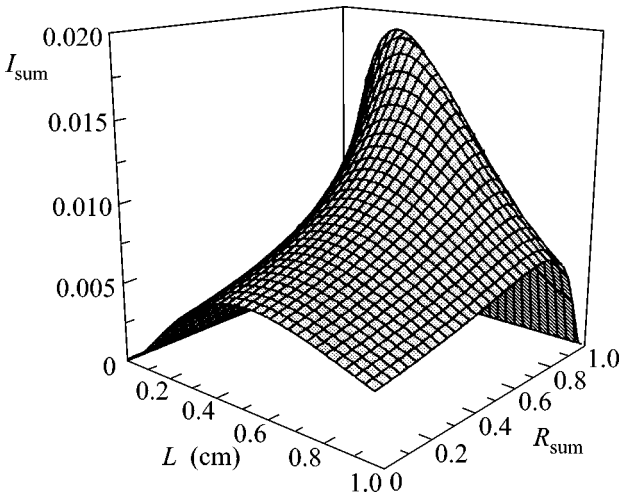

Fig. 4. Normalized intensity (I_{sum}) of sum frequency at the exit from the cavity vs. the crystal length (L) and the reflection coefficient (R_{sum}) of the exit mirror for the sum frequency.

$$\frac{dI_2}{dt} = \frac{1}{n_2 T_C} \times (-\nu_2 I_2 - \sqrt{\varepsilon_{32} I_2 I_3 I_4}\cos\Psi_3 - \sqrt{\varepsilon_{22} I_1 I_2 I_3}\cos\Psi_2), \qquad (9)$$

$$\frac{dI_3}{dt} = \frac{1}{n_3 T_C} \times (-\nu_3 I_3 - \sqrt{\varepsilon_{33} I_2 I_3 I_4}\cos\Psi_3 + \sqrt{\varepsilon_{23} I_1 I_2 I_3}\cos\Psi_2), \qquad (10)$$

$$\frac{dI_4}{dt} = \frac{1}{n_4 T_C}(-\nu_4 I_4 + \sqrt{\varepsilon_{34} I_2 I_3 I_4}\cos\Psi_3), \qquad (11)$$

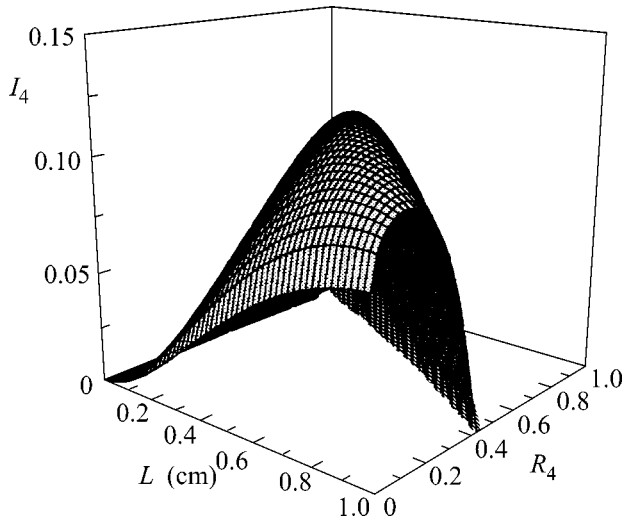

Fig. 5. Normalized intensity (I_4) of the wave with frequency ω_4 at the exit from the cavity vs. the crystal length (L) and the reflection coefficient (R_4) of the exit mirror for the wave with frequency ω_4.

$$\frac{d\Psi_2}{dt} = \frac{\sqrt{I_2 I_3 I_4}\sin\Psi_3}{4(n_1+n_2-n_3)T_C}\left(\frac{\sqrt{\xi_{33}}}{I_3}-\frac{\sqrt{\xi_{32}}}{I_2}\right) + \frac{\sqrt{I_1 I_2 I_3}\sin\Psi_2}{4(n_1+n_2-n_3)T_C}\left(\frac{\sqrt{\xi_{23}}}{I_3}-\frac{\sqrt{\xi_{22}}}{I_2}-\frac{\sqrt{\xi_{21}}}{I_1}\right), \quad (12)$$

$$\frac{d\Psi_3}{dt} = \frac{\sqrt{I_2 I_3 I_4}\sin\Psi_3}{4(n_2+n_3-n_4)T_C}\left(\frac{\sqrt{\xi_{34}}}{I_4}-\frac{\sqrt{\xi_{33}}}{I_3}-\frac{\sqrt{\xi_{32}}}{I_2}\right) - \frac{\sqrt{I_1 I_2 I_3}\sin\Psi_2}{4(n_1+n_2-n_3)T_C}\left(\frac{\sqrt{\xi_{23}}}{I_3}+\frac{\sqrt{\xi_{22}}}{I_2}\right), \quad (13)$$

$$\frac{dI_q}{dt} = \frac{\nu_q I_q}{n_q T_C}(N-1), \quad (14)$$

$$\frac{dN}{dt} = \frac{1}{T_\parallel}(1+\eta-N(I_q+I_q R_q+1)), \quad (15)$$

where $\Psi_{2,3}$, ε_{2i}, ε_{3p}, ξ_{2i}, and ξ_{3p} are, respectively, the phase differences and the nonlinear wave-coupling coefficients (i = 1, 2, 3, p = 2, 3, 4).

The calculations carried out with the dispersion data taken for the periodically poled Nd:Mg:$LiNbO_3$ crystal from [25] showed that, for the properly chosen modulation period of nonlinear susceptibility and quasi-phase-matching orders, the following sequential quasi-phase-matched processes can occur in this crystal. (i) Parametric amplification at low-frequency pumping: $\omega_3 \longrightarrow \omega_1 + \omega_2$ and $\omega_2 + \omega_3 \longrightarrow \omega_4$, if the wave ω_3 is amplified due to the active crystal properties and the frequency $\omega_4 > \omega_3$ is generated as a result of frequency summation, and (ii) third harmonic generation $\omega + \omega \longrightarrow 2\omega$ and $\omega + 2\omega \longrightarrow 3\omega$, if the wave with frequency ω is amplified in the crystal. It should be noted that, in contrast to the conventional nonlinear periodically-poled crystals, one fails to realize the sequential quasi-phase-matched interactions for multiple frequencies, i.e., the situation for which $\omega_1 = \omega_2 = \omega$, $\omega_3 = 2\omega$, and $\omega_4 = 3\omega$, in the active nonlinear crystals [22].

Let us now turn to *the quasi-phase-matched parametric amplification at low-frequency pumping.* In the Nd:Mg:$LiNbO_3$ crystal, this process proceeds as follows: 1.084 μm $\longrightarrow$ 2.163 μm + 2.173 μm and 2.173 μm + 1.084 μm $\longrightarrow$ 0.728 μm. To observe this process in the first quasi-phase-matching order for the *ee–e* interactions, the RDS period should be Λ = 20.7 μm. The behavior of intensity corresponding to the steady-state solution to the set of Eqs. (8)–(15) is presented in Fig. 5. The calculations were performed with $P_{\text{pump}} = 3$ W, $\nu_1 = \nu_2 = \nu_3 = 0.08$, and $\alpha_4 = 0.1$ cm^{-1}. The other parameters were the same as in the previous cases.

In this crystal, the *quasi-phase-matched consecutive third harmonic generation* in the low quasi-phase-matching orders can be realized with a laser wavelength of 1.387 μm. The corresponding period must be Λ = 13 μm. This process proceeds in the following way: 1.387 μm $\longrightarrow$ 0.6935 μm + 0.6935 μm and 1.387 μm + 0.6935 μm $\longrightarrow$ 0.462 μm. The third harmonic frequency falls within the violet wavelength range.

EXPERIMENTS ON QUASI-PHASE-MATCHED LASER-FREQUENCY SELF-FREQUENCY CONVERSION

3.1. Periodically Polled Active Nonlinear Nd:Mg:$LiNbO_3$ Crystals

There are several methods of forming regular domain structure in active nonlinear crystals. Among them are the standard growth (Czochralski) method, the method of post-growth crystal processing through applying a high voltage (so-called high-voltage method), and the diffusional method. At present, quasi-phase-matched frequency self-frequency conversion has been experimentally observed in the crystals that were prepared by all the indicated methods [26–31]. The best results were obtained for the active nonlinear RDS crystals grown by the Czochralski method [18].

The Czochralski method allows the preparation, directly in the course of growth, of RDS crystals containing relatively smooth and flat domain walls with a broad range of periods and a crystal volume of several cm^3 [32, 33]. If the symmetry axis of the heat field does not coincide with the crystal rotation axis, the temperature periodically changes at the growth front, resulting in the modulation of the crystal chemical composition. The composition inhomogeneity gives rise to so-called growth rotational bands. On cooling with passing through the Curie point, a local field produced by the concentration gradient of rare-earth impurities Nd, Er, or Yb leads to the formation of a domain structure. The

spontaneous polarization vectors in the adjacent domains form an angle of 180° with each other. The maxima and minima of impurity concentration correspond to the domain walls, while the impurity modulation period corresponds to the period of domain structure [34, 35]. Therefore, rare-earth ions in PPANCs serve the functions of an active ion and of a "building material" in the formation of a regular domain structure. The presence of MgO in a periodically poled crystal diminishes the photorefractive damage of a PPANC, thereby improving its quality. The PPANC period is determined by the ratio of pulling rate to the crystal rotation velocity during the growth.

3.2. Frequency Self-Doubling in the Nd:Mg:LiNbO$_3$ Periodically Poled Crystal

To observe frequency self-frequency doubling [18], a Nd:Mg:LiNbO$_3$ crystal with a regular domain structure and a composition close to its congruent ratio ([Li]/[Nb] = 0.942) was grown by the Czochralski method from a melt along the normal to the close-packed face $(01\bar{1}2)$. For the experiments, a sample with a length of 7 mm and a period of domain structure of about 7 μm was cut from the grown crystal. After bleaching, the sample was placed into a 20-centimeter hemispherical cavity near the flat mirror with a high reflectivity (99.9%) at the laser wavelength (1.084 μm) and a high transmittance (85%) at a diode pumping wavelength (Fig. 6). The exit mirror of the cavity was a spherical mirror with a high reflectivity at the laser wavelength and a high transmittance (80%) at the second harmonic wavelength (0.542 μm). The sample was pumped by a diode laser (0.81 μm). The radiation at the laser generation frequency was linearly polarized and corresponded to the π polarization ($^4F_{3/2} \longrightarrow {}^4I_{11/2}$ laser transition). The second harmonic and the pump polarizations coincided with the laser polarization. According to our calculations, the effective nonlinear coefficient for the *ee–e* interaction in lithium niobate was 12 pm/V under the conditions of our experiment. The laser radiation power and the second harmonic power as functions of the pump power absorbed in the crystal are shown in Fig. 7. The solid line in Fig. 7 is the theoretical dependence corresponding to the steady-state solution to the set of Eqs. (1)–(5) for self-frequency doubling with the parameters used in the experiment. The best agreement between the experimental and theoretical data was obtained for an effective nonlinear coefficient of 5 pm/V.

3.3. Frequency Summation in the Nd:Mg:LiNbO$_3$ Periodically Poled Crystal

For the experiment with frequency summation [36], the Nd:Mg:LiNbO$_3$ periodically poled crystal was grown by the Czochralski method. The prepared nonlinear sample was 6 mm in length and had a domain

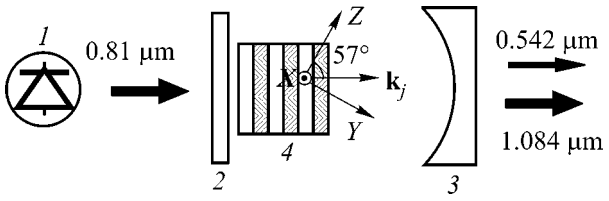

Fig. 6. Schematic of the experimental setup: (*1*) diode laser; (*2*) and (*3*) are the flat and (exit) spherical cavity mirror, respectively; and (*4*) is the active nonlinear Nd:Mg:LiNbO$_3$ periodically poled crystal.

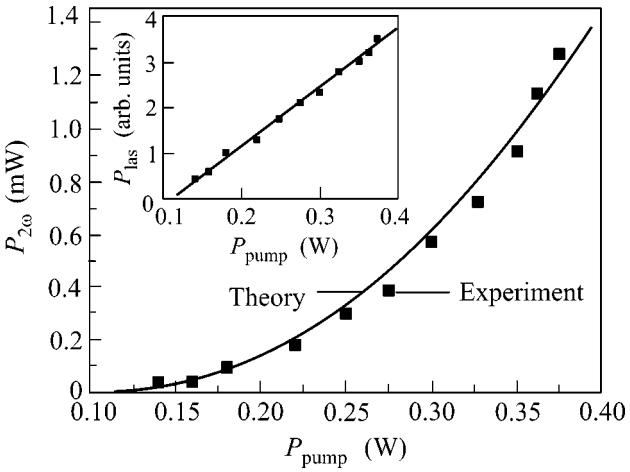

Fig. 7. Laser radiation power P_{las} and the second harmonic power $P_{2\omega}$ as functions of the pump power P_{pump} absorbed in the crystal.

period of about 4 μm. The experimental scheme was analogous to the scheme of frequency self-frequency doubling, with the only difference that the exit mirror had a transmittance of about 90% for the sum wave. The nonabsorbed portion of pump radiation was involved in the nonlinear interaction with the pump and laser frequencies. This gave rise to the wave with the sum frequency; its length was measured by a monochromator and found to be 0.464 μm, in accordance with the calculated value. The laser, pump, and sum radiations were linearly polarized and corresponded to the π polarization. The laser radiation power and the sum-wave power as functions of the pump power absorbed in the crystal are shown in Fig. 8. The solid line in this figure is the theoretical dependence corresponding to the steady-state solution to the set of Eqs. (1)–(5) for this process with the parameters used in the experiment. As in the case of self-frequency doubling, the best agreement between the experimental and theoretical data was achieved for an effective nonlinear coefficient of 5 pm/V.

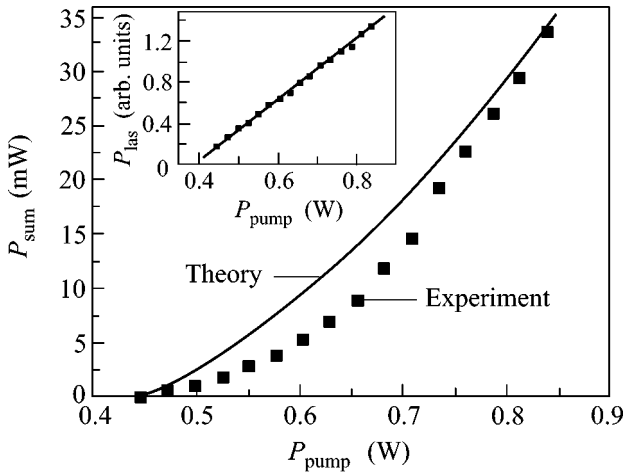

Fig. 8. Laser radiation power P_{las} and the sum-frequency power P_{sum} as functions of the pump power P_{pump} absorbed in the crystal.

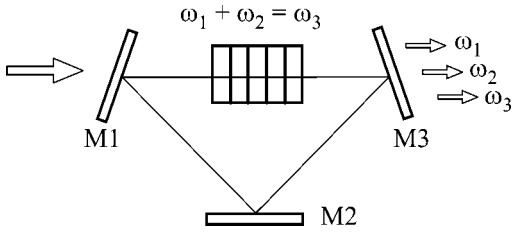

Fig. 9. Schematic of the active nonlinear periodically poled crystal inside a ring cavity.

4. QUANTUM THEORY OF LASER-FREQUENCY SELF-FREQUENCY CONVERSION

Let us now turn to the three-frequency interactions, in which the wave ω_1 is amplified due to the crystal active properties and the waves with frequencies ω_1, ω_2, and ω_3 are involved in the quasi-phase-matched interaction ($\omega_1 + \omega_2 = \omega_3$). For a ring cavity with a PPANC inside (Fig. 9), we derived the following set of Heisenberg–Langevin equations for the evolution of the field and atomic operators [37]:

$$\frac{da_{1,2}}{dt} = -\frac{\nu_{1,2}}{2}a_{1,2} + i\varepsilon a_{2,1}^{+}a_3 + F_{1,2}(t), \quad (16)$$

$$\frac{da_3}{dt} = -\frac{\nu_3}{2}a_3 + i\varepsilon a_1 a_2 + F_3(t), \quad (17)$$

$$\frac{d\sigma}{dt} = \frac{2T_C}{T_\perp}(-\sigma + igT_\perp a_q N) + \Gamma(t), \quad (18)$$

$$\frac{d\sigma^{+}}{dt} = \frac{2T_C}{T_\perp}(-\sigma^{+} - igT_\perp a_q^{+} N) + \Gamma^{+}(t), \quad (19)$$

$$\frac{dN}{dt} = \frac{2T_C}{T_\parallel}(P - N + i2T_\parallel g(\sigma a_q^{+} - \sigma^{+} a_q)) + \Gamma_N(t). \quad (20)$$

In this set of equations, a_j^{+} and a_j are the photon creation and annihilation operators satisfying the commutation rules $[a_j(t), a_k^{+}(t)] = \delta_{jk}$ (δ_{jk} is Kronecker delta); ε is the nonlinear wave-coupling coefficient; $\sigma = \sum_{\nu=1}^{M}\sigma_\nu$ and $N = \sum_{\nu=1}^{M}N_\nu$ are, respectively, the polarization operator and the operator of inverse population of the whole active medium, where σ_ν and N_ν are, respectively, the polarization and inverse population of the νth active atom and M is the total number of active atoms in the crystal; t is the dimensionless time normalized to $2T_C$; $\nu_j = 1 - R_j + \alpha_j L$ are the linear losses in the crystal and at the cavity mirrors for the wave with frequency ω_j; $g = \sqrt{c\hbar\omega_q/4I_S V T_\parallel T_\perp}$ is the interaction constant of an atom and electromagnetic field; $T_\parallel$ and $T_\perp$ are, respectively, the inverse-population and polarization relaxation times; V is the quantization volume; $P = k_q(1+\eta)/2g^2T_C T_\perp$ is the pump parameter; and $\Gamma(t)$ and $\Gamma_N(t)$ are the noise operators associated, respectively, with the polarization and inverse population of the active medium. The appearance of these operators and the terms $(2T_C/T_\perp)\sigma$, $(2T_C/T_\perp)\sigma^{+}$, and $2T_C(P-N)/T_\parallel$ appearing in the set of Eqs. (16)–(20) is caused by the interaction of the electromagnetic field with the thermal bath.

The set of Eqs. (16)–(20) was solved by the standard method. The operators were represented as the sums of stationary values (classical quantities) and fluctuation operators. This approach was used to obtain analytic expressions for the spectra of fluctuation operators at the exit from cavity and to analyze the possibility of nonclassical light generation [37]. The analysis was carried out for the quadrature field components

$$X_j = a_j + a_j^{+}, \quad Y_j = i(a_j^{+} - a_j). \quad (21)$$

The fluctuation spectra of one of the quadrature field components at the frequency of the second harmonic obtained in the course of self-frequency doubling is shown in Fig. 10. The unit level in Fig. 10 corresponds to the standard quantum level, i.e., to the vacuum fluctuation level. One can see in Fig. 10 that, by properly choosing the converter parameters, one can sizably enhance the efficiency of fluctuation suppression for the quadrature component considered. With the parameters used, the maximal suppression efficiency is approximately 70%. In accordance with the uncertainty principle, the fluctuations of the conjugate quadrature component (Y component) prove to be higher than the standard quantum level. In this section, all calculations are performed with the same parameters as those used in Section 2 in the classical analysis of the frequency self-frequency conversion processes. The remaining

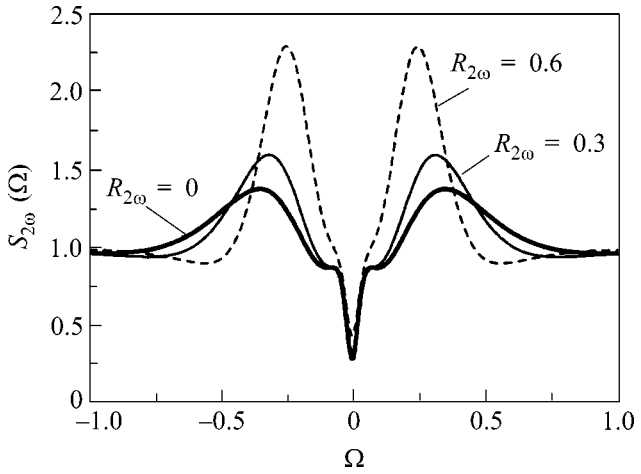

Fig. 10. Fluctuation spectrum $S_{2\omega}(\Omega)$ of the second harmonic field X quadrature for various reflection coefficients $R_{2\omega}$ of the exit mirror; $\Omega = 2T_C\omega$. The curves are constructed for the pump power $P_{pump}/P_{th} = 20$.

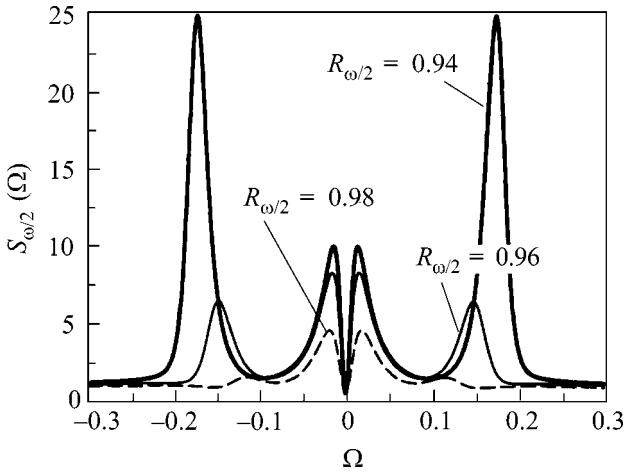

Fig. 11. Fluctuation spectrum $S_{\omega/2}(\Omega)$of the subharmonic field X quadrature for various reflection coefficients $R_{\omega/2}$ of the exit mirror; $\Omega = 2T_C\omega$. The curves are constructed for the pump power $P_{pump}/P_{th} = 20$.

parameters are $T_\perp = 6.7 \times 10^{-10}$ s, $T_C = 3 \times 10^{-11}$ s, and $M = 10^{18}$.

In the quantum study of frequency self-frequency halving, one should take into account that this process, apart from the lasing threshold, is characterized by the subharmonic-generation threshold. For this reason, two regimes can be considered: (i) the above-threshold and (ii) the subthreshold subharmonic-generation regimes. The fluctuation spectra for one of the quadrature subharmonic components for these regimes are presented, respectively, in Figs. 11 and 12. One can see in these figures that the maximal fluctuation-suppression efficiency for the converter parameters used is about 50% for the above-threshold regime and about 90% for the subthreshold regime. Thus, by properly choosing the crystal, pumping, and cavity parameter, one can appreciably enhance the efficiency of fluctuation suppression in the process considered.

It should be noted that the processes of simultaneous laser generation and nonlinear laser-frequency conversion in a cavity were studied earlier for gas lasers [38, 39]. In gas lasers, the photon lifetime in a cavity is much longer than the inverse-population and polarization relaxation times in the active medium, allowing the analysis of nonlinear equations to be greatly simplified. Moreover, the results obtained in [36, 37] cannot be applied to solid-state lasers.

5. THE FORMATION OF ENTANGLED STATES IN SIMULTANEOUS QUASI-PHASE-MATCHED PARAMETRIC CONVERSION PROCESSES

The quasi-phase-matched interactions can be used to produce entangled quantum states in the collinear wave-interaction geometry [38, 39]. We will focus on the process of parametric generation of frequencies ω_1 and ω_2 in the pump field of frequency ω_3, such that $\omega_3 = \omega_1 + \omega_2$. Let us consider two methods of frequency down-conversion in a periodically poled crystal: (i) the wave with frequency ω_1 is ordinary (index o) and the wave with frequency ω_2 is extraordinary (index e), and (ii) the wave with frequency ω_1 is extraordinary and the wave with frequency ω_2 is ordinary. In these cases, the condition for simultaneous quasi-phase-matching is written as

$$\Delta k^{(1)} = k_3 - k_1^{(o)} - k_2^{(e)} = 2\pi m_1/\Lambda, \quad (22)$$

$$\Delta k^{(2)} = k_3 - k_1^{(e)} - k_2^{(o)} = 2\pi m_2/\Lambda, \quad (23)$$

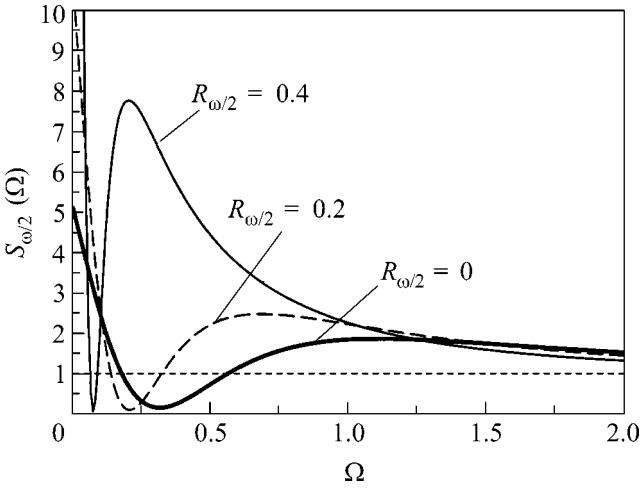

Fig. 12. Fluctuation spectrum $S_{\omega/2}(\Omega)$ of the subharmonic field X quadrature for various reflection coefficients $R_{\omega/2}$ of the exit mirror; $\Omega = 2T_C\omega$. The pump power $P_{pump}/P_{th} = 8$.

where m_1 and m_2 are the quasi-phase-matching orders. Our analysis showed that quasi-phase-matching conditions (22) and (23) can be met in the $LiNbO_3$ crystal. The corresponding nonlinear wave-coupling coefficients are nonzero if the pump wave is ordinary (the processes are due to the nonlinear susceptibility d_{15}).

In the approximation of a given classical pump field, these processes are described by the interaction Hamiltonian [40, 41]

$$H_I^{(s)} = \hbar[\beta_1 a_1^{(o)} a_2^{(e)} + \beta_2 a_1^{(e)} a_2^{(o)} + \text{h.c.}], \quad (24)$$

where h.c. stands for Hermitian conjugation, $\beta_j = \gamma_j A_3$, γ_j is the nonlinear coefficient, and A_3 is the pump amplitude.

In the Schrödinger representation, the evolution of the state vector of a two-frequency field obeys the well-known relation

$$|\psi(z)\rangle = \exp[-(i/\hbar)H_I^{(s)}z]|\psi(0)\rangle, \quad (25)$$

where $|\psi(0)\rangle$ is the vector of initial state.

For the vacuum initial states of the fields with frequencies ω_1 and ω_2, one has

$$|\psi(0)\rangle = |0\rangle_1|0\rangle_2.$$

Then, by inserting Eq. (24) into Eq. (25), one obtains the following expression for the field state at the nonlinear crystal output in the first order in coefficients β_1 and β_2 [40]:

$$\begin{aligned}|\psi(z)\rangle &= |0\rangle_1^{(o)}|0\rangle_1^{(e)}|0\rangle_2^{(o)}|0\rangle_2^{(e)} \\ &- i\beta_1 z|1\rangle_1^{(o)}|0\rangle_1^{(e)}|0\rangle_2^{(o)}|1\rangle_2^{(e)} \\ &- i\beta_2 z|0\rangle_1^{(o)}|1\rangle_1^{(e)}|1\rangle_2^{(o)}|0\rangle_2^{(e)},\end{aligned} \quad (26)$$

where the indices (o) and (e) denote the photon polarization state.

The state vector associated with the measured photons takes the form

$$|\psi(z)\rangle = \frac{1}{\sqrt{|\beta_1|^2 + |\beta_2|^2}}[\beta_1|H\rangle_1|V\rangle_2 + \beta_2|V\rangle_1|H\rangle_2], \quad (27)$$

where $|H\rangle_j = |1\rangle_j^{(o)}$ and $|V\rangle_j = |1\rangle_j^{(e)}$.

Therefore, according to Eq. (27), photons with frequencies ω_1 and ω_2 generated in these processes are in the polarization-entangled state. From state (27) one can obtain two Bell's states by changing the sign of the β_2/β_1 ratio. This ratio determines the degree of entanglement, because it depends on the ratio γ_2/γ_1 of nonlinear coefficients and the ratio m_1/m_2 of quasi-phase-matching orders. In our opinion, this way of producing entangled quantum states can be simply realized, because it uses only one periodically poled crystal and the collinear geometry of interacting waves. In the experiments [41], two nonlinear crystals were used for producing polarization-entangled states.

6. NONCLASSICAL LIGHT GENERATION UPON PARAMETRIC AMPLIFICATION IN A LOW-FREQUENCY PUMP FIELD

The sequential quasi-phase-matched interactions of light waves in nonlinear and active nonlinear periodically poled crystals open up new possibilities in nonclassical light generation. In recent years, we have developed a quantum theory of the sequential interactions between light waves with multiple frequencies [40, 42–46]. The quantum properties of waves with frequencies ω and 3ω in a given classical pump field with frequency 2ω were studied in detail.

The process of interest is described by the interaction Hamiltonian of the form [42]

$$H_I^{(c)} = \hbar[\beta_2 a_1^{+2} + \beta_2^* a_1^2 + \beta_3 a_3^+ a_1 + \beta_2^* a_3 a_1^+]. \quad (28)$$

Here, $\beta_j = \gamma_j A_2$, γ_j is the nonlinear coefficient, and A_2 is the pump amplitude.

In the Heisenberg representation, the following set of operator equations corresponds to this process:

$$\frac{da_1}{dz} = -i\beta_3^* a_3 - i2\beta_2 a_1^+, \quad (29)$$

$$\frac{da_3}{dz} = -i\beta_3 a_1. \quad (30)$$

The solution to Eqs. (29) and (30) can be represented as [45]

$$\begin{aligned}a_1(z) &= -e^{-i\varphi}G_+(z)a_{30} + e^{2i\varphi}G_-(z)a_{30}^+ \\ &+ u_+(z)a_{10} - ie^{i\varphi}F_+(z)a_{10}^+,\end{aligned} \quad (31)$$

$$\begin{aligned}a_3(z) &= u_-(z)a_{30} - ie^{3i\varphi}F_-(z)a_{30}^+ \\ &- ie^{i\varphi}G_+(z)a_{10} - e^{2i\varphi}G_-(z)a_{10}^+.\end{aligned} \quad (32)$$

The operators a_{j0} and a_{j0}^+ are related to the entrance of the periodically poled crystal, and the phase π is related to the pump phase.

For $|\beta_3| > |\beta_2|$, the functions in Eqs. (31) and (32) are given by the expressions

$$\begin{aligned}u_\pm(z) &= \cosh(|\beta_2|z)\cos(\gamma z) \\ &\pm \kappa\varepsilon\sinh(|\beta_2|z)\sin(\gamma z),\end{aligned} \quad (33)$$

$$\begin{aligned}F_\pm(z) &= \pm\sinh(|\beta_2|z)\cos(\gamma z) \\ &+ \kappa\varepsilon\cosh(|\beta_2|z)\sin(\gamma z),\end{aligned} \quad (34)$$

$$G_\pm(z) = 0.5\kappa[e^{(|\beta_2|z)} \pm e^{-(|\beta_2|z)}]\sin(\gamma z), \quad (35)$$

where $\kappa = 1/\sqrt{1-\varepsilon^2}$, $\gamma = \sqrt{|\beta_3|^2 - |\beta_2|^2}$, and $\varepsilon = |\beta_2/\beta_3|$.

For the case $|\beta_3| < |\beta_2|$, the corresponding functions are given in [43]. The interaction Hamiltonian (28) and solutions (31) and (32) can be used to calculate the sta-

tistical characteristics of radiation with frequencies ω and 3ω.

We first consider the formation of *frequency-entangled* states. In the Schrödinger representation, one has for the state of a two-frequency field at the crystal output

$$|\psi(z)\rangle = \exp[-(i/\hbar)H_I^{(c)}z]|\psi(0)\rangle. \quad (36)$$

Here, $|\psi(0)\rangle$ is the initial state vector in the absence of a signal at the entrance of the crystal; it can be written as

$$|\psi(0)\rangle = |0\rangle_1|0\rangle_3, \quad (37)$$

where $|0\rangle_j$ is the vacuum field state for the frequency $j\omega$.

In the second order in nonlinear coefficients $|\beta_2|$ and $|\beta_3|$, the field state at the crystal output can be written in the following compact form:

$$|\psi(z)\rangle = \mathcal{N}_1|\varphi\rangle_1|0\rangle_3 - q|1\rangle_1|1\rangle_3, \quad (38)$$

$$|\varphi\rangle_1 = \mathcal{N}_2|0\rangle_1 - if|2\rangle_1 - p|4\rangle_1. \quad (39)$$

Here, $\mathcal{N}_1$ and $\mathcal{N}_2$ are the normalization factors:

$$\mathcal{N}_1 = \sqrt{1-q^2}, \quad \mathcal{N}_2 = \sqrt{1-f^2+p^2}, \quad (40)$$

with

$$f = \sqrt{2}|\beta_2|z, \quad p = \sqrt{6}(|\beta_2|z)^2, \quad q = |\beta_2\beta_3|z^2$$

and the figures inside the ket-vectors stand for the number of photons.

From the analysis of Eqs. (38) and (39), it follows that only two ω photons appear in the first approximation. In the second approximation, either four ω photons or one photon with frequency ω and one photon with frequency 3ω are generated. From these expressions, it also follows that the photons with generated frequencies are in the entangled state. One photon with frequency 3ω is detected if and only if one ω photon is detected. The degree of entanglement of these states is [40, 42]

$$\begin{aligned}\varepsilon(|\psi\rangle) &= -\mathrm{Tr}_3(\rho_3\log_2\rho_3)\\ &= -(1-q^2)\log_2(1-q^2) - q^2\log_2 q^2.\end{aligned} \quad (41)$$

Note that it depends on the product of coefficients $|\beta_2|$ and $|\beta_3|$. It should be taken into account that expression (41) only applies if $q < 1$.

The analysis of fields at frequencies ω and 3ω showed [42] that, for the vacuum initial states, the radiation with these frequencies proved to be in the quadrature-squeezed state, and photons obeyed the super-Poisson statistics, as in the case of the usual parametric process in a high-frequency pump field. On the other hand, if a coherent signal at frequency ω or 3ω is fed to the entrance of a nonlinear crystal, *fields with sub-Poisson photon statistics can be generated* [45].

The photon statistics can conveniently be analyzed using solutions (31) and (32). Let us consider the behavior of a mean number of photons $\langle n_1(z)\rangle$ and $\langle n_3(z)\rangle$ at frequencies ω and 3ω, respectively, and the Fano factors $\mathcal{F}_1$ and $\mathcal{F}_3$ defined as

$$\langle n_j(z)\rangle = \langle\psi(0)|a_j^+(z)a_j(z)|\psi(0)\rangle, \quad (42)$$

$$\mathcal{F}_j = \frac{\langle\Delta n_j^2\rangle}{\langle n_j\rangle} \quad (j = 1, 3). \quad (43)$$

The phase sensitivity of this process in the case when the initial signal at one of the frequencies is coherent can clearly be seen from the expressions for the mean number of photons. Let the initial field with frequency ω be in the coherent state $|\alpha\rangle_1$ and the field at frequency 3ω be in the vacuum state $|0\rangle_3$; i.e., the state of the input field is $|\psi(0)\rangle = |\alpha\rangle_1|0\rangle_3$, where $\alpha = |\alpha|e^{i\varphi_{10}}$, $|\alpha| = \sqrt{\langle n_{10}\rangle}$, $\langle n_{10}\rangle$ is the mean number of photons, and φ_{10} is the phase of the signal wave. In this case, the mean numbers of photons at the crystal output are given by the expressions

$$\begin{aligned}\langle n_1(z)\rangle &= \langle n_{10}\rangle(u_+^2 + F_+^2\\ &+ 2u_+F_+\sin(\varphi - 2\varphi_{10})) + G_-^2 + F_+^2,\end{aligned} \quad (44)$$

$$\begin{aligned}\langle n_3(z)\rangle &= \langle n_{10}\rangle(G_+^2 + G_-^2\\ &+ 2G_+G_-\sin(\varphi - 2\varphi_{10})) + G_-^2 + F_-^2.\end{aligned} \quad (45)$$

The dependence of the mean number of photons on the phase difference between the pump φ and signal φ_{10} waves is clearly seen. Analysis showed that the sub-Poisson photon statistics can be obtained for the phase relationship $\Phi = \varphi - 2\varphi_{10} = -\pi/2$.

The dependence of the mean numbers of photons at frequencies ω and 3ω on the interaction length is shown in Fig. 13a for $\Phi = -\pi/2$. For the signal frequency ω, this number first decreases with increasing interaction length, whereupon it increases at distances z such that $|\beta_2|z \gtrsim 1$. The behavior of the mean number of photons at frequency 3ω (Fig. 13b) is more complicated. In this case, after the increase, it may decrease at certain interaction distances. For curve *1* in Fig. 13b, this occurs at $|\beta_2|z \gtrsim 0.5$.

For the relationship $\Phi = -\pi/2$ between the pump and signal phases, the Fano factors are given by the expressions

$$\begin{aligned}\mathcal{F}_1 &= \frac{1}{\langle n_1\rangle}\{\langle n_{10}\rangle(u_+ - F_+)^2[(G_+ - G_-)^2\\ &+ (u_+ - F_+)^2] + 2u_+^2F_+^2\\ &+ 2G_-^2G_+^2 + (F_+G_+ + u_+G_-)^2\},\end{aligned} \quad (46)$$

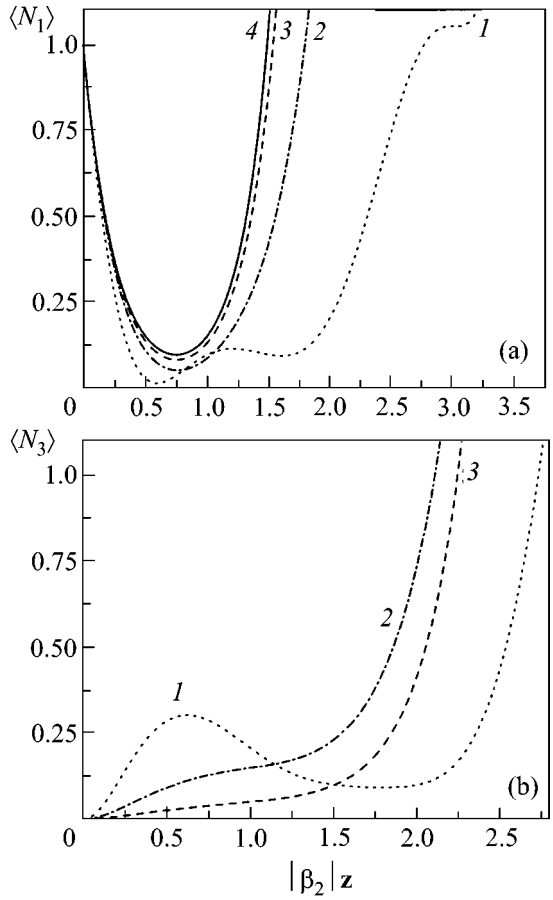

Fig. 13. Normalized mean number of photons (a) $\langle N_1\rangle$ and (b) $\langle N_3\rangle$ at, respectively, frequencies ω and 3ω vs. the reduced interaction length $|\beta_2|z$ for various ratios of the coefficients $|\beta_3/\beta_2|$: (*1*) 2, (*2*) 1, (*3*) 0.5, and (*4*) 0 ($\langle N_j\rangle = \langle n_j\rangle/\langle n_{10}\rangle$). The curves are constructed for the initial mean number of photons $\langle n_{10}\rangle = 100$.

$$\mathcal{F}_3 = \frac{1}{\langle n_3\rangle}\{\langle n_{10}\rangle(G_+ - G_-)^2[(G_+ - G_-)^2 + (u_- + F_-)^2] + 2u_-^2F_-^2 + 2G_-^2G_+^2 + (F_-G_+ + u_-G_-)^2\}. \quad (47)$$

An analysis of the behavior of the Fano factor showed [45, 46] that it is less than unity at certain distances, which corresponds to the sub-Poisson statistics. Notice once more that, if a signal at the entrance of a nonlinear crystal is absent, one always deal with the super-Poisson photon statistics. We established that the greater the initial number of signal photons, the smaller the Fano factor, i.e., the stronger the suppression of photon fluctuations. Therefore, with the nonlinear interaction considered, one can suppress the photon fluctuations at frequency ω and generate a sub-Poisson light at frequency 3ω. This effect is accompanied by a decrease in the intensity of the initial signal. The mean numbers of photons and the Fano factors at frequencies ω and 3ω

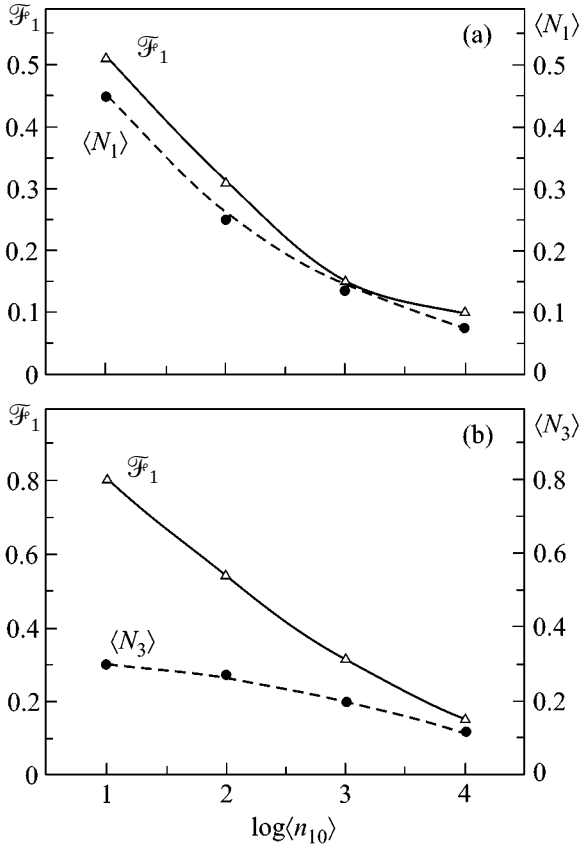

Fig. 14. Minimal values of the Fano factors (a) $\mathcal{F}_1$ and (b) $\mathcal{F}_3$ and of the corresponding normalized mean numbers of photons $\langle N_1\rangle$ and $\langle N_3\rangle$ vs. the initial mean number of photons. The graphs are calculated for (a) $|\beta_3| = 0$ and (b) $\beta_3/\beta_2 = 2$.

are shown in Fig. 14 as functions of the mean initial number of coherent-signal photons. The curves in Fig. 14 clearly demonstrate that the formation of a sub-Poisson light at the signal frequency is due to the removal of photons from this signal.

The most favorable conditions for the formation of sub-Poisson photon statistics occur at $|\beta_2|z = 1$ [45, 46]. The intensity of a coherent signal necessary for this condition to be met in the periodically poled $LiNbO_3$ crystal can be estimated as follows. Consider the interacting extraordinary waves. The nonlinear coefficient is $\beta_2 = 8\pi^2 d_{33}|A_2|/\lambda n m_2$, where λ is the pump wavelength and n is the refractive index at the same wavelength. For the crystal length $z = 1$ cm, $\lambda = 0.5$ μm, and quasi-phase-matching order $m_2 = 3$, one obtains $I_2 \approx 2 \times 10^7$ W/cm^2 for the pump intensity. This laser intensity can readily be obtained in the experiment. Thus, for the sequential nonlinear optical transformations, one can produce fields with the sub-Poisson photon statistics at frequencies both lower and higher than the pump frequency.

7. CONCLUSIONS

In this work, the results of combined investigations of the processes of light wave interactions in active nonlinear and nonlinear crystals with regular domain structure have been reported. The results of studying the processes of laser-frequency self-frequency conversion and sequential nonlinear optical interactions in crystals with regular domain structure are presented. The classical and quantum analyses of the processes of this class, such as laser-frequency self-frequency doubling and self-frequency halving, have been carried out. The calculations confirmed both the possibility of high-efficiency frequency conversion and the possibility of obtaining sources with suppressed quantum fluctuations.

An important problem associated with the influence of the aperiodic domain structure on the nonlinear optical interactions was not discussed in this review. The studies in this direction are in their infancy. Nevertheless, some interesting results have already been obtained in this respect. The influence of the aperiodic crystal structure on the sequential third harmonic generation was considered in [47]. In [48], the statistical theory of second harmonic generation in a disordered domain structure with fluctuating phase mismatch and nonlinear wave-coupling coefficient was developed. We have recently established that stochastic quasi-phase-matching, analogous to the usual quasi-phase-matching, may take place in crystals with the random aperiodic structure.

Experimental study of the statistical properties of light fields produced in the sequential interactions and laser-frequency self-frequency conversion is, no doubt, an important problem. The theory of these processes also calls for further elaboration.

Our studies form new avenue of investigations in nonlinear and quantum optics. It is associated with several simultaneous coupled wave interactions in nonlinear and active nonlinear crystals. The use of these processes allows one to increase the number of generated wavelengths in the same crystal and fabricate a miniature laser source for a number of applications.

We are grateful to I.I. Naumov, V.V. Firsov, A.V. Nikandrov, and E.Yu. Morozov for the contribution to the project.

This work was supported in part by the Russian Foundation for Basic Research, project no. 00-02-16040.

REFERENCES

1. N. F. Evlanova, A. S. Kovalev, V. A. Koptsik, *et al.*, Pis'ma Zh. Éksp. Teor. Fiz. **5**, 351 (1967) [JETP Lett. **5**, 291 (1967)].
2. L. F. Johnson and A. A. Ballman, J. Appl. Phys. **40**, 297 (1969).
3. A. A. Kaminskiĭ, D. Jaque, S. N. Bagaev, *et al.*, Kvantovaya Élektron. (Moscow) **26**, 95 (1999).
4. C. Q. Wang, Y. T. Chow, W. A. Gambling, *et al.*, Opt. Commun. **174**, 471 (2000).
5. P. Dekker, J. M. Dawes, J. A. Piper, *et al.*, Opt. Commun. **195**, 431 (2001).
6. C.-L. Wang, K.-H. Lin, T.-M. Hwang, *et al.*, Appl. Opt. **37**, 3282 (1998).
7. J. Bartschke, K.-J. Boller, R. Wallenstein, *et al.*, J. Opt. Soc. Am. B **14**, 3452 (1997).
8. D. Jaque, J. Capmany, J. Carsia Sole, *et al.*, J. Opt. Soc. Am. B **15**, 1656 (1998).
9. Z. Shengzi, Z. Xingyu, W. Qingpu, *et al.*, Opt. Laser Technol. **30**, 239 (1998).
10. P. Dekker, Y. Huo, J. M. Dawes, *et al.*, Opt. Commun. **151**, 406 (1998).
11. H. J. Zhang, X. L. Meng, L. Zhu, *et al.*, Opt. Commun. **160**, 273 (1999).
12. C. Q. Wang, Y. T. Chow, W. A. Gambling, *et al.*, Opt. Commun. **174**, 471 (2000).
13. P. Wang, J. M. Dawes, P. Dekker, and J. A. Piper, Opt. Commun. **174**, 467 (2000).
14. X. Zhang, S. Zhao, and O. Wang, J. Opt. Soc. Am. B **18**, 770 (2001).
15. P. Wang, J. M. Dawes, P. Dekker, *et al.*, J. Opt. Soc. Am. B **16**, 63 (1999).
16. Q. Ye, L. Shah, J. Eichenhold, *et al.*, Opt. Commun. **164**, 33 (1999).
17. J. Lu, G. Li, J. Liu, *et al.*, Opt. Commun. **168**, 405 (1999).
18. G. D. Laptev, A. A. Novikov, and A. S. Chirkin, J. Russ. Laser Res. **23**, 183 (2002).
19. *Physics of the Quantum Information*, Ed. by D. Bouwmeester, A. Ekert, and A. Zeilinger (Springer, Berlin, 2000; Postmarket, Moscow, 2002).
20. G. D. Laptev and A. A. Novikov, Kvantovaya Élektron. (Moscow) **31**, 981 (2001).
21. T. Y. Fan, A. Cordova-Plaza, M. J. F. Digonnet, *et al.*, J. Opt. Soc. Am. B **3**, 140 (1986).
22. A. S. Chirkin, V. V. Volkov, G. D. Laptev, and E. Yu. Morozov, Kvantovaya Élektron. (Moscow) **30**, 847 (2000).
23. A. S. Chirkin, J. Opt. B.: Quantum Semiclassic. Opt. **4**, S91 (2002).
24. G. D. Laptev and A. A. Novikov, Opt. Spektrosk. **93**, 131 (2002) [Opt. Spectrosc. **93**, 140 (2002)].
25. G. K. Kitaeva, I. I. Naumova, A. A. Mikhailovsky, *et al.*, Appl. Phys. B **66**, 201 (1998).
26. N. V. Kravtsov, G. D. Laptev, E. Yu. Morozov, *et al.*, Kvantovaya Élektron. (Moscow) **29**, 95 (1999).
27. J. Capmany, D. Callejo, V. Bermudez, *et al.*, Appl. Phys. Lett. **79**, 293 (2001).
28. K. S. Abedin, T. Tsuritani, M. Sato, and H. Ito, Appl. Phys. Lett. **70**, 10 (1997).
29. L. Barraco, A. Grisard, E. Lallier, *et al.*, Opt. Lett. **27**, 1540 (2002).
30. W. Sohler, *Technical Digest of the Pacific Rim Conference on Lasers and Electro-Optics* (Seoul, 1999), p. 1265.
31. M. Fujimura, N. Suhara, and H. Nishihara, *Abstracts of the International Workshop on Periodically Microstructured Nonlinear Optical Materials* (Madrid, 2001).

32. O. A. Gliko, Candidate's Dissertation (Moscow State Univ., Moscow, 1998).
33. I. I. Naumova, N. F. Evlanova, O. A. Gliko, and S. V. Lavrishchev, J. Cryst. Growth **181**, 160 (1997).
34. I. I. Naumova, N. F. Evlanova, S. A. Blokhin, and S. V. Lavrishchev, J. Cryst. Growth **187**, 102 (1998).
35. I. I. Naumova, N. F. Evlanova, S. V. Lavrishchev, *et al.*, Mater. Élektron. Tekh. **1**, 30 (1999).
36. N. V. Kravtsov, G. D. Laptev, I. I. Naumova, *et al.*, Kvantovaya Élektron. (Moscow) **32**, 923 (2002).
37. A. A. Novikov, G. D. Laptev, and A. S. Chirkin, Opt. Spektrosk. **94**, 820 (2003) [Opt. Spectrosc. **94**, 760 (2003)].
38. V. N. Gorbachev and E. S. Polzik, Zh. Éksp. Teor. Fiz. **96**, 1984 (1989) [Sov. Phys. JETP **69**, 1119 (1989)].
39. R. Schack, A. Sizmann, and A. Schenzle, Phys. Rev. A **43**, 6303 (1991).
40. A. S. Chirkin, J. Opt. B: Quantum Semiclassic. Opt. **4**, S91 (2002).
41. Y. Kim, S. P. Kulik, and Y. Shih, Phys. Rev. A **63**, 060301 (2001).
42. A. S. Chirkin and A. V. Nikandrov, Laser Phys. **12**, 941 (2002).
43. A. S. Chirkin, Opt. Spektrosk. **87**, 627 (1999) [Opt. Spectrosc. **87**, 575 (1999)].
44. V. V. Volokhovskiĭ and A. S. Chirkin, Kvantovaya Élektron. (Moscow) **31**, 437 (2001).
45. A. V. Nikandrov and A. S. Chirkin, Pis'ma Zh. Éksp. Teor. Fiz. **76**, 333 (2002) [JETP Lett. **76**, 275 (2002)].
46. A. S. Chirkin and A. V. Nikandrov, J. Opt. B.: Quantum Semiclassic. Opt. **5**, 169 (2003).
47. E. Yu. Morozov and G. D. Laptev, Izv. Ross. Akad. Nauk, Ser. Fiz. **66**, 1108 (2002).
48. E. Yu. Morozov, A. A. Kaminskiĭ, A. S. Chirkin, and D. B. Yusupov, Pis'ma Zh. Éksp. Teor. Fiz. **73**, 731 (2001) [JETP Lett. **73**, 647 (2001)].

Translated by V. Sakun

JETP Letters, Vol. 78, No. 1, 2003, pp. 5–7. Translated from Pis'ma v Zhurnal Éksperimental'noĭ i Teoreticheskoĭ Fiziki, Vol. 78, No. 1, 2003, pp. 8–10.

Is There a Collective Dielectric Resonance?

A. N. Oraevsky

Lebedev Institute of Physics, Russian Academy of Sciences, Leninskiĭ pr. 53, Moscow, 117924 Russia

e-mail: oraevsky@sci.lebedev.ru

Received April 28, 2003; in final form, May 30, 2003

It is shown that the Maxwell–Garnett equation predicts resonance in a heterogeneous material consisting of ellipsoids embedded in a matrix, even if the ellipsoids are made from a transparent material. It is suggested that the resonance of this type be denoted as collective because it cannot be achieved in a single ellipsoid. However, the problem of applicability of the Maxwell–Garnett equation in the range of ellipsoid concentrations corresponding to the resonance condition remains unsolved. © *2003 MAIK "Nauka/Interperiodica".*

PACS numbers: 77.22.Ej

1. Resonance in a single ellipsoid. The so-called plasmon resonance occurring in spherical or ellipsoidal metallic particles is well known [1]. It was shown in [2] that the plasmon resonance in prolate metallic ellipsoids of revolution is shifted in frequency with respect to the resonance in spherical particles. The intensity of resonance in ellipsoids is also notably higher than in spheres. This follows from the equation relating the field strength $E_k^{(el)}$ in an ellipsoid to the uniform field strength E_k in the medium surrounding the ellipsoid [3]:

$$E_k^{(el)} = \frac{2\varepsilon_m}{(\varepsilon_{el} - \varepsilon_m)A_k + 2\varepsilon_m} E_k. \quad (1)$$

Here, E_k is the projection of an external field onto the ellipsoid axis; index k assumes three different values for the three axes a, b, and c of the ellipsoid; the lengths of the ellipsoid axes are also denoted by a, b, and c; $\varepsilon_m = \varepsilon_m' + i\varepsilon_m''$ is the dielectric constant of the medium (matrix) surrounding the ellipsoid; $\varepsilon_{el} = \varepsilon_{el}' + i\varepsilon_{el}''$ is the dielectric constant of the ellipsoid material; and the value of A_k is determined by the following integral [3]:

$$A_k = \int_0^\infty \frac{abc}{(s + d_k^2)\sqrt{(s + a^2)(s + b^2)(s + c^2)}} ds, \quad (2)$$

where $k = a, b, c$; $d_a \equiv a$, $d_b \equiv b$, and $d_c \equiv c$. Equation (1) is valid if the transverse size of the ellipsoid is considerably smaller than its length. This condition is discussed in more detail, for example, in [2]. For the optical wavelength range, the transverse size of the particles should not exceed several tens of nanometers to satisfy this condition.

In the literature, A_k is often referred to as the depolarization parameter. The dependences of A_k of an ellipsoid of revolution ($a = b$) on the aspect ratio ξ ($\xi = c/a$) are shown in Fig. 1 for the field directed along the ellipsoid axis c (A_c) and perpendicularly to this axis (A_a). It can be seen from Fig. 1 that $0 < A_c < 2$ and $0 < A_a < 1$.

The condition for plasmon resonance follows from Eq. (1):

$$\varepsilon_{el}' A_k + (2 - A_k)\varepsilon_m' = 0. \quad (3)$$

The parameter A_k does not exceed 2, so that the resonance condition can be met only if ε_{el}' or ε_m' is negative. The width and intensity of resonance depend on the parameter $A_k\varepsilon_{el}'' + (2 - A_k)\varepsilon_m''$: the smaller its value, the narrower and more intense the resonance.

It follows from Eq. (3) that

$$\varepsilon_{el}'/\varepsilon_m' = (2 - A_k)/A_k. \quad (4)$$

Equation (4) shows that the optical density of the ellipsoid material can be higher ($A_k < 1$) or lower ($A_k > 1$) than the optical density of the surrounding medium. However, the latter is possible only for an oblate ellipsoid (spheroid) in a field directed along its axis, because this requires $A_k > 1$ (see Fig. 1).

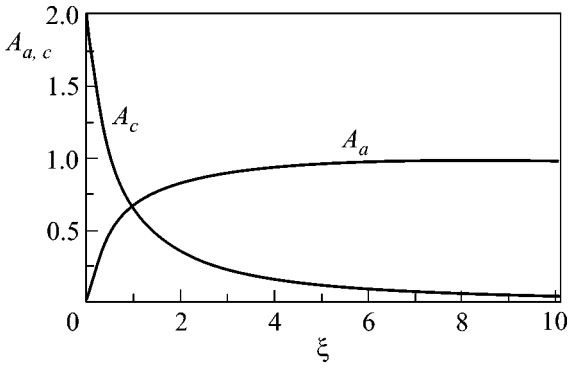

Fig. 1. Dependence of the depolarization parameter of an ellipsoid of revolution on its aspect ratio ξ.

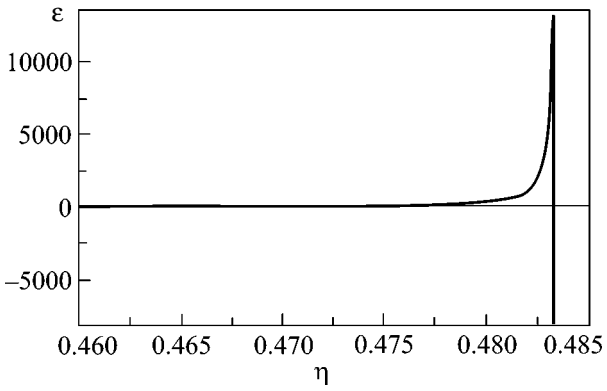

Fig. 2. Dependence of the effective dielectric constant of a transparent heterogeneous material on the relative concentration of ellipsoids: $A = 0.1$, $\varepsilon'_{el}/\varepsilon'_m = 10$.

Collective dielectric resonance. The frequency of plasmon resonance in a medium consisting of metal spheres embedded in a matrix depends on the concentration of spheres, as follows from the Maxwell–Garnett equation for the dielectric constant of a heterogeneous medium [4-6]:

$$\frac{\varepsilon - \varepsilon_m}{\varepsilon + 2\varepsilon_m} = \eta\frac{\varepsilon_b - \varepsilon_m}{\varepsilon_b - 2\varepsilon_m}, \qquad (5)$$

where ε is the effective dielectric constant of the heterogeneous medium, ε_b is the dielectric constant of the material of the spheres, and η is the relative concentrations of the spheres. Although the Maxwell–Garnett equation has long been discussed in the literature [1], the problem of the dependence of the plasmon resonance position on the concentration of nanoparticles had not attracted special attention until the works [6, 7] were published. Taking into account the results considered in the preceding section, it can be expected that the resonance in a medium consisting of ellipsoids has interesting specific features.

The dielectric constant a material based on oriented ellipsoids is described by a tensor. Analysis of the case of an arbitrary mutual orientation of the ellipsoids and the external field is a challenging task. It becomes considerably simpler if the field is directed along the ellipsoid axis or perpendicular to it, i.e., along one of the principal axes of the tensor of the dielectric constant of a heterogeneous medium. Further consideration will be restricted to this case. For the field directed along one of the principal axes, the Maxwell–Garnett equation takes the form

$$\frac{\varepsilon_{a(c)} - \varepsilon_m}{\varepsilon_{a(c)} + 2\varepsilon_m} = \frac{2}{3}\eta\frac{\varepsilon_{el} - \varepsilon_m}{(\varepsilon_{el} - \varepsilon_m)A_{a(c)} + 2\varepsilon_m}. \qquad (6)$$

By solving this equation for $\varepsilon_{a(c)}$, one gets

$$\varepsilon_{a(c)} = \varepsilon_m\frac{1 + 2F_{a(c)}(\eta)}{1 - F_{a(c)}(\eta)}, \qquad (7)$$

where

$$F_{a(c)}(\eta) = \frac{2}{3}\eta\frac{\varepsilon_{el} - \varepsilon_m}{(\varepsilon_{el} - \varepsilon_m)A_{a(c)} + 2\varepsilon_m}. \qquad (8)$$

In the general case, $F_{a(c)}(\eta) = F'_{a(c)}(\eta) + iF''_{a(c)}(\eta)$ is a complex quantity. The condition for resonance amounts to the real part of the denominator in Eq. (7) vanishing: $1 - F'_{a(c)}(\eta) = 0$. In the expanded form, this condition is written as follows:

$$\left(A_{a(c)} - \frac{2}{3}\eta\right)\varepsilon'_{el} + \left(2 + \frac{2}{3}\eta - A_{a(c)}\right)\varepsilon'_m = 0. \qquad (9)$$

For spherical particles ($A = 2/3$), the condition (9) can be met only if $\varepsilon'_{el} < 0$ or $\varepsilon'_m < 0$. That is why the authors of [6, 7] considered the optical properties of a heterogeneous medium consisting of metal nanospheres.

The fundamental difference between conditions (9) and (3) is that condition (9) for ellipsoidal particles can be met if the media with positive real parts of the dielectric constant (including transparent media) are used. It is suggested that this type of resonance be denoted as *collective* because it cannot be achieved in a single ellipsoid. As follows from Eq. (9), the media with the required ratio of dielectric constants should satisfy the condition $1 > \eta > 1.5A$. As an example, the dependence of the dielectric constant of a transparent material consisting of ellipsoids with $A = 0.1$ on η is shown in Fig. 2 (from here on, indices in $\varepsilon_{a(c)}$ and $A_{a(c)}$ are omitted). The aspect ratio ξ of these ellipsoids should be ~0.07 (spheroids) or ~5.4 (prolate ellipsoids). It can be seen that, as the concentration of particles approaches a critical value, the dielectric constant increases indefinitely. Obviously, such an increase is not observed in actual materials: various losses occurring even in transparent materials (including dispersion losses) remove the singularity without eliminating the resonance.

However, what is the reason for raising the question formulated in the title of this work? The point is that the limits of applicability of the Maxwell–Garnett equation for high concentrations of particles in a dielectric medium have long been discussed in the literature. There is experimental data [1, Fig. 125] showing that, in some cases, the Maxwell–Garnett equation is valid for concentrations up to 40%. However, as shown below, the Maxwell–Garnett equation has a more serious flaw.

Let us assume that the matrix is made from an absorbing material, so that $\varepsilon_m = \varepsilon'_m + i\varepsilon''_m$, where $\varepsilon''_m > 0$. In this case, the dependence of ε'' on the concentration parameter η takes the form shown in Fig. 3. It can be seen that, as the concentration of particles exceeds a certain value, ε_m becomes negative. This means that a composite medium consisting of absorbing components can become amplifying if the concentration of ellipsoids is sufficiently high. This conclusion contra-

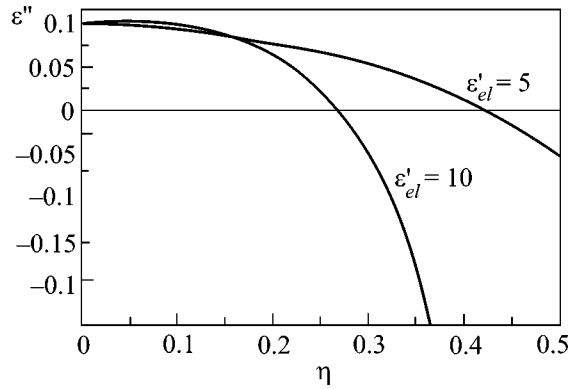

Fig. 3. Dependence of ε" on the relative concentration η of ellipsoidal particles: $A = 0.1$, $\varepsilon'_m = 1.5$, $\varepsilon''_m = 0.1$.

dicts the energy conservation law. Does it mean that all consequences of the Maxwell–Garnett equation should be rejected? It is hard to answer this question: all consequences cannot be taken to be invalid beforehand. For a long time, a better equation describing the dielectric constant of heterogeneous media has been searched for, but without any considerable success. In particular, there is still no adequate formula providing more balanced consideration of the dielectric constants of a medium and particles than the Maxwell-Garnett equation. For a good review of the literature on the subject see [1]. In our opinion, the possibility of such interesting effects as the collective dielectric resonance should give an additional impetus to the search for a more perfect equation describing the dielectric constant of heterogeneous media. This is one of the topical problems of the further theoretical and experimental studies of the electrodynamics of heterogeneous materials (including composite materials).

I am grateful to V.V. Klimov, V.S. Zuev, and I.E. Protsenko for stimulating discussion. This work was supported by the Russian Foundation for Basic Research, project no. 00-02-16660.

REFERENCES

1. Yu. I. Petrov, *Physics of Small Particles* (Nauka, Moscow, 1982).
2. A. A. Oraevskiĭ and A. N. Oraevskiĭ, Kvantovaya Élektron. (Moscow) **32** (1), 79 (2002).
3. J. A. Stratton, *Electromagnetic Theory* (McGraw-Hill, New York, 1941; Gostekhizdat, Moscow, 1948).
4. J. C. Maxwell-Garnett, Philos. Trans. R. Soc. London, Ser. A **203**, 385 (1904).
5. J. C. Maxwell-Garnett, Philos. Trans. R. Soc. London, Ser. A **205**, 237 (1906).
6. A. N. Oraevskiĭ and I. E. Protsenko, Pis'ma Zh. Éksp. Teor. Fiz. **72**, 641 (2000) [JETP Lett. **72**, 445 (2000)].
7. A. N. Oraevskiĭ and I. E. Protsenko, Kvantovaya Élektron. (Moscow) **31**, 252 (2001).

Translated by K. Chamorovskiĭ

JETP Letters, Vol. 78, No. 1, 2003, pp. 8–12. Translated from Pis'ma v Zhurnal Éksperimental'noĭ i Teoreticheskoĭ Fiziki, Vol. 78, No. 1, 2003, pp. 11–15.

Atom Nanooptics Based on Photon Dots and Photon Holes

V. I. Balykin[1], V. V. Klimov[2, *], and V. S. Letokhov[1]

[1]*Institute of Spectroscopy, Russian Academy of Sciences, Troitsk, Moscow region, 142190 Russia*
[2]*Lebedev Physical Institute, Russian Academy of Sciences, Leninskiĭ pr. 53, Moscow, 119991 Russia*
**e-mail: vklim@sci.lebedev.ru*

Received June 3, 2003

New types of light fields localized in nanometer-sized regions of space were observed and analyzed. The possibility of using these nanolocalized fields in atom optics for atom focusing and localization is discussed.

PACS numbers: 03.75.Be; 32.80.Lg; 39.25.+k; 81.16.Ta

Atom optics is a new type of optics (along with photon, electron, and neutron optics). It has emerged in the last 20 years as a result of studying the action of electromagnetic radiation on spatial atomic motion [1–5]. Atom optics is subdivided into two types: (a) atom optics based on the mechanical micro- and nanostructures (e.g., zone plates) and (b) atom optics based on the use of laser radiation in the presence of static electric and magnetic fields. Atom optics encompasses physical problems that are associated with studying atomic interactions with surfaces and electromagnetic fields in an effort to determine those interaction potentials which provide a controlled action on the spatial atomic motion; among these problems are diffraction of atomic waves and their interference, focusing of atomic waves, mirror reflection, atomic localization in a confined spatial region (atomic traps), and the increase in the phase density of atomic ensembles.

Laser atom optics has a number of limitations of both fundamental and technical character; since the laser fields are spatially nonlocalized, the elements of atom optics are also nonlocalized. As a result, such imperfections as aberration of atom lenses, low diffraction efficiency of atomic waves, and limiting contrast of interference fringes in atomic interferometers are inherent in the elements of atom optics.

From general physical considerations, it is clear that spatially localized potentials are more favorable for constructing the elements of atom optics. At present, only two types of spatially localized laser fields are known: (a) a surface (evanescent) light wave arising upon total internal reflection (one-dimensional light localization) and (b) a light field appearing upon its diffraction by structures with characteristic sizes smaller than the light wavelength. The most familiar example of the second type of localized light field is provided by a field arising upon the diffraction by an aperture with a size smaller than the wavelength in an ideally conducting screen. In this case, a local three-dimensional field maximum forms near a small aperture, with sizes mainly determined by the sizes [6–8].

A serious disadvantage of the field localized near an isolated aperture is that it is inevitably connected with the field of the associated standing wave. When an atom moves in this region, it may undergo spontaneous decay, which is highly undesirable in many problems of atom optics. In this work, new types of a spatially localized nanometer-sized light field free of the above-mentioned disadvantage are proposed. The possibility of using such a *nanofield* in the problems of atom optics (*atom nanooptics*) is considered.

The scheme of producing spatially localized light nanofield is illustrated in Fig. 1a. Two flat conducting screens with a distance between them on the order of or shorter than the light wavelength, $d \leq \lambda$, form a planar two-dimensional waveguide for laser radiation that enters the waveguide from the side. As known [9], the solutions to the Maxwell equations for a waveguide consisting of two parallel ideally conducting planes allow the propagation of radiation in a waveguide of an arbitrarily small thickness *d*, including the thickness much smaller than the radiation wavelength. The solution inside the waveguide coincides with a plane wave

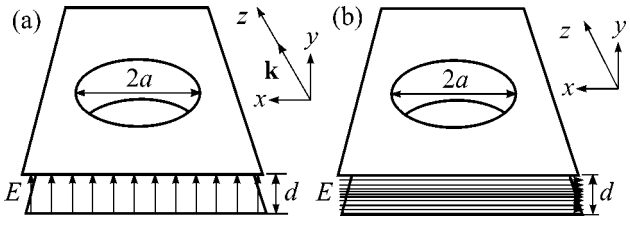

Fig. 1. Geometry of the formation of (a) photon hole and (b) photon dot by nanoapertures in a planar optical waveguide formed from two conducting planes.

0021-3640/03/7801-0008$24.00

whose electric field is directed perpendicular to the planes. In fact, this system is a double-wire line and provides two-dimensional nanometer-sized light localization [9].

Now let two small coaxial apertures with radius $a \ll \lambda$ be formed in a conducting screen (Fig. 1). If the aperture diameters are much smaller than the wavelength of incident radiation, it will practically not pass through these apertures but will be strongly modified near each of the apertures. In fact, the field is reduced near the apertures in the region with the characteristic sizes on the order of the aperture diameter, i.e., much smaller than the radiation wavelength λ. The volume of this region is $V \sim a^2 d \ll \lambda^3$. A field modification of this kind can naturally be called a "photon hole."

The determination of the field distribution near the apertures in the waveguide walls is a challenging task of electrodynamics. In the particular case of a nanoaperture ($a \ll \lambda$), the problem becomes quasistatic. Indeed, let the wave propagate along the Z axis, as shown in Fig. 1a, and be polarized along the Y axis. Then, in the absence of apertures, the nonzero field components (for the traveling wave) are

$$E_y = E_0 e^{i(kz-\omega t)}, \quad H_x = -E_0 e^{i(kz-\omega t)}, \qquad (1)$$

where $k = \omega/c$.

In the presence of small apertures, this problem reduces, to a first approximation, to the quasistatic problem. The corresponding general solution is obtained by solving the integral equation for the charge densities in planes [10]. If the waveguide thickness d is larger than the aperture diameter, $\lambda > d \gg a$, one can ignore the mutual influence of apertures, so that the problem reduces to the superposition of fields caused by the diffraction by individual apertures. The problem of the modification of a uniform field in the presence of a conducting plane with a round aperture in it can be solved analytically [11]. The resulting expression for the potential φ of electric field $\mathbf{E} = -\nabla\varphi$ has the form

$$\varphi(r, y) = \varphi^+\left(r, y - \frac{d}{2}\right) + \varphi^-\left(r, y + \frac{d}{2}\right),$$

$$\varphi^\pm(r, y) = -\frac{E_0}{2}(y \mp d)$$

$$\pm \frac{E_0}{\pi}|y|\left(\frac{1}{\mu(r, y)} + \arctan\mu(r, y)\right), \qquad (2)$$

$$\mu(r, y) = \left[\frac{1}{2}\left(\frac{r^2}{a^2} + \frac{y^2}{a^2} - 1\right) + \frac{1}{2}\sqrt{\left(\left(\frac{r^2}{a^2} + \frac{y^2}{a^2} - 1\right)^2 + 4\frac{y^2}{a^2}\right)}\right]^{1/2},$$

where $r^2 = x^2 + z^2$.

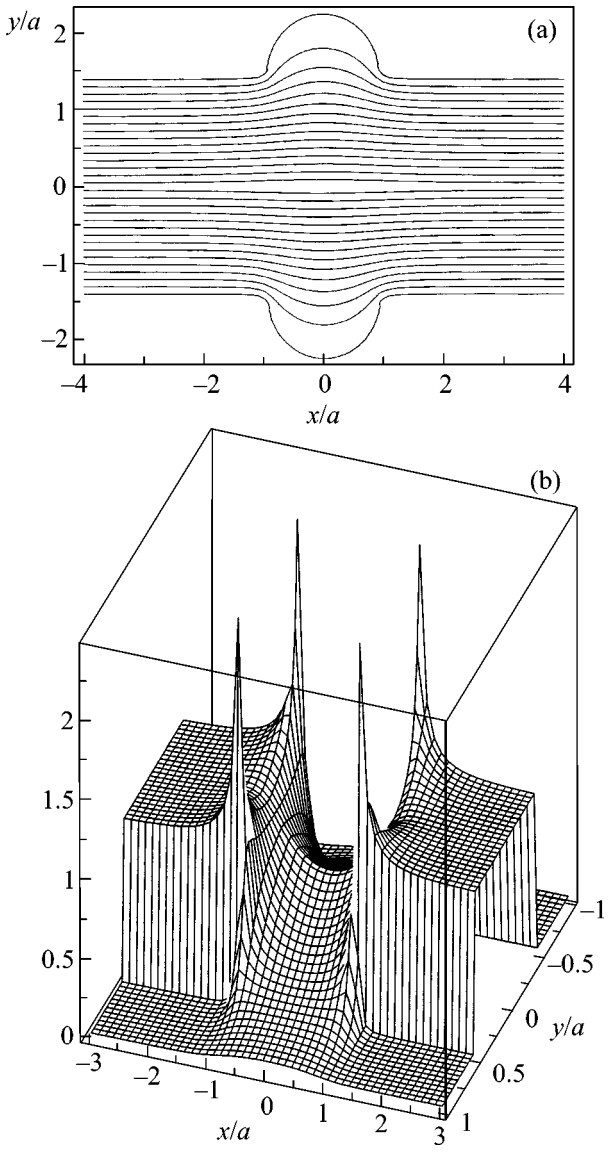

Fig. 2. (a) Isolines of potential (2) describing a photon hole with $a/d = 1/3$, and (b) electromagnetic-field intensity for a photon hole with $a/d = 1$.

The distribution of the equipotential lines (2) and the electric-field energy density proportional to $\mathbf{E}^2 = (\nabla\varphi)^2$ are shown in Fig. 2. One can see in Fig. 2 that a photon hole or, to be more precise, photon saddle with the characteristic sizes determined by the aperture size and the waveguide thickness actually appears near the apertures.

We now consider one more way of field localization in nanometer-sized regions (Fig. 1b). It generalizes the method of localization near an aperture [8] but is free from the drawback associated with the presence of a standing wave. Let us again take two ideally conducting planes with apertures in them, but let the planes be separated by $d = \lambda/2$. In this case, one of the solutions

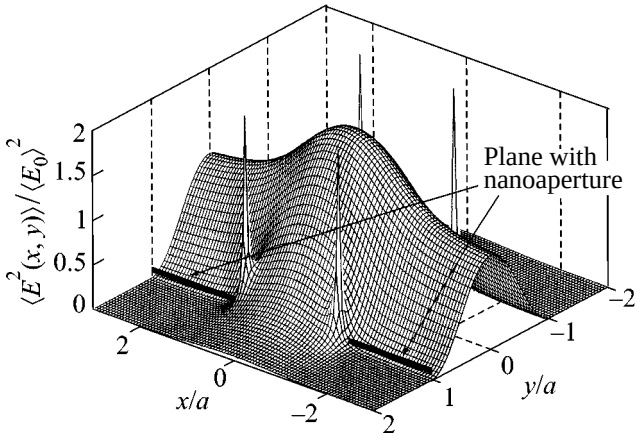

Fig. 3. Electromagnetic-field intensity for a photon dot with $a/d = 0.5$.

(TE_{01}) in the absence of apertures has the nonzero components

$$E_{0,x} = -2i\cos\left(\frac{\pi}{d}y\right)e^{-i\omega t},$$
$$H_{0,z} = 2\sin\left(\frac{\pi}{d}y\right)e^{-i\omega t}. \tag{3}$$

Physically, solution (3) corresponds to the standing wave whose wave vector is perpendicular (directed along the **Y** axis) to the planes. At the same time, Eq. (3) is a portion of the standing wave formed upon the reflection of a plane wave incident normally onto one of the planes. Due to the condition $d = \lambda/2$, the other plane occurs in the node of this standing wave and does not affect it.

If the apertures are small compared to the wavelength, $a \ll d = \lambda/2$, their mutual influence can be ignored, and one can use the solution to the problem of diffraction by a single aperture [6–8]. For the circular polarization, the field components are

$$\mathbf{E}_0 = -\frac{1}{\sqrt{2}}(1, 0, i)2i\cos\frac{\pi}{d}y \quad \left(-\frac{d}{2} < y < \frac{d}{y}\right),$$
$$\mathbf{H}_0 = -\frac{1}{\sqrt{2}}(i, 0, -1)2\sin\frac{\pi}{d}y \quad \left(-\frac{d}{2} < y < \frac{d}{y}\right), \tag{4}$$

and the time-averaged squared electric field modified by the apertures takes the form

$$\langle E^2\rangle = \left(\frac{a}{3d}\right)^2 W, \tag{5}$$
$$W = \left\{A\left(r, \left|y + \frac{d}{2}\right|\right)^2 + \left(A\left(r, \left|y + \frac{d}{2}\right|\right)\right.\right.$$
$$\left.\left. + B\left(r, \left|y + \frac{d}{2}\right|\right)\right)^2 + C\left(r, \left|y + \frac{d}{2}\right|\right)^2\right\} \quad (y < -d/2),$$

$$W = \left\{18\pi^2\frac{\cos^2\frac{\pi}{d}y}{(ka)^2} + 6\pi\frac{\cos\frac{\pi}{d}y}{ka}(2\hat{A} + \hat{B}) + \hat{A}^2\right.$$
$$\left. + (\hat{A} + \hat{B})^2 + \hat{C}^2)\right\} \quad \left(-\frac{d}{2} < y < \frac{d}{2}\right),$$

$$W = \left\{A\left(r, \left|y - \frac{d}{2}\right|\right)^2 + \left(A\left(r, \left|y - \frac{d}{2}\right|\right)\right.\right.$$
$$\left.\left. + B\left(r, \left|y - \frac{d}{2}\right|\right)\right)^2 + C\left(r, \left|y - \frac{d}{2}\right|\right)^2\right\} \quad (y > d/2),$$

where

$$\hat{A} = A\left(r, \left|y - \frac{d}{2}\right|\right) + A\left(r, \left|y + \frac{d}{2}\right|\right),$$
$$\hat{B} = B\left(r, \left|y - \frac{d}{2}\right|\right) + B\left(r, \left|y + \frac{d}{2}\right|\right), \tag{6}$$
$$\hat{C} = C\left(r, \left|y - \frac{d}{2}\right|\right) + C\left(r, \left|y + \frac{d}{2}\right|\right)$$

and

$$A(r, y) = R^-\left(\frac{2a^2}{R^*} + 2 - \frac{y^2}{r^2}\right)$$
$$+ ya\left(\frac{R^+}{r^2} - \frac{3}{a^2}\arctan\left(\frac{1}{R^+}\right)\right),$$
$$B(r, y) = R^-\left(\frac{2y^2}{r^2} - \frac{2r^2 - y^2}{R^*}\right)$$
$$+ yR^+a\left(\frac{1}{R^*} - \frac{2}{r^2}\right) + \frac{3yr^2R^+}{aR^*(1 + R^{+2})}, \tag{7}$$
$$C(r, y) = \frac{2arR^+}{R^*(1 + R^{+2})},$$
$$R^* = ((r^2 + y^2 - a^2)^2 + 4a^2y^2)^{1/2},$$
$$R^\pm = \left(\frac{R^* \pm (r^2 + y^2 - a^2)}{2a^2}\right)^{1/2}.$$

The intensity distribution of the field near the apertures of a planar waveguide and inside the waveguide is shown in Fig. 3 for a waveguide with a half-wavelength thickness and a aperture radius $a = \lambda/4$. It is seen from the figure that the field outside the waveguide drops rather rapidly in the direction perpendicular to the waveguide plane and has a maximum inside the waveguide; i.e., a "photon dot" arises. The characteris-

tic size of such a photon dot is $V \sim \frac{\lambda}{2} a^2 \ll \lambda^3$. The sharp field-intensity spikes near the aperture edge appear because the conductivity of the waveguide walls is assumed to be infinite. In the waveguides with a finite wall conductivity, the spike amplitudes will be less pronounced. Of prime importance is that the maximum (measured from the level in the absence of apertures) at $x = y = 0$ is twice its value for the case of a single aperture. This is caused by the constructive interference of the fields scattered by apertures, allowing the use of fields lower than in the case of a single aperture.

Consider two examples of application of the spatially localized light field (photon dots and apertures) in atom focusing and localization.

Atom lens. We first consider the possibility of using localized fields for focusing atomic beams by the gradient force proportional to the electric-field strength. For the positive detuning between the laser frequency and the atomic-emission frequency, an atom is expelled to weaker fields, whereas, for the negative frequency detuning, it is drawn into the region with stronger fields.

In the case of a photon hole, the nanometer-sized weak-field region is surrounded inside the waveguide by a strong field and, in the case of positive frequency detuning, an atom passing through the aperture will be drawn to the axis of the system; i.e., focusing will occur. As was mentioned above, it is quite important that the focused beams mainly move in the weak-field region, where the defocusing spontaneous-decay processes are highly improbable.

In the case of negative frequency detuning, atoms are drawn in by a photon dot, and, hence, focusing again takes place. In a photon dot, an atom moves through the strong-field region, and, thus, the spontaneous decay probability is higher than in the photon hole. However, the passage time through the nanometer region is short, so that the influence of the spontaneous decay on the focusing can again be ignored.

The theory of focusing atomic beams in the regions both with maxima and minima of an electric field is well elaborated. In particular, it was shown in [12, 13] that, in the absence of spontaneous decay, an atomic beam can be focused on an area with a diameter on the order of atomic de Broglie wavelength, which is equal to several Angströms for thermal beams. These results fully apply to our photon dots and apertures, because the spontaneous decay can be ignored in our case.

Atomic trap. For a system with the symmetry considered above, the optical-field configurations have extreme points where the gradient is zero. The configurations of these fields can naturally be considered as the possible trap configurations. The configuration of a photon dot is stable and is genuinely three-dimensional (Fig. 3), with the characteristic volume on the order of $a^2\lambda/2 \ll \lambda^3$. The depth of such a trap is twice the depth of a single-aperture trap [8].

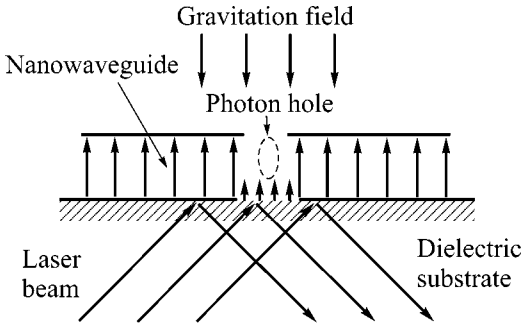

Fig. 4. Scheme of the three-dimensional trap configuration for a photon hole with the use of a surface wave formed upon the total internal reflection from a dielectric layer beneath the waveguide.

The extreme point of a photon hole is a saddle point (Fig. 2b): for the positive detuning, the radial motion is stable, while the motion along the axis is unstable. The opposite situation occurs for the negative detuning. However, it is desirable to determine the stable trap configuration for a nanometer-sized photon hole (all its dimensions can be much smaller than the wavelength!). The stable three-dimensional trap configuration in the case of a photon hole can be formed after slight waveguide modification with the use of the gravitational field. One such variant of a three-dimensional trap based on a photon hole is shown in Fig. 4.

In the scheme proposed, a photon hole with positive frequency detuning localizes atoms in the radial direction. From below, atoms are localized due to the exponentially decaying field that is formed upon the total internal reflection of a plane wave with the positive frequency detuning. The gravitational field provides atomic localization from above.

Therefore, both optical-field configurations proposed in this work provide three-dimensional atomic localization in nanometer-sized regions.

Note that one can produce a large number (lattice) of aperture pairs and, accordingly, the same number of localized fields (zero-dimensional photon holes and dots). Such a lattice allows simultaneous control of many atomic beams. In turn, such lattices can be used to form periodic lattices of localized atoms (atom lattices [14]) with a period independent of the light wavelength. The properties of such periodic lattices can be similar to the properties of planar photonic crystals [15], but, as distinct from the latter, they can combine both photon-dot lattices and lattices of localized atoms. On the whole, the approach suggested in this work forms, together with [8, 12, 13], the concept of atom nanooptics, i.e., atom optics based on optical nanofields.

We are grateful to Prof. V.G. Minogin, P.N. Melent'ev, and Prof. Shimizu (Japan) for helpful

discussions of results. This work was supported in part by the Russian Foundation for Basic Research (project nos. 02-17014, 02-16337a, 02-16592a), the program "Integratsiya," and INTAS (no. INFO-00-479).

REFERENCES

1. V. Balykin and V. Letokhov, Phys. Today **42**, 23 (1989).
2. C. S. Adams, M. Sigel, and J. Mlynek, Phys. Rep. **240**, 143 (1994).
3. V. Balykin and V. Letokhov, *Atom Optics with Laser Light* (Harwood Academic, Chur, Switzerland, 1995).
4. P. Meystre, *Atom Optics* (Springer, New York, 2001).
5. *Nanofabrication with Atom Optics*, Ed. by P. Meschede and J. Mlynek, Special Issue of Appl. Phys. B **70** (5) (2000).
6. H. A. Bethe, Phys. Rev. **66**, 163 (1944); C. J. Bouwkamp, Philips Res. Rep. **5**, 401 (1950).
7. V. V. Klimov and V. S. Letokhov, Opt. Commun. **106**, 154 (1994).
8. V. V. Klimov and V. S. Letokhov, Opt. Commun. **121**, 130 (1995).
9. L. A. Vaĭnshteĭn, *Electromagnetic Waves*, 2nd ed. (Radio i Svyaz', Moscow, 1988).
10. N. N. Lebedev, Zh. Tekh. Fiz. **27**, 2097 (1957) [Sov. Phys. Tech. Phys. **2**, 1943 (1957)].
11. M. Szilagyi, *Electron and Ion Optics* (Plenum, New York and London, 1988).
12. V. I. Balykin, V. V. Klimov, and V. S. Letokhov, Pis'ma Zh. Éksp. Teor. Fiz. **59**, 219 (1994) [JETP Lett. **59**, 235 (1994)].
13. V. V. Klimov and V. S. Letokhov, Laser Phys. **13**, 339 (2003).
14. V. S. Letokhov, in *Trapped Particles and Fundamental Physics*, Ed. by S. N. Atutov, R. Calabrese, and L. Moi (Kluwer Academic, Dordrecht, 2002), pp. 10–11.
15. E. Yablonovitch, Phys. Rev. Lett. **58**, 2059 (1987); S. John, Phys. Rev. Lett. **58**, 2486 (1987).

Translated by V. Sakun